REPORT DOCUMENTATION PAGE

Form Approved
OMB No. 0704-0188

1. REPORT DATE *(DD-MM-YYYY)*	2. REPORT TYPE	3. DATES COVERED *(From - To)*
08/31/2007	Final	7/2/2002 to 7/1/2007

4. TITLE AND SUBTITLE
Development of Novel Instrumentation to Characterize Aerosol Insets and Cloud Particles

5a. CONTRACT NUMBER
N00014-02-C-0317

5b. GRANT NUMBER

5c. PROGRAM ELEMENT NUMBER

6. AUTHOR(S)
Dr. Paul Lawson

5d. PROJECT NUMBER

5e. TASK NUMBER

5f. WORK UNIT NUMBER

7. PERFORMING ORGANIZATION NAME(S) AND ADDRESS(ES)
SPEC Inc.
3022 Sterling Circle Suite 200
Boulder, CO 80301

8. PERFORMING ORGANIZATION REPORT NUMBER
Final

9. SPONSORING/MONITORING AGENCY NAME(S) AND ADDRESS(ES)
Office of Naval Research for Naval Postgraduate School, CIRPAS (Monterey)
ONR 253
Ballston Tower One
800 North Quincy Street
Arlington, CA 22217

10. SPONSOR/MONITOR'S ACRONYM(S)
CIRPAS

11. SPONSORING/MONITORING AGENCY REPORT NUMBER
N00014

12. DISTRIBUTION AVAILABILITY STATEMENT
Approved for public release; SBIR report, distribution unlimited.

13. SUPPLEMENTARY NOTES

14. ABSTRACT

SPEC Incorporated was contracted in Phase II by the Office of Naval Research to develop innovative new technology to measure the size, shape and concentration of water drops and ice particles in clouds. This effort included the main SBIR Phase II contract and two options. The principal objectives of the main SBIR phase II contract and its two options are:

Main Contract: Development of a 2D-S (Stereo) cloud particle imaging probe

Option 1: Determine the feasibility of designing and developing a 3V-CPI probe.

Option 2: Design and fabricate a 3V-CPI probe for use on research aircraft.

One result of the Phase II research was the development of a new cloud particle-imaging probe, the 2D-S (Stereo) probe, which has been installed on four research aircraft and flown in four major field campaigns sponsored by the National Science Foundation (NSF) and the National Aeronautics and Space Administration (NASA). A description of the 2D-S probe and scientific results from field campaigns are the subject of two refereed journal publications.

A second result is the ongoing development of another innovative cloud particle-imaging probe, called a 3V-CPI, which is essentially a combination of a 2D-S and the SPEC cloud particle imager. The 3V-CPI is being developed under a joint

INSTRUCTIONS FOR COMPLETING SF 298

agreement between the Navy and the NSF, whereby two 3V-CPI probes are being developed in parallel under joint funding from both agencies. Both the Navy and NSF agreed to this arrangement to facilitate development of the 3V-CPI under available funding. The Navy 3V-CPI will undergo final assembly and testing and be delivered to CIRPAS for use in the VOCALS field campaign scheduled for autumn 2008 in Chile. The NSF instrument, which is essentially identical to the Navy instrument, will be tested on the NSF owned Gulfstream V research aircraft before the Navy probe is delivered.

The principal result from this research is work on the development of a new instrument, the 3V-CPI, for atmospheric research. The 2D-S and 3V-CPI, like their predesessor the CPI, are expected to be used on several research aircraft, including aircraft operated by DoD, NASA, NSF and DOE. Measurements of cloud particles using research aircraft is a key component in validating measurements from satellites, which are the main tool used to evaluate global warming and in the development of global climate prediction models. In addition, the 2D-S and 3V-CPI probes will be used in the private sector to better understand processes that lead to improved weather modifiction techniques (e.g., cloud seeding techniques to increase rainfall).

15. SUBJECT TERMS

Cloud Physics, cloud particle instrumentation, optical array probes, global climate change, weather modification

16. SECURITY CLASSIFICATION OF:			17. LIMITATION OF ABSTRACT	18. NUMBER OF PAGES	19a. NAME OF RESPONSIBLE PERSON
a. REPORT	b. ABSTRACT	c. THIS PAGE	UU	81	R. Paul Lawson
					19b. TELEPONE NUMBER (*Include area code*) 303 449 1105

SPEC inc

3022 Sterling Circle – Suite 200, Boulder, CO 80301. (303) 449-1105 (303) 449-0132 (fax)
www.specinc.com

FINAL REPORT

Office of Naval Research
SBIR Phase II Contract No. N00014-02-C-0317

"Development of Novel Instrumentation to Characterize Aerosol Insets and Cloud Particles"

Period of Performance:
July 2, 2002 to July 1, 2007

1. Introduction

SPEC Incorporated was contracted by the Office of Naval Research to develop innovative new technology to measure the size, shape and concentration of water drops and ice particles in clouds. This effort included the main SBIR Phase II contract and two options. The principal objectives of the main SBIR phase II contract and its two options are:

Main Contract: Development of a 2D-S (Stereo) cloud particle imaging probe

Option 1: Determine the feasibility of designing and developing a 3V-CPI probe.

Option 2: Design and fabricate a 3V-CPI probe for use on research aircraft.

One result of the Phase II research was the development of a new cloud particle-imaging probe, the 2D-S (Stereo) probe, which has been installed on four research aircraft and flown in four major field campaigns sponsored by the National Science Foundation (NSF) and the National Aeronautics and Space Administration (NASA). A description of the 2D-S probe and scientific results from field campaigns are the subject of two refereed journal publications (Lawson et al. 2006; Lawson et al. 2007).

A second result is the ongoing development of another innovative cloud particle-imaging probe, called a 3V-CPI, which is essentially a combination of a 2D-S and the SPEC cloud particle imager (CPI). The 3V-CPI is being developed under a joint agreement between the Navy and the NSF, whereby two 3V-CPI probes are being developed in parallel under joint funding from both agencies. Both the Navy and NSF agreed to this arrangement to facilitate development of the 3V-CPI under available funding. The 3V-CPI is a very complex instrument that is being developed for a new NSF research aircraft, a Gulfstream V (G-V), designated HIAPER (High Altitude Platform for Environmental Research). Subsequent to award of Phase II Option 2, the NSF decided to change their approach to modifying the G-V, and instead of seeking public category or restricted category designations, the NSF sought to have the research instrumentation certified in transport category. The distinction is that transport category is the same as the normal category for transporting passengers, while public and restricted category limits occupants to only crew members. The FAA requirements to have the research instrumentation certified in transport category are much stricter than public or restricted categories and require more extensive design, tests and documentation. The decision to certify the G-V in transport category significantly lengthened the timeline required to design and fabricate the 3V-CPI. Thus, the 3V-CPI was not completed at the (mandatory 5-yr) expiration date of this SBIR Phase II contract and will be retained by SPEC after the close of the contract for final assembly and testing.

2. The 2D-S (Stereo) Probe.

The 2D-S (stereo) probe was specifically designed to overcome limitations of existing probes that image cloud particles in the size range from 30 μm to about 1 mm. Here we discuss briefly the limitations of current imaging probe technology and how the new probe overcomes these limitations. Errors due to electro-optical limitations that are inherent in the design of the Particle Measuring Systems (PMS) model 2D-C and Droplet Measurement Technologies (DMT) model CIP imaging probes have been well documented in the literature. Korolev et al. (1991, 1998) and Strapp et al. (2001) have shown that large counting and sizing errors occur with the PMS 2D-C particle-imaging probe when drops pass outside the optical depth of field (DOF). For example, a 100 μm particle can be oversized by nearly a factor of two, undersized by a factor of four or missed all together. Also, small (e.g., 25 μm) particles have a very small DOF (about 1 mm or $1/60^{th}$ of the distance between the probe arms) and very large uncertainties in sample volume.

Additional counting and sizing errors occur due to the relatively slow time response of the PMS 2D-C and DMT CIP probes, resulting from the finite time response of the photodiode array and first stage amplifier. Baumgardner and Korolev (1997), and more recently, Strapp et al. (2001), show that the time response of PMS imaging probes is limited by the time constant of the photodiode array and first stage amplifier, leading to a significant reduction in sensitivity to particles with sizes < ~ 75 μm at airspeeds of 120 m s^{-1} and greater. Similar results have been obtained using a high-speed spinning wire to test the time response of the DMT CIP probe (Nagel 2003 – personal communication)[1].

2.1 2D-S Probe Description

The new 2D-S probe is designed to minimize errors associated with DOF, sample volume uncertainties and time response. A photograph of the 2D-S probe illustrating its functional aspects is shown in **Figure 1**. Two diode laser beams cross at right angles and illuminate two linear 128-photodiode arrays. The laser beams precisely define a rectangular overlap region in the middle of the probe. The 2D-S simultaneously records two independent images of the same particle in the region where the beams overlap, and single images of all particles outside the overlap region.

[1] Dr. Dagmar Nagel of the Institut für Atmosphärenphysik (GKSS) tested CIP probes at the Meteorology Research Institute (MRI) of Japan and at the National Center for Atmosphere Research (NCAR) and found that at 75 m s^{-1}, the smallest diameter wire that could be imaged was 75 μm.

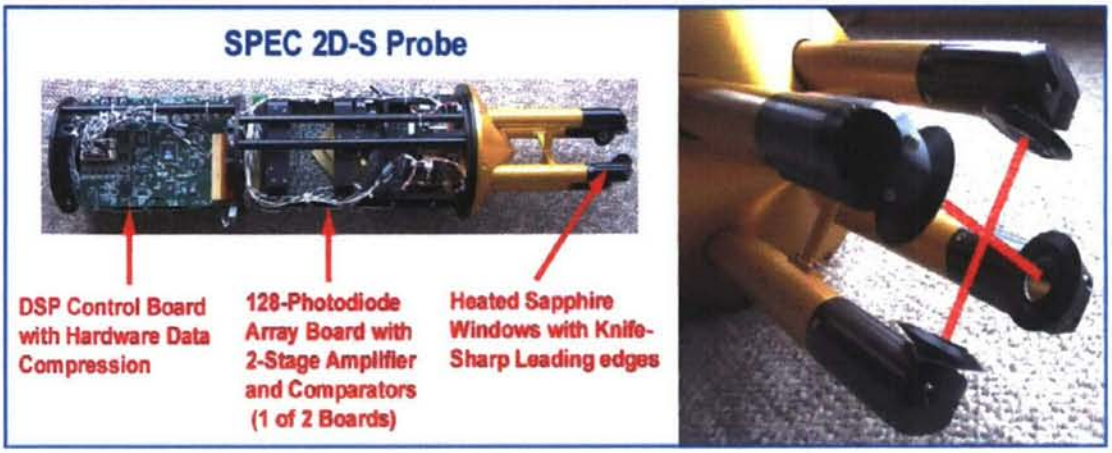

Figure 1. Photographs of the SPEC 2D-S probe. See text for description

The electro-optics used in the 2D-S are on the cutting edge of technology. In order to substantially increase the time response of the photodiode array and first stage amplifier, a new custom 128-element linear photodiode array was built by CentroVision Corporation. Each photodiode in the array is 50 μm instead of 200 μm used in the conventional (PMS and DMT) photodiode arrays, thereby reducing capacitance and increasing speed. The 128-photodiode array chip is positioned on a 12-layer printed circuit board that is specially designed to reduce lead length and increase speed (**Figure 1**). The 2D-S probe response was tested in the laboratory and compared with the response of a PMS 2D-C probe. **Figure 2** shows digital oscilloscope traces of the time response of the 2D-C and 2D-S probes to a sharp (5 ns fall time) negative-going pulse of laser light (i.e., when the laser beam is blocked corresponding to when a particle occults a photodiode). The 2D-C has a ($1/\varepsilon$) response time constant of 760 ns, while the 2D-S probe has a response of 41 ns, which is nearly 20 times faster than the 2D-C probe.

An additional test that demonstrates the extremely fast response time of the 2D-S was conducted by Dr. Dagnar Nagel with a unique high-speed spinning wire calibration unit developed and operated by the Institut für Atmosphärenphysik (GKSS). Using the GKSS calibration unit, the 2D-S was able to completely image an 8 μm wire spinning at a velocity of 233 m s^{-1}. **Figure 3** shows a photograph of the GKSS spinning wire set up and **Figure 4** shows a digital oscilloscope recording of the response of the 2D-S to the 8 μm wire spinning at 233 m s^{-1}. In comparison, using the same GKSS spinning wire set-up, the best response that the PMS 2D-C and DMT CIP probes could achieve was to image a 75 μm wire at 75 m s^{-1}.

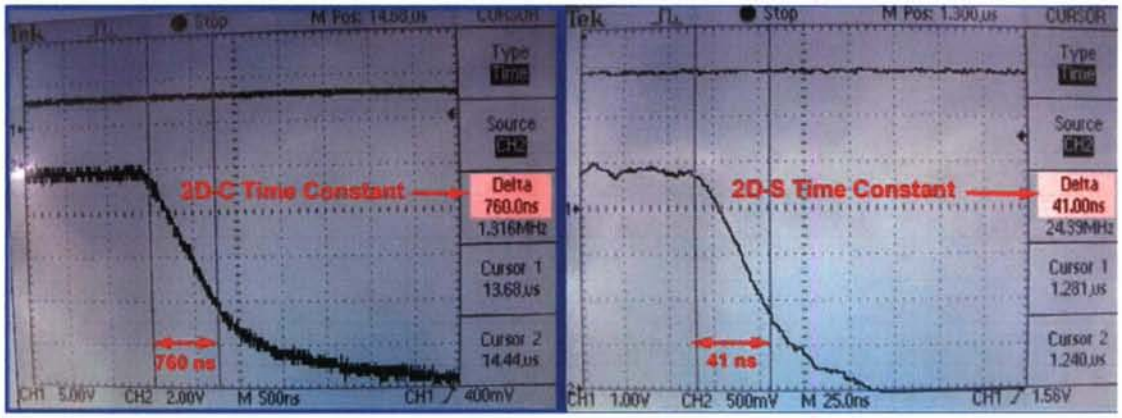

Figure 2. Digital oscilloscope traces and computation of time constants from the front ends of (left) PMS 2D-C probe and (right) SPEC 2D-S probe. The response is generated by illuminating each photodiode array with pulsed laser light; the falling edge simulates shadowing by a particle. The $1/\varepsilon$ time constant of the 2D-S is 41 ns, nearly 20 times faster than the 760 ns time constant of the 2D-C (note that the time scale in the 2D-C plot is 500 ns per box and it is 25 ns per box on the 2D-S plot).

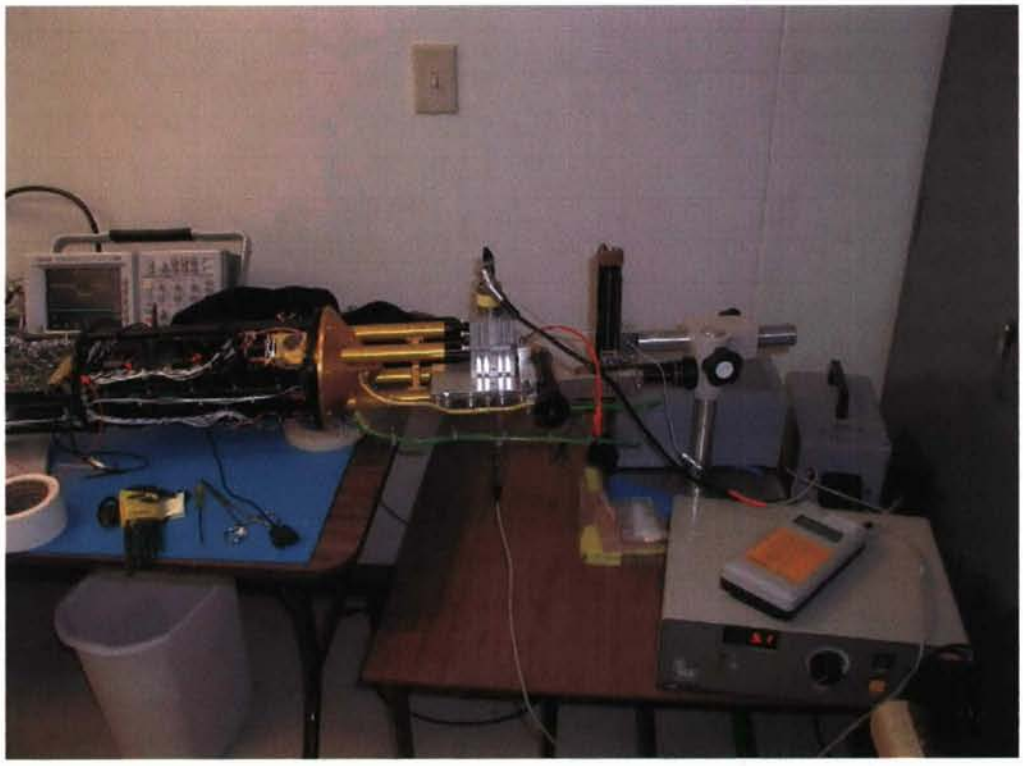

Figure 3. GKSS high-speed spinning wire tests of the 2D-S probe.

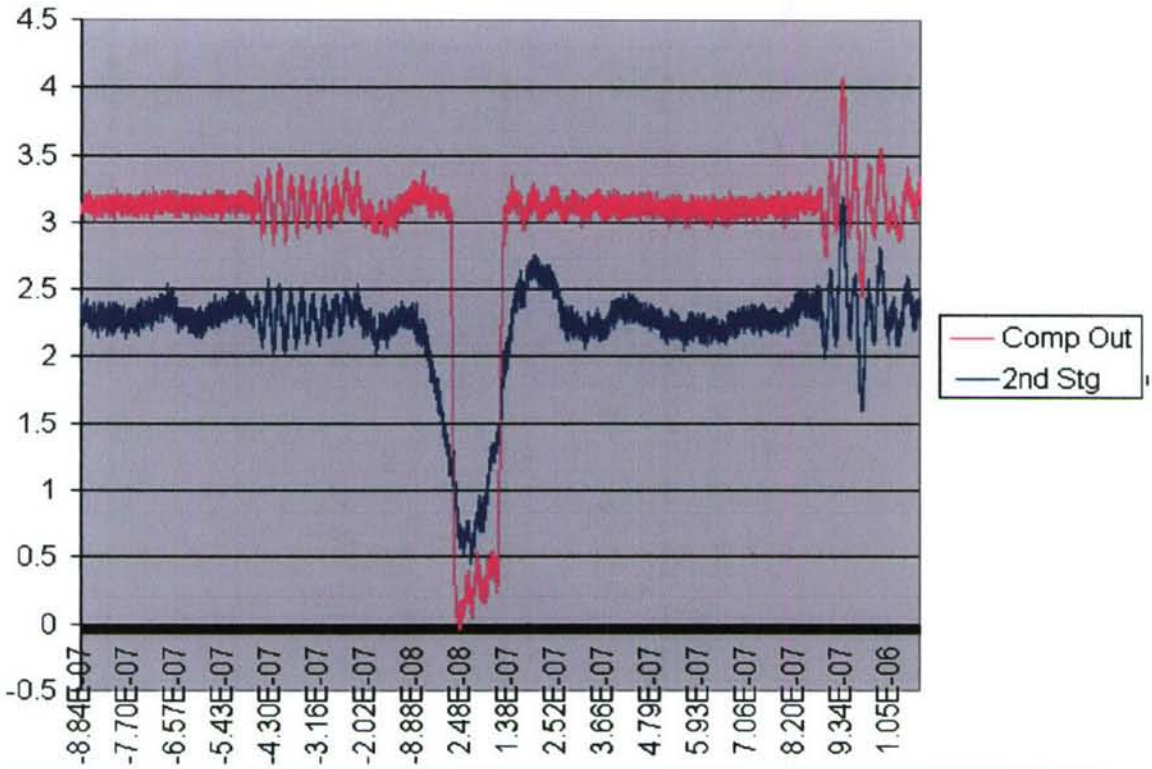

Figure 4. Oscilloscope captured electronics waveforms for an 8 μm wire spinning through the sample volume at 233 m s^{-1}.

A 12-layer printed circuit board with a 32-bit AD-2192 DSP running at 80 MHz controls very large, ball-grid array Complex Programmable Logic Devices (CPLDs) that perform hardware data compression to handle the extremely high data rates (**Figure 1**). The 2D-S probe outputs data at a maximum rate of 20 million samples per second per 128-photodiode array. This amounts to a maximum "raw" data rate of 1.28 Gbytes s^{-1} Since much of the area is "white space" between particle images, hardware data compression reduces this rate by about a factor of ten to a thousand (depending on particle size and concentration), making it possible to transfer data via a high-speed serial interface (HDLC). As discussed above, the standard 2D-C imaging probes miss a substantial fraction of particles < 75 μm in diameter. In the 2D-S, the arrival time of each particle is recorded and the *x*-*y* position of each particle in the overlap region of the two laser beams is recorded. Finally, as shown in **Figure 1**, the 2D-S probe is specially designed with non-wetting, heated sapphire windows that have a knife-sharp leading edge to minimize particle bounce and breakup that is suspected to contaminate imaging probes (Jensen and Granek 2002). Data from the 2D-S are recorded through standard aircraft PMS 2D-C wiring using an Ethernet connection that supports data transfer rates up to 100 mbs.

2.2 Results of Preliminary Flight Tests

The 2D-S probe was installed on the SPEC Learjet and flown on seven research flights during November-December 2003 and eight flights during April-May 2004. In November 2004, it was installed on the National Center for Atmospheric Research (NCAR) C-130 aircraft for the Rain In Cumulus over the Ocean (RICO) project. Data were collected by the Learjet in cirrus clouds, wave clouds and upslope clouds along the Front Range of the Rocky Mountains in Colorado. Data were collected by the C-130 in an upslope cloud along the Front Range, and on 13 missions in warm cumulus clouds near Antigua during the RICO project. **Figure 5** shows photographs of the 2D-S probe installed on the Learjet and the NCAR C-130.

Figure 5. Photographs of the 2D-S probe installed on (left) the SPEC Learjet and (right) NCAR C-130.

Here we present comparisons of 2D-S images with images collected using a cloud particle imager and conventional imaging probes installed on the research aircraft. The 2D-S results are based on preliminary software programs. Because the analysis software is preliminary, we opt to show only particle counts in all cases except one, which is when the probe was in small drizzle drops during RICO. In the RICO case, we incorporated recent work by Korolev (2005) to correct for out-of-focus images, and also, because the drops are small ($\leq$ 150 μm) we believe that artifacts that may be generated from drop shattering and/or incomplete diffraction rings are minimal. The development of mature software capable of automatically rejecting artifacts (e.g., images fragmented from large particles shattering on the probe tips), accurate determination of stereo particles, sizing corrections to non-spherical particles and improving image-to-volume algorithms, is a work in progress.

2.2.1 Mixed-phase Upslope and Wave Clouds

Figure 6 shows examples of 2D-S, CPI and 2D-C particle images collected at –13 ° C by the NCAR C-130 in a mixed-phase upslope cloud east of the Colorado Front Range. The 10 μm resolution, 0.128-cm width of the sample area and high-speed response of the 2D-S probe allow it to show ice particles within a field of small cloud droplets. Compared to the 2D-C particle images, the 2D-S shows considerably more detail of ice crystal structure. **Figure 6** also shows examples of "stereo" views of images that passed through the overlap region of the 2D-S probe. The stereo views reveal details of the three-dimensional structure of particles that cannot be determined from a single shadow-image of the particle.

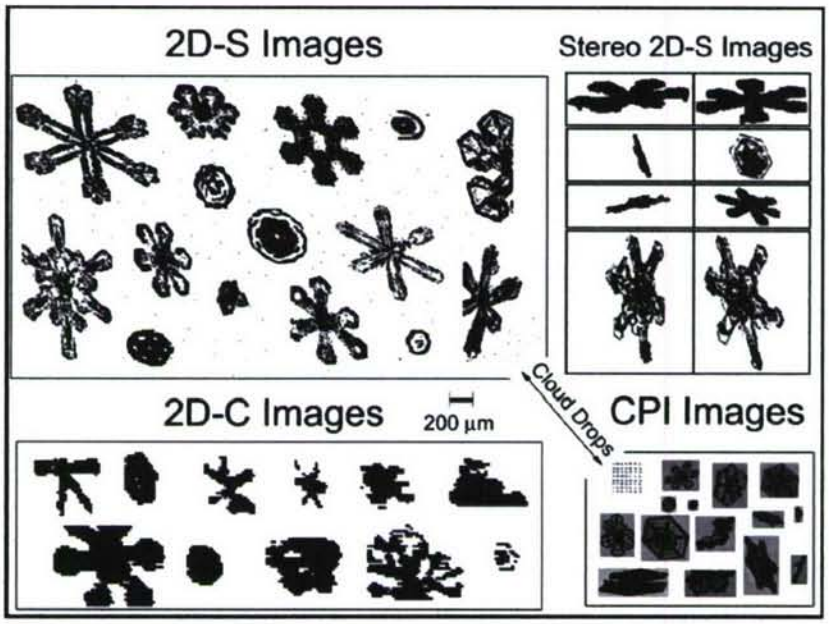

Figure 6. Examples of images from the 2D-S, CPI and 2D-C probes in a mixed-phase upslope cloud investigated by the NCAR C-130 research aircraft. (All of the particle images in this figure have been hand-picked and placed using a graphics tool, i.e., the spatial relationships of the particles are not as observed by the probes.)

Figure 7 shows an example of measurements from the SPEC Learjet during penetration of a wave cloud that formed over the Colorado Front Range. The evolution of particles is shown starting from the top of the figure, which is the leading (western) edge of the wave cloud. The wave cloud undergoes the expected particle evolution at -27 °C (Baker and Lawson 2006), i.e., a transition from supercooled cloud droplets near the leading edge, changing to a mixed-phase region, which rapidly turns into glaciated cloud. The cloud drop size

distribution from an FSSP is displayed at the left of the figure, showing that the size of the supercooled drops ranges from about 4 to 18 μm in diameter, with a mean diameter of 11.6 μm. Both the CPI and the 2D-S probes detect the cloud drops as seen in the sample images. The location of the first ice particles encountered in the mixed-phase cloud region is of interest to cloud physicists, because this relates to ice nucleation, a process that is still poorly understood in wave clouds (Baker and Lawson 2006). The data in **Fig. 7** shows that the 2D-S detects ice particles much closer to the cloud leading edge than either the CPI or the 2D-C probes. The 2D-C does not detect particles with sizes < ~ 100 μm due to the slow response of the photodiode array and front-end amplifier. (Later in this section, we show additional probe comparisons from the RICO project that support this statement.) The CPI easily sees the cloud drops, but since the imaging laser is triggered, the probe response is dominated by the high concentration of drops, so it is often inactive when larger (ice) particles enter the sample volume. The ability of the 2D-S to detect small ice "earlier" into the traverse of the wave cloud may provide the basis for a better understanding of the ice nucleation process in clouds.

2.2.2 Cold Wave and Cirrus (Ice) Clouds

Figure 8 shows examples of small spheroidal particles and budding rosettes in a cold (- 45 ° C) cirrus cloud. The figure is configured to show the transition from a region of small particles to budding rosettes and highlights how the 2D-S probe sees these particles and the 2D-C barely responds. This is emphasized by the total particle count, where the 2D-S recorded 268,897 particles compared with 264 particles seen by the 2D-C over a 40 s time period. Also, the shapes of many of the larger (> ~ 100 μm) budding rosettes, which are confirmed by the CPI images, are discernable and can be identified as rosettes in the 2D-S imagery, whereas the 2D-C sees only 1 – 5 pixel images whose shape is indistinguishable. **Figure 9** shows another example of small ice particles and budding rosettes in a cold (- 50 ° C) cirrus cloud. In this figure, six 2D-S image strips have been aligned horizontally. Notable in this figure is the large number of small ice particles in the absence of large particles that could have shattered on the probe tips. Observations of high concentrations of small ice particles in cirrus have been reported by some investigators (Lawson et al. 2001; Gayet et al. 2002; Lawson et al. 2006), but questioned by others as being a possible result of crystal shattering. The 2D-S probe may shed new light on this issue.

Wave Cloud

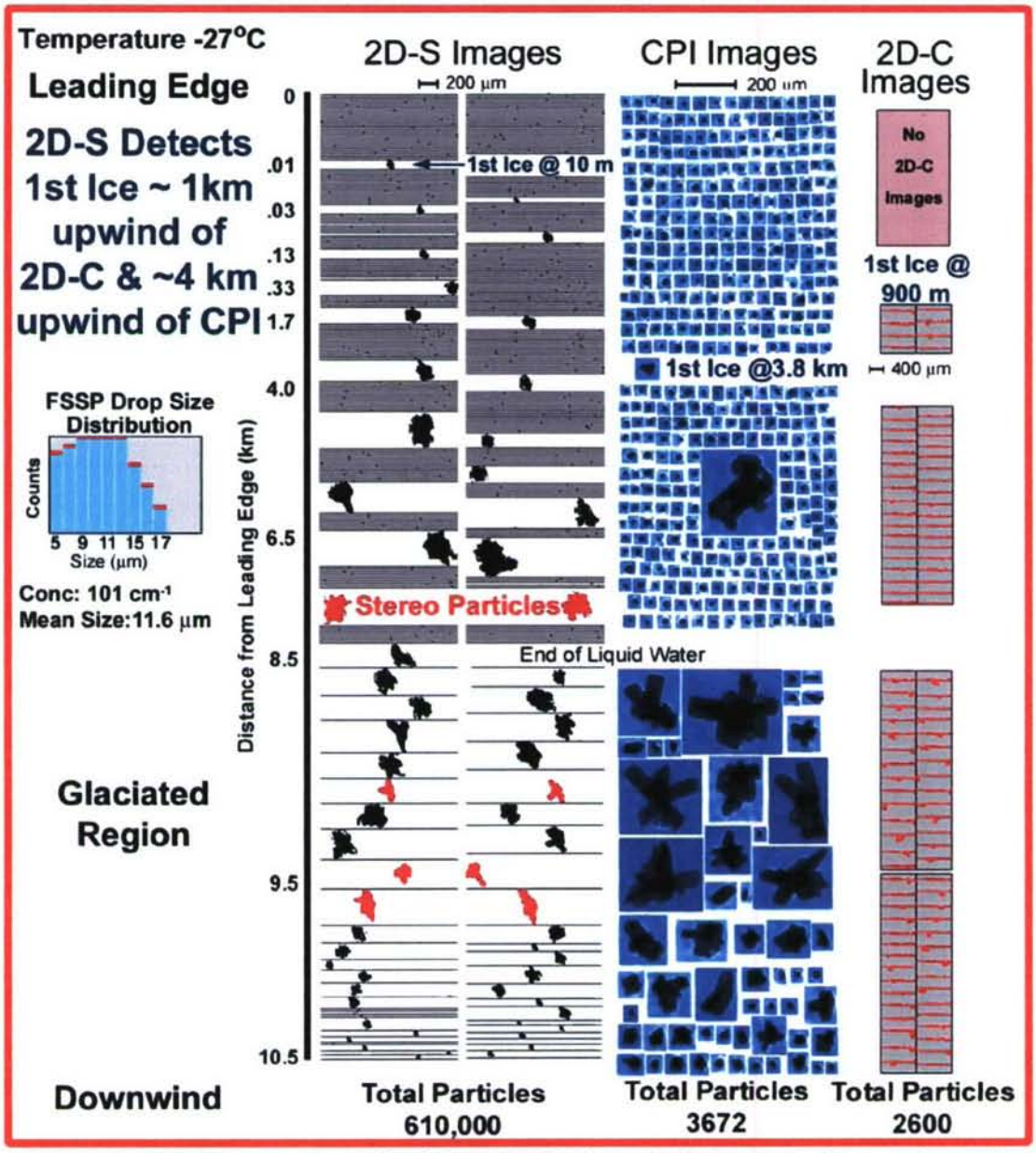

Figure 7. Examples of 2D-S, CPI and 2D-C particle images observed starting from (top of figure) the leading edge of a wave cloud containing supercooled drops, extending into the mixed-phase region and terminating (bottom of figure) in the glaciated region. The FSSP cloud drop distribution near the leading edge is shown at the left. Examples of 2D-S stereo images are shown in red.

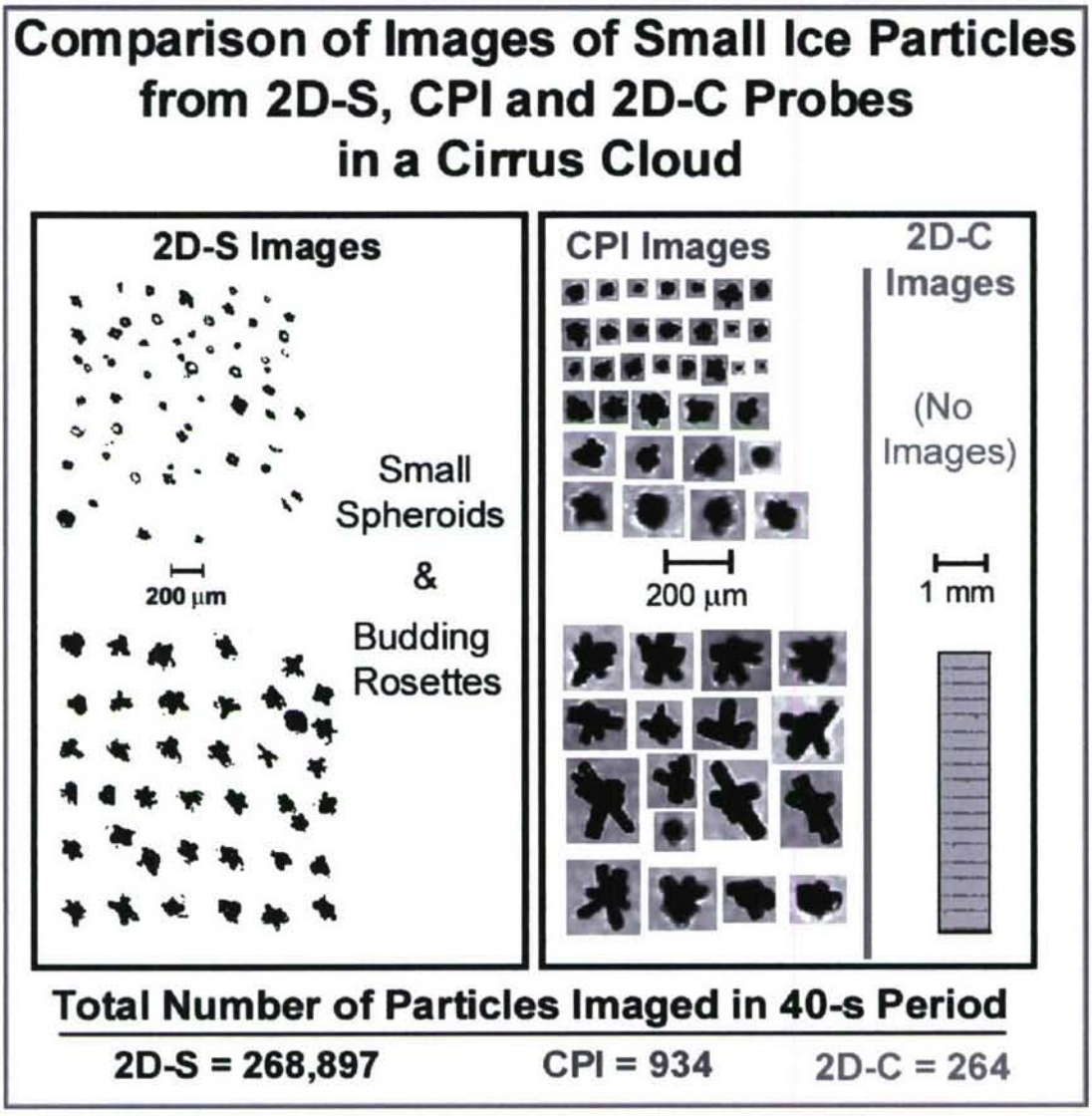

Figure 8. Examples of images from the 2D-S, CPI and 2D-C probes in a cirrus cloud (-45 ° C) investigated by the SPEC Learjet.

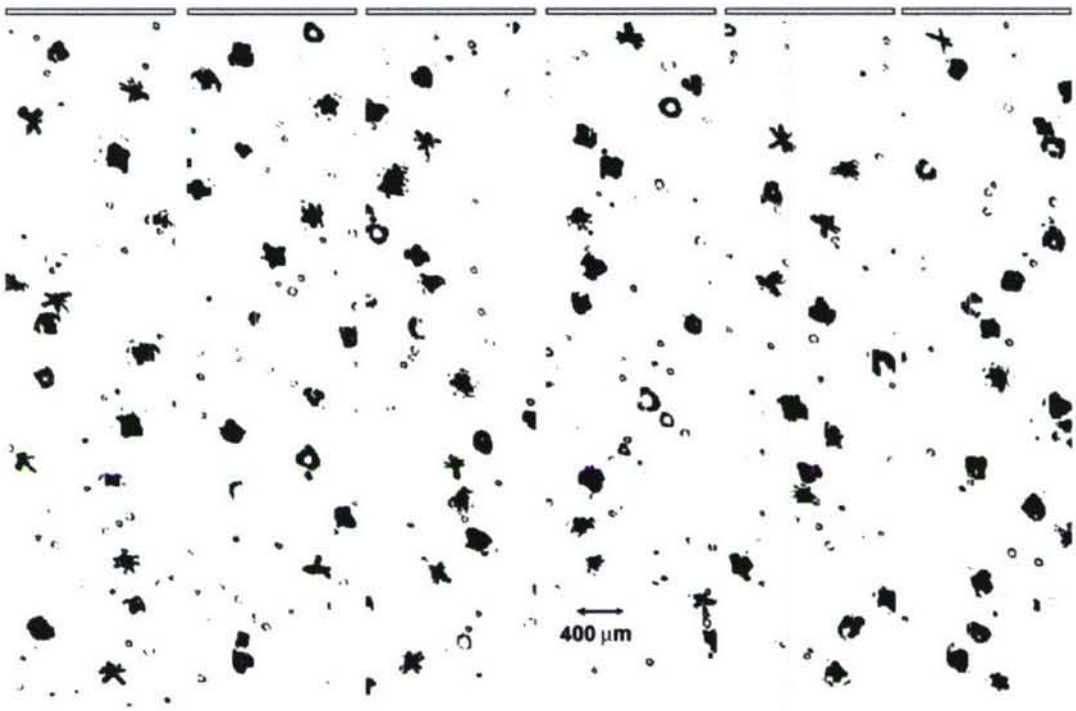

Figure 9. Example of images of budding rosettes, irregular-shaped particles and small particles recorded by the 2D-S during a test flight in a thin cirrus cloud at –50 °C.

Figure 10 shows image data from several particle imaging probes on the SPEC Learjet and WB-57F research aircraft, operated by the National Aviation and Space Agency (NASA). Both aircraft participated in the Mid-Latitude Cirrus Experiment (MidCiX) and flew a coordinated mission in a system of persistent, vertically stacked wave clouds. The wave cloud system was located over the Colorado Front Range and had a cloud base temperature of –43 ° C and a cloud top temperature of –63 ° C. A Rosemount icing probe (Mazin et al. 2001; Cober et al. 2001) indicated there was no detectable supercooled liquid water drops in these clouds.

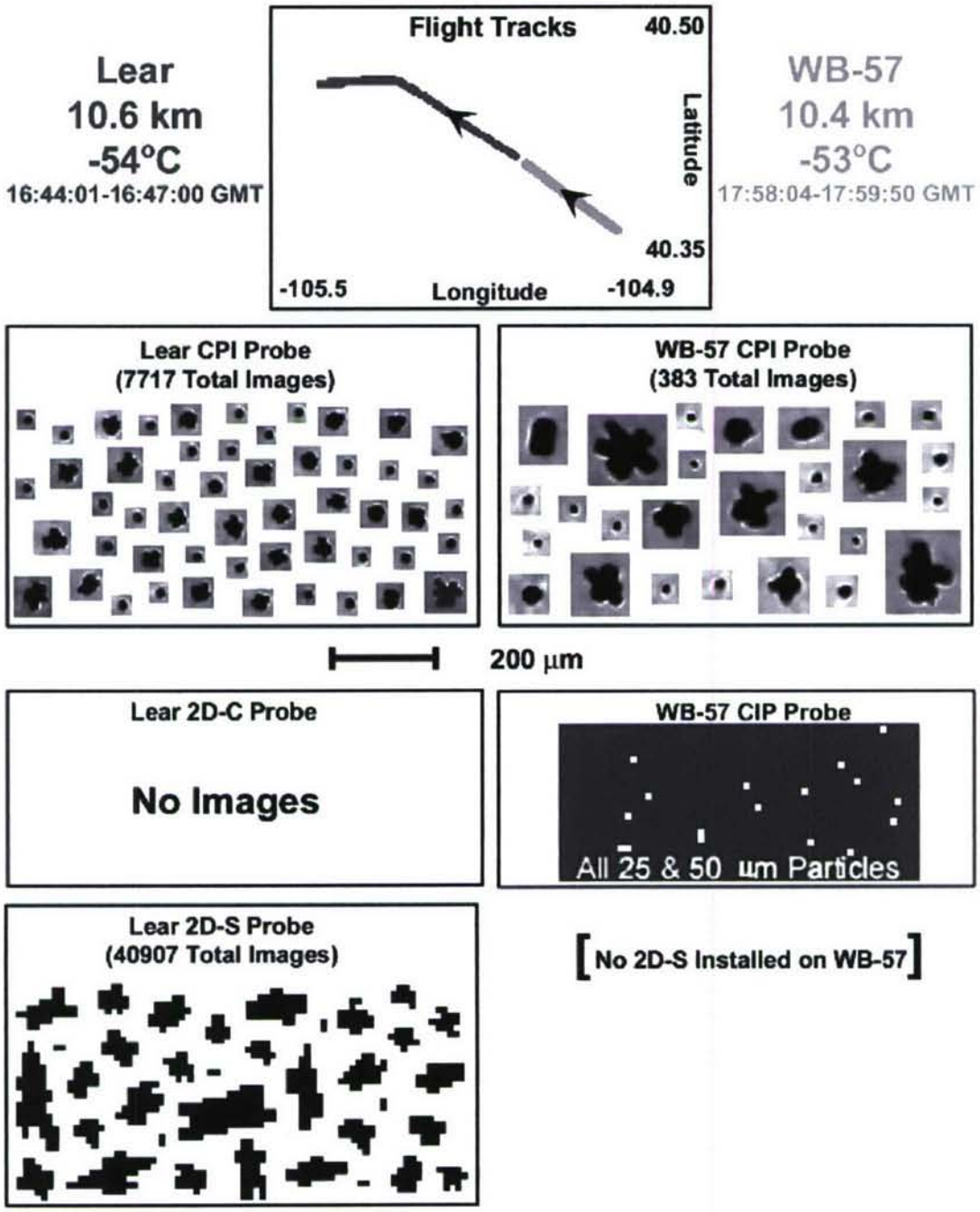

Figure 10. Comparison of particle images from various probes installed on the SPEC Learjet and NASA WB-57 in a cold wave cloud where the two aircraft penetrated the same region of cloud.

Figure 10 shows portions of the Lear and WB-57 flight tracks as they penetrated the same wave cloud, based on video records and flight notes from both aircraft. The Learjet penetrated the cloud at 10.6 Km (–54 ° C) and the WB-57 penetrated 200 m lower in the cloud at –53 ° C. Both aircraft carried CPIs and 2D-C type imaging probes. The 2D-C probe on the Learjet was manufactured by PMS. The WB-57 flew a DMT cloud, aerosol and precipitation spectrometer (CAPS) probe (Baumgardner et al. 2001), which is a composite of probes, one of which is a DMT CIP. The CPI particle images in **Fig. 10** show that both aircraft penetrated regions with small spheroidal particles and budding rosettes (i.e., rosettes with short branches). The maximum dimension of the budding rosettes observed by the Lear is about 75 μm, while the WB-57 recorded some slightly larger particles, with maximum dimension of about 125 μm, during its penetration 200 m lower in the cloud. Of note is the observation that during the entire penetration (and actually during the entire flight), there were no particle images recorded by the Learjet PMS 2D-C probe. The DMT CIP probe, on the other hand, only recorded images that were 25 and 50 μm (one and two pixels). The true airspeed of each aircraft during the cloud penetrations was about 160 ms^{-1}. Since the CPI imaged particles up to 125 μm at the same time that the CIP recorded 25 and 50 μm images, it would appear that the front-end electro-optics of the CIP were not fast enough to capture the entire particle image. **Figure 10** shows that the 2D-S probe recorded particle images as small as 10 μm and with the largest image dimension being 200 μm during the penetration. However, since the 2D-S electro-optics are fast enough to accurately capture the image, it is possible that the 200 μm images are out-of-focus particles that are actually about 125 μm in size (see Korolev et al. 1998).

2.2.3 Warm Cumulus (Water) Clouds

The RICO project addressed several aspects of the warm rain process, one of which is evolution of the droplet spectra in small, warm cumulus clouds (Rauber et al 2003). The 2D-S probe can detect and size drops from 10 μm to > 1 mm in diameter, so it is capable of measuring the evolution of the drop size distribution in the critical size region where cloud drops coalesce into drizzle and eventually become raindrops. Measurements of the drop size distribution in warm cumulus have been made during several previous projects using PMS 2D-C and 260X probes (e.g., Blyth et al 2003; Jensen and Granek 2002). We show here that these instruments appear to have improperly measured the critical size range of drops with diameters from about 25 to 150 μm.

Figure 11 shows examples of 2D-S and 2D-C images, along with PSDs from the FSSP, 2D-S and 2D-C during a 250-s penetration in a cloud region on 7 January 2005. During this time period, the C-130 encountered cloud and drizzle drops that produced in-focus 2D-S images that extended out to 150 μm in diameter. The FSSP and 2D-C data were processed using standard NCAR processing software (NCAR 2003). The 2D-C depth-of-field correction for

sample volume comes from the PMS 2D-C manual (NCAR 2003), which uses a value of $c \approx 6$ in (1). The 2D-S images are shown exactly as they were recorded. Based on theory shown in Korolev et al. (1998) and algorithmic simulations recently developed for SPEC by Korolev (2005), out-of-focus 2D-S images (i.e., "donuts") with maximum dimensions $\geq$ 30 μm were automatically resized. The Korolev (2005) algorithm uses the ratio D_{area} / D_{max}, where D_{area} and D_{max} are explained in detail in Korolev et al. (1998).[2] The Korolev (2005) algorithm is only applied to the portion of the 2D-S PSD $\geq$ 30 μm because smaller images do not contain enough information (e.g., Poisson spot) to reconstruct the original particle size. The concentration of 2D-S images $\leq$ 20 μm was adjusted using depth-of-field and sample volume corrections based on (1) with a value of c = 8, which was determined from laboratory calibrations with glass beads. No attempt was made to eliminate artifacts, however, in the RICO PSD presented here, there is little evidence of drop shattering or other artifacts. Also, the occurrence of images "joined together" is minimal and can be ignored.

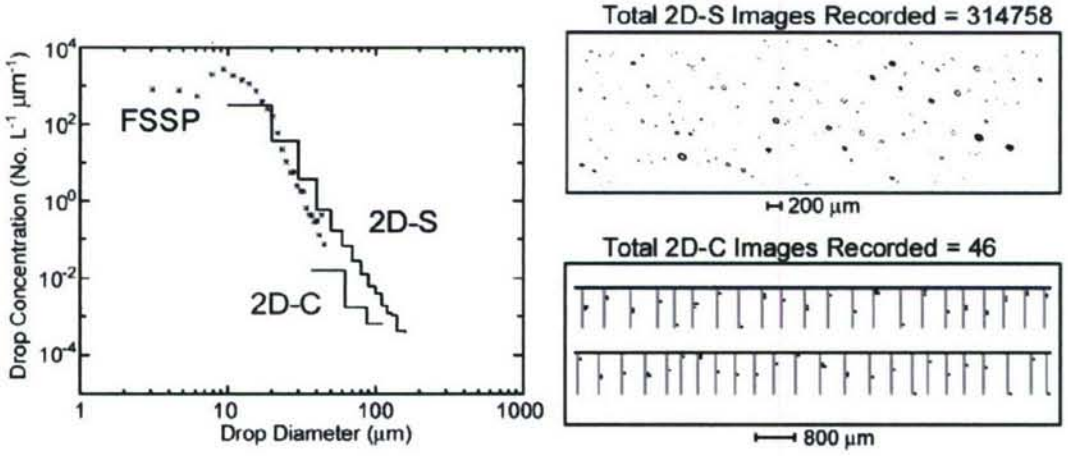

Figure 11. Comparisons of (left) PSDs from FSSP, 2D-S and 2D-C and (right) droplet images for the time period from 185340 to 185750 on 7 January 2005.

2D-C images from 50 to 150 μm (2 to 6 pixels) cannot be resized due to the poorer instrument response time and pixel resolution. The 2D-C drop size distribution was computed using depth-of-field corrections published in the PMS 2D-C manual. As shown in the **Table 1**, the 2D-C recorded a total of 46 images while the 2D-S horizontal channel recorded 314,758 images during the same 250-s time period; 90 of the 2D-S images had diameters of 100 μm or greater. A comparison of the number of particles in **Fig. 11** shows that the 2D-C recorded about 0.1% of the particles seen by the 2D-S in the size range from

[2] The algorithm developed by Korolev is described in Korolev (2005), which can be viewed at www.specinc.com, and will be the subject of a future paper by Korolev and co-authors.

about 30 to 150 μm, and the 2D-C PSD was about an order of magnitude lower than the 2D-S in this size range.

Table 1. Comparison showing response of 2D-S probe horizontal (H-channel) with expected counts from 2D-C probe assuming theoretical instantaneous time response and actual counts for time period with maximum drop diameter of (left) 150 μm and (right) maximum drop diameter of 120 μm. Data shown at left is from RICO for 250-s time period from 185340 to 185750 on 7 January 2004, and data shown at right is a continuous 65-s time period within the 250-s time period.

Maximum Drop Size = 150 μm

2D-S Size (μm)	H-Channel 2D-S Counts	2D-C Size (μm)	Expected 2D-C Counts	Actual 2D-C Counts
10	181273			
20	95271	25	89357	0
30	27989			
40	6075	50	3969	30
50	1992			
60	1166	75	595	9
70	469			
80	326			
90	106	100	82	7
100	60			
110	19	125	8	0
120	8			
130	3	150	0.5	0
140	0			
150	1			
160	0			

Maximum Drop Size = 120 μm

2D-S Size (μm)	H-Channel 2D-S Counts	2D-C Size (μm)	Expected 2D-C Counts	Actual 2D-C Counts
10	30876			
20	18564	25	16585	0
30	4508			
40	895	50	622	0
50	326			
60	222	75	97	0
70	74			
80	48			
90	19	100	13	0
100	9			
110	2	125	0.8	0
120	1			
130	0			

Of the total images recorded by the 2D-S, 30 of the images had diameters > 100 μm and the 2D-C probe did not record any images > 100 μm. Therefore, even though a single channel of the 2D-S has 1.75 times the sample volume of the 2D-C for drops < 150 μm, the absence of recorded 2D-C images > 100 μm cannot be explained by sampling statistics (**Table 1**). The 260X probe recorded only 6 drops during the same 250-s time period.

The 2D-C probe did not record any images larger than 100 μm in diameter during the 250-s period, which suggests that the few images it did record may actually have been out-of-focus images of larger (100 to 150 μm) drops. This is supported by the data shown in **Table 1,** which shows the 2D-S horizontal (H-) channel counts per bin for 65-s during the 250-s period when the 2D-C did not record any images. During this 65-s period, the 2D-S probe H-channel recorded

55,544 drop images, 375 with diameters from 60 to 120 μm and 12 with diameters 100 μm and larger. Since the 2D-C probe did not record any images, this suggests that the threshold drop size that the 2D-C probe detected was about > 100 μm at the 103 m s^{-1} airspeed of the C-130. With this information, we can hypothesize that the images recorded by the 2D-C in the 50 to 100 μm size bins during the 250-s time period (**Fig. 11**) are actually drops in the size range from 100 to 150 μm that produce smaller images due to inadequate time response of the probe.

Another interesting observation drawn from **Fig. 11** is that if one extrapolates the PSD from the FSSP to the 2D-C, they form a relatively straight line, implying that the 2D-C PSD is reasonable. Given that it is likely that the 2D-C is recording measurements in the 25 to 100 μm size range that are actually out-of-focus images of larger drops, one can draw the conclusion that many of the PSDs previously reported in this size range are erroneous. To be more specific, measurements from the 2D-C with time constants similar to the NCAR instrument, when operated at 100 m s^{-1} or faster, likely do not detect (spherical water) particles with sizes < 100 μm. If particles > 100 μm are present, the out-of-focus images from these particles may artificially create a pseudo PSD from 25 to 100 μm.

A comparison of measurements from the (independent) vertical and horizontal 2D-S channels is similar to comparing the response to two independent imaging probes. Previous efforts to compare the output from several 2D-C imaging probes installed on the same aircraft have shown that errors in concentration of up to 50% are expected (Gayet et al. 1993). Drop size distributions and time-series of drop concentration from both the vertical and horizontal 2D-S imaging channels are shown in **Fig. 12**. The good agreement in the time-series of drop concentrations between the vertical and horizontal channels is encouraging. This level of agreement is not always present in the RICO data set, because the functioning of one channel or the other is sometimes degraded in the salty tropical environment due to window contaminants, and/or optical alignment issues.

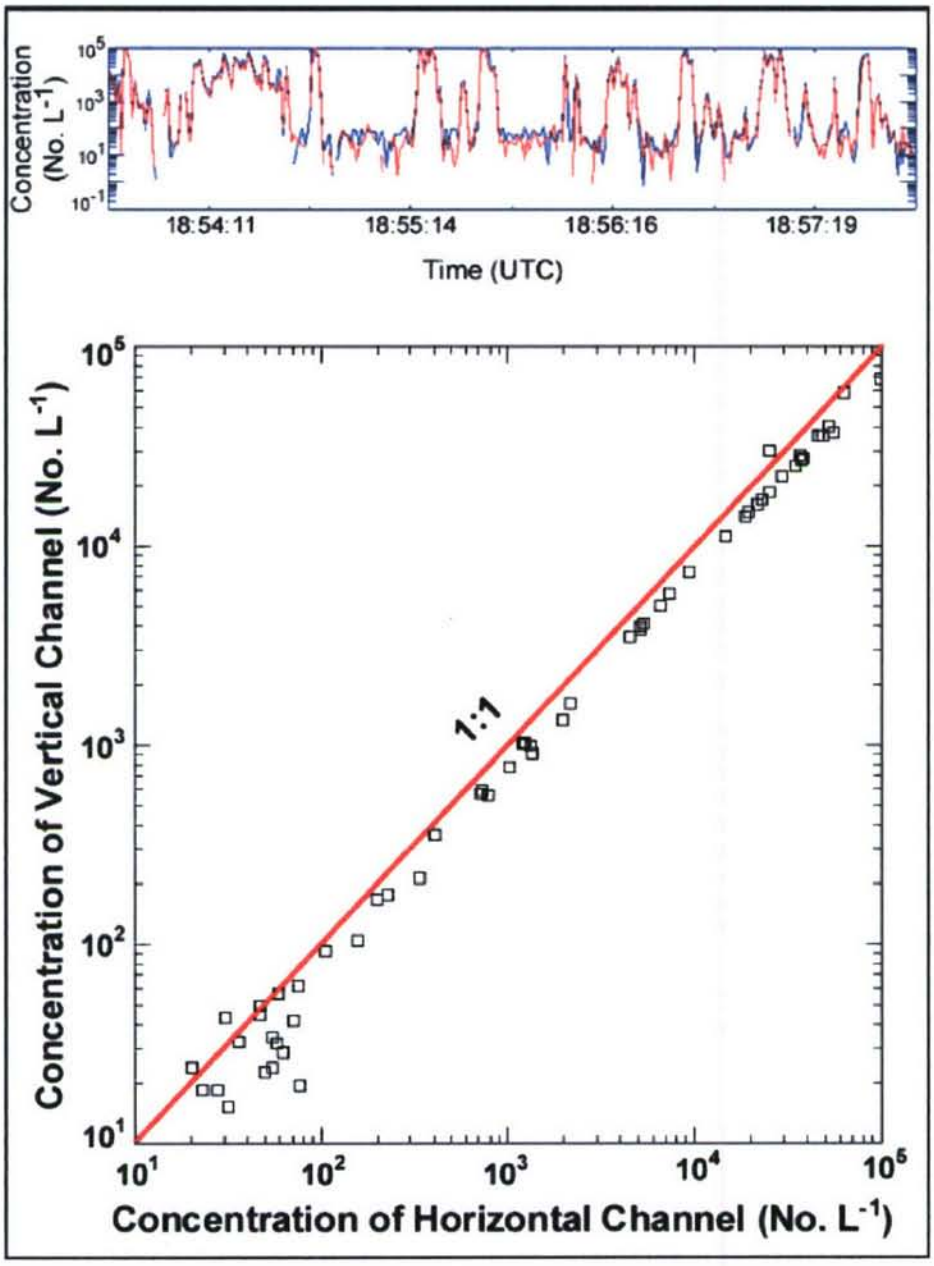

Figure 12. Comparison of (top) time-series data and (bottom) scatter plot for the "vertical" and "horizontal" channels of the 2D-S probe. Occasional data dropouts in the time series are when a channel is in overload. Each square in the scatter plot is a 4-s average. Measurements are for the cloud penetration from 185340 to 185750 on 7 January 2005.

3. Use of the 2D-S on NASA Field Campaigns.

The Navy gave permission for SPEC to install the 2D-S on the NASA DC-8 for the NASA African Monsoon Multidisciplinary Analysis (NAMMA) project, and on the NASA WB-57F for the Costa Rica – Aura Validation Experiment (CR-AVE). The 2D-S performed exceptionally well in both of these projects. A peer-reviewed paper that discusses data collected by the 2D-S installed on the NASA WB-57F in subvisible cirrus clouds in the tropical tropopause layer is contained in Appendix A.

4. Development of the 3V-CPI

As explained in **Section 1**, the Navy 3V-CPI is being developed in parallel with the NSF/NCAR HIAPER 3V-CPI. A Critical Design Review (CDR) was presented to the NCAR in June 2006. The CDR is equally applicable to the development of the Navy CPI and is reproduced below. Since the time of the CDR until the termination of the Phase II contract (2 July 2007), development of the 3V-CPI has continued and all mechanical, electrical and optical components have been designed and a large majority of the parts were fabricated. Since 2 July 2007, SPEC has continued development of the Navy 3V-CPI with internal research and development funds. Initial laboratory tests of the subsystems are proceeding and final tests, including flight tests on the HIAPER G-V are expected to be completed by June 2008, at which time SPEC plans delivery of the 3V-CPI to the Navy for application in the VOCALS-REx project planned for October 2008.

3V-CPI Critical Design Review
(Presented to the Research Aviation Facility at the National Center for Atmospheric Research in June 2006):

SPEC, INC.
3V-CPI CRITICAL DESIGN REVIEW

Presenters: Darren O'Connor, Pat Zmarzly, Paul Lawson

Phone Number: 303.449.1105
Emails:
Darren@specinc.com
Pzmarzly@specinc.com
Plawson@specinc.com

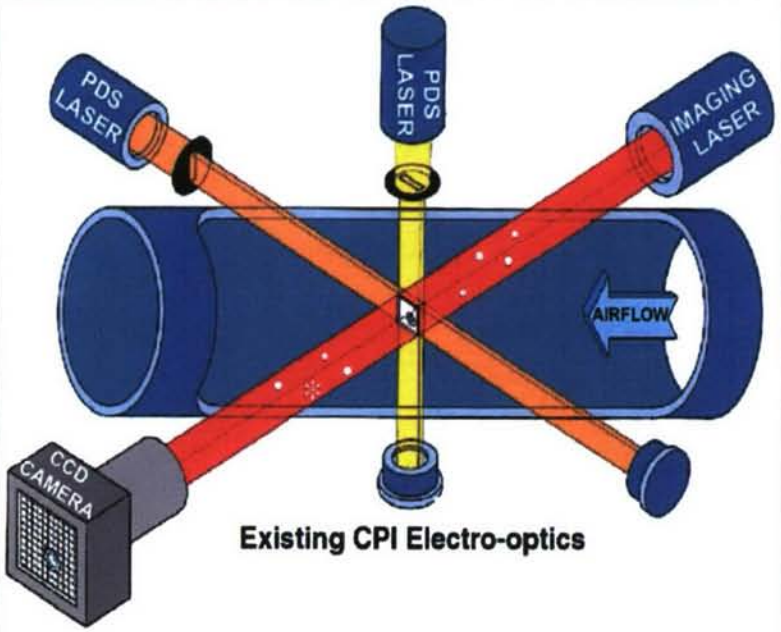

Existing CPI Electro-optics

Examples of CPI Images

Photograph of CPI Installed on the NASA WB-57

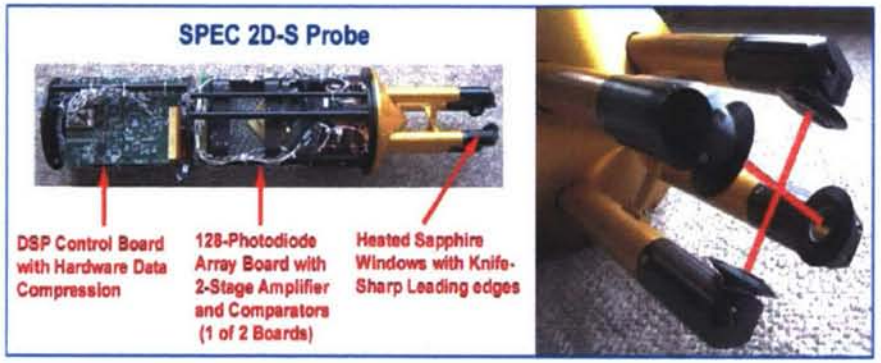

Comparison of 2D-S, CPI and 2D-C images in a Mixed-Phase (Upslope) Cloud

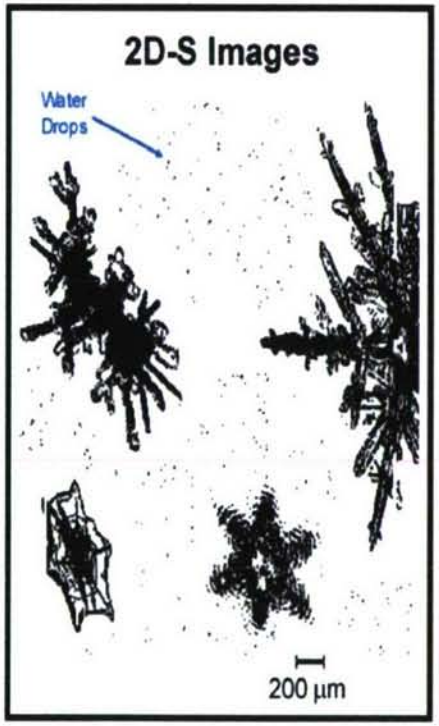

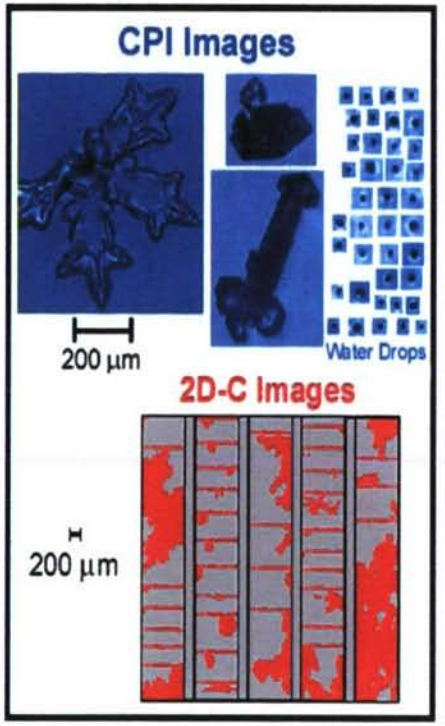

Solidworks Drawing Showing Internal Structure of 2D-S/CPI with 2D-S Electro-Optics and Basler 504K Digital Camera

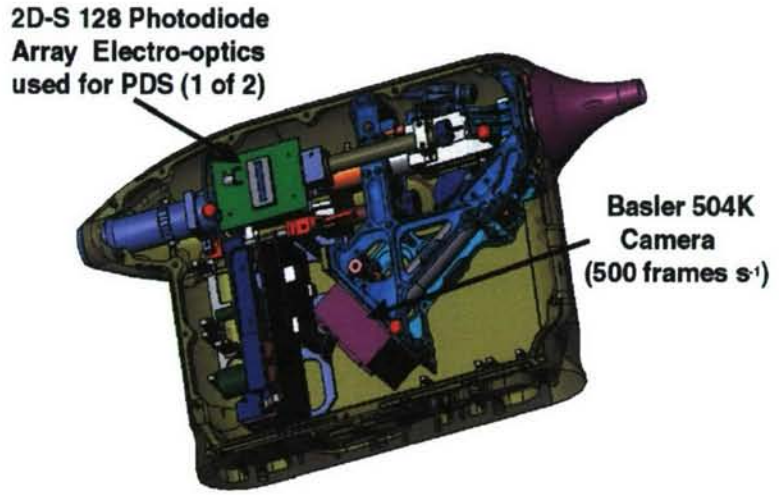

Schematic Showing Electro-Optics of the 2D-S/CPI Imaging Probe

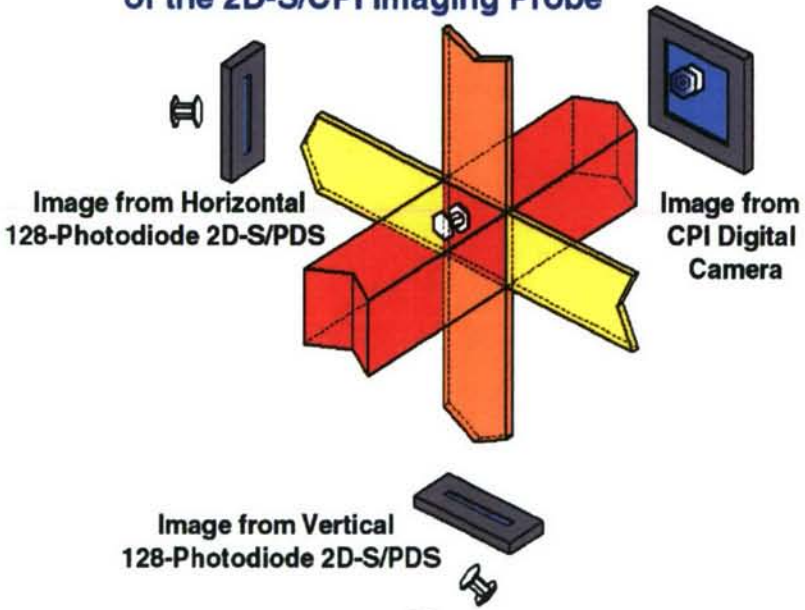

GOALS FOR JUNE 2006 CRITICAL DESIGN REVIEW

- PURCHASE CPI QUAD PROCESSOR COMPUTER SYSTEM AND BEGIN OPTIMIZING IMAGE PROCESSING
- TARGETING COMPLETION OF FINAL OPTICAL SYSTEM DESIGN INCLUDING FOLD PATHS (2D-S ARRAY BOARD ORIENTATION) AND ALIGNMENT STRATEGY
- TARGETING COMPLETION OF PACKAGING TOP LEVEL DESIGN INTEGRATING OPTICAL SYSTEMS, SAMPLE TUBE GEOMETRY ,AND INSTRUMENT PYLON STRUCTURE
- TARGETING ELECTRONICS PCB DESIGN FOR ALL ELECTRICAL SYSTEM BOARDS.
- QUOTES AND DELIVERY TIMES FOR ALL SYSTEM CONNECTORS AND FAA APPROVED CABLE COMPONENTS

CPI-IMAGING SYSTEM COMPUTER THROUGHPUT ANALYSIS

Performed exhaustive review of state of the art multiprocessor computer systems. Selected and purchased system with the following:

- **Rack mount 3U chassis with 8 drive bays**
- **High throughput motherboard**
- **Dual Intel dual-core Xeon CPU's with Hyper threading capabilities (effectively quad-CPU, but with faster inter-processor and motherboard communications)**
- **On-board SATA RAID controller**
- **2GB main memory**
- **High performance PCI-e graphics**
- **High speed image capture device**

IMAGING SYSTEM HARDWARE COMPONENTS

Hardware Components (cont.)

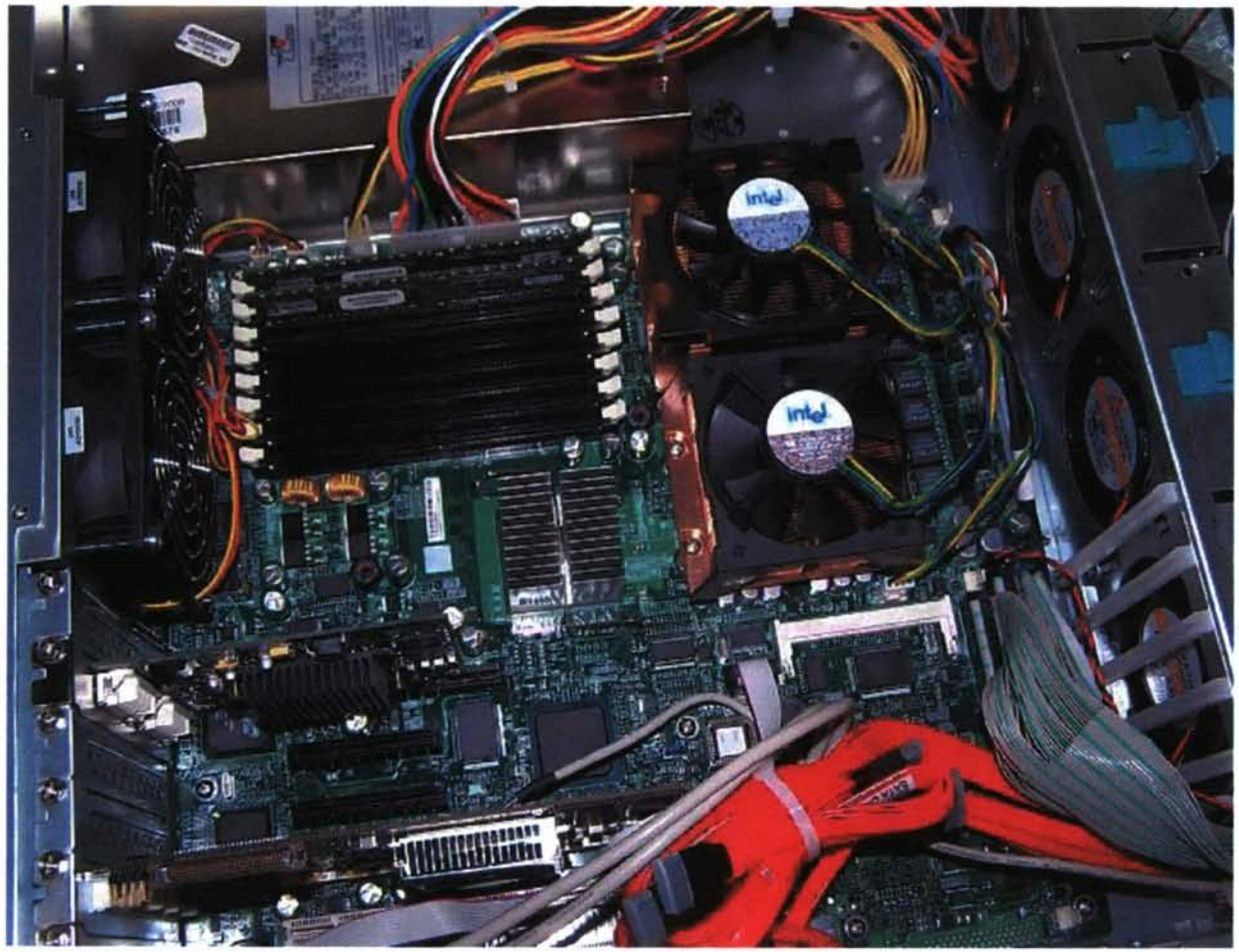

MIKROTRON CAMERA WITH EDT FIBER TRANSCEIVER SYSTEM

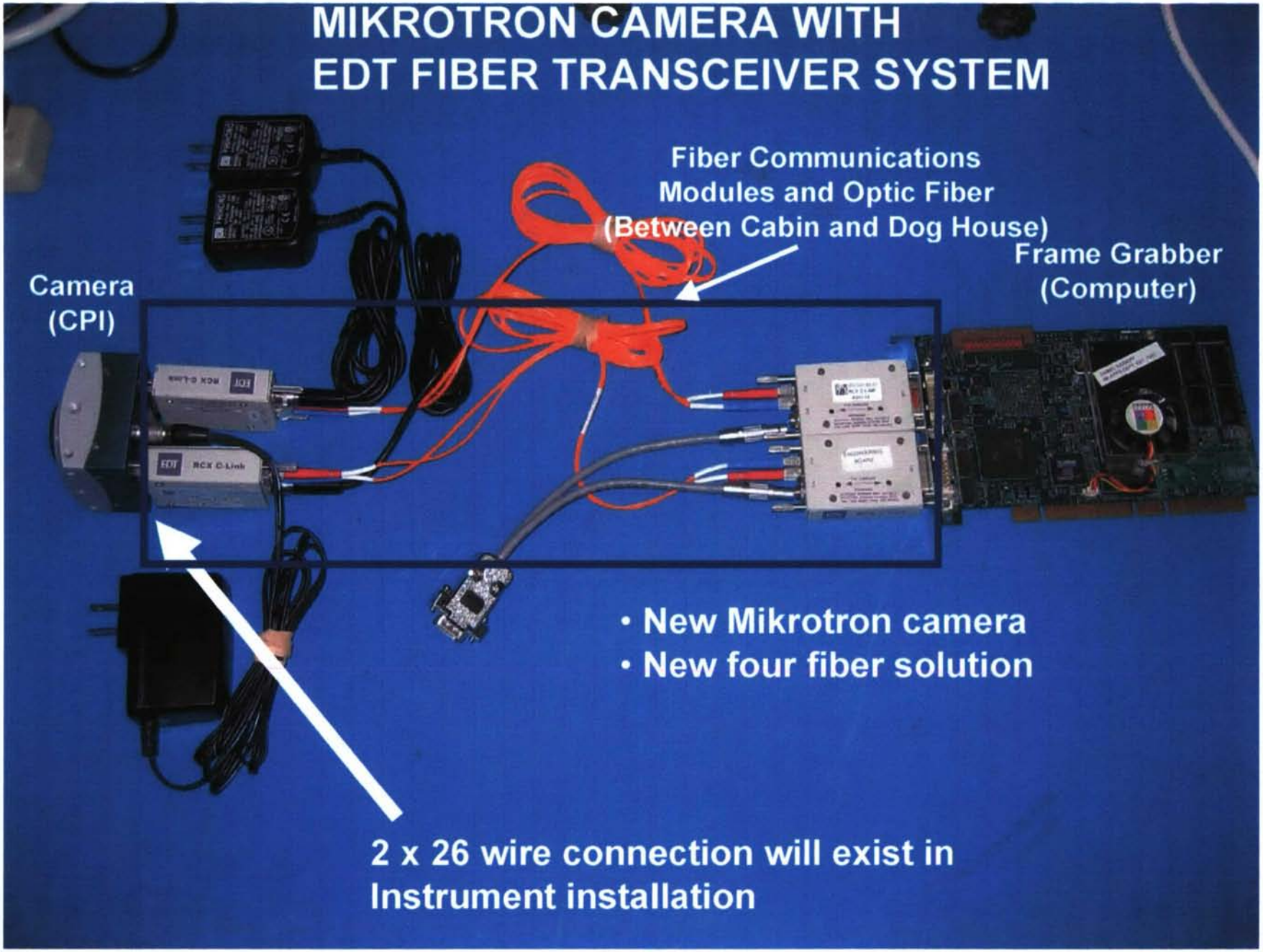

TEST SETUP

- We used VisionNow - Boulder Imaging's real-time imaging capture / processing software in simulation mode.
- We created test images with the size of 1024x1024, and 8 bits per pixel.
- In each image, we generated 10 random particles per frame, with width and height ranging between 4 and 25 pixels. This matches the number of particles expected in the highest concentration clouds.

PERFORMANCE DATA

- **Simulations show that the particle detection algorithm will process 750 frames per second while operating with 8 parallel threads.**

- **The camera has a maximum frame rate of 460 at 1kx1k resolution. Therefore the image processing capability exceeds the camera output rate**

- **With the addition of communication to the probe and the data processing, and additional User-interface functions, we expect a slight reduction in maximum image throughput per second; however the achieved throughput exceeds the camera capabilities**

FIBER / POWER INTERFACE BOX – CDR VERSION

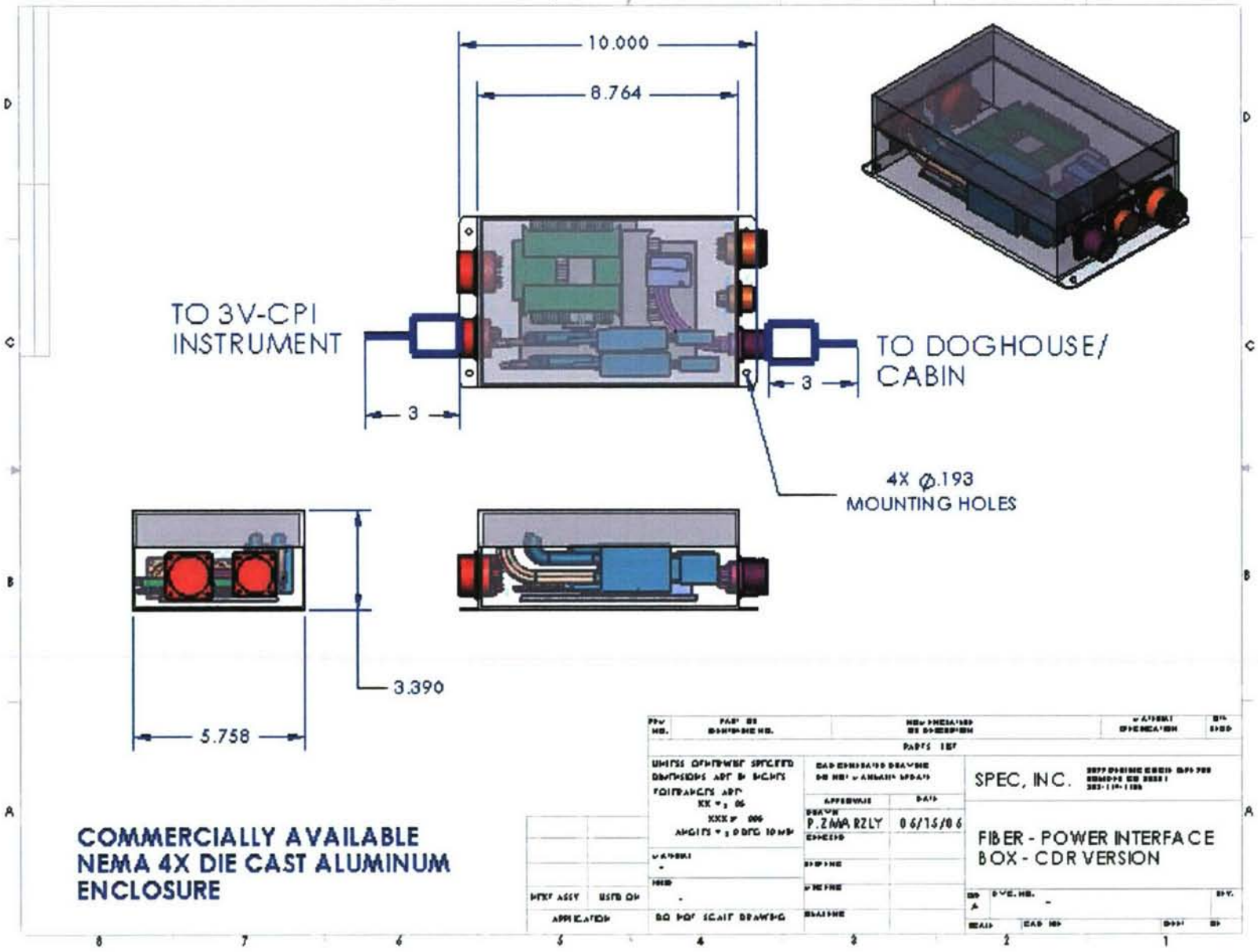

COMMERCIALLY AVAILABLE NEMA 4X DIE CAST ALUMINUM ENCLOSURE

FIBER / POWER INTERFACE BOX DETAILS

- Uses off-the-shelf die cast aluminum enclosure (NEMA 4X).
- Contains power distribution board (conformal coated).
- Contains fiber transceivers.
- Minco temperature controller used to keep fiber transceivers above 0 C (Min. operating temperature) and prevent condensation.
- Requires 4 screw points for mounting.
- Requires space to mount the interface box with 3V-CPI instrument connectors on bottom of pylon.

CONFLICT BETWEEN FIBER/POWER INTERFACE BOX AND 3V-CPI CONNECTORS WITHIN NCAR PROPOSED MOUNT STRUCTURE

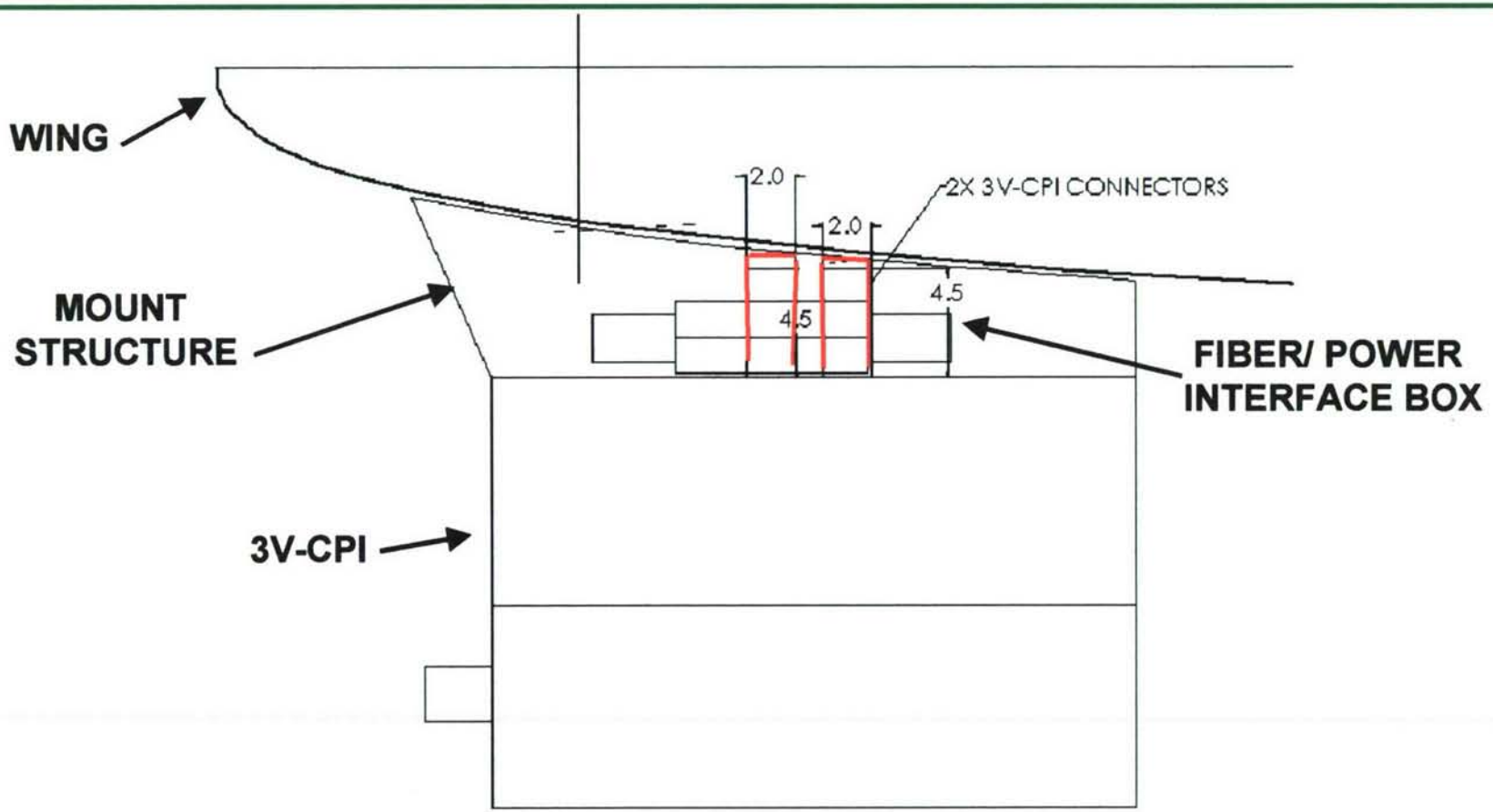

- MOUNT STRUCTURE NEEDS TO ACCOMMODATE INSTRUMENT CONNECTORS AND FIBER / POWER INTERFACE BOX- CABLE PASS TO DOGHOUSE / CABIN
- NCAR PRELIMINARY MOUNT STRUCTURE NEEDS TO BE MODIFIED
- ACCESS REQUIRED TO MATE CONNECTORS AND REACH MOUNTING HOLES IN BOTTOM OF PYLON

ORIGINAL OPTICAL SYSTEM ORIENTATION

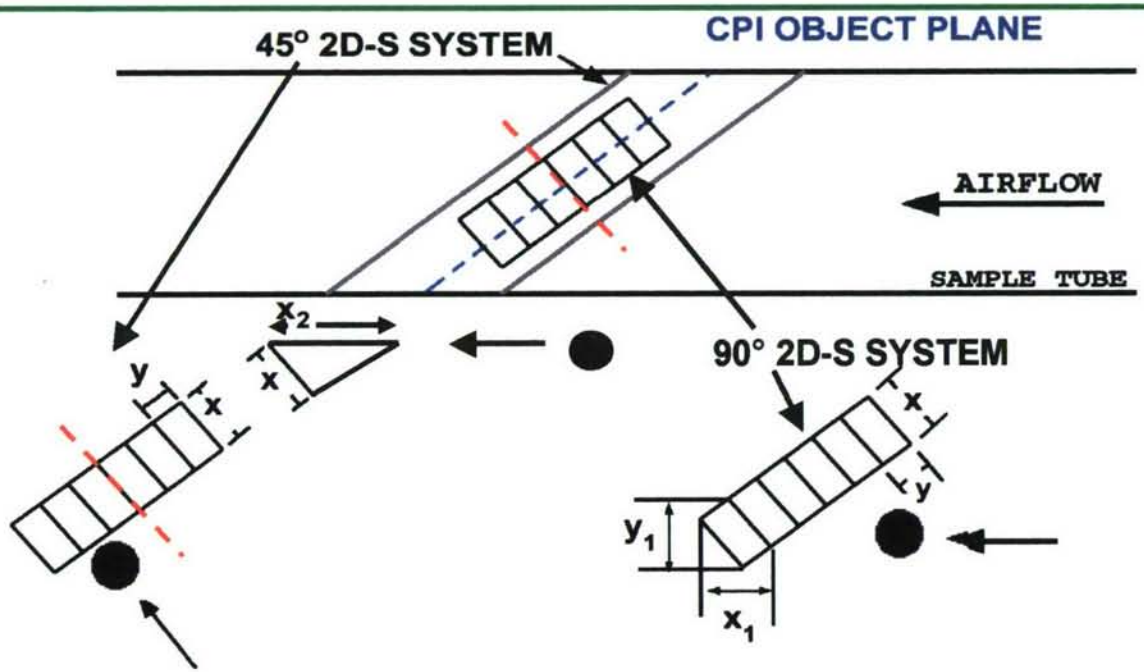

$$x_1 \neq x_2 \neq x$$

- PROPOSED BECAUSE ALL TRIGGERED IMAGES PERFECTLY IN FOCUS ON CPI, HOWEVER:
- PIXEL RESOLUTION DIFFERENT FOR 45 AND 90 SYSTEM
- TRUE AIR SPEED CLOCKING DIFFERENT FOR 45 AND 90 SYSTEM, WILL NOT HAVE SQUARE PIXELS
- DIFFICULT TO INTERPRET IMAGES / OUT OF FOCUS EFFECTS, 2D-S SOFTWARE IS NOT DIRECTLY APPLICABLE

NEW OPTICAL SYSTEM ORIENTATION

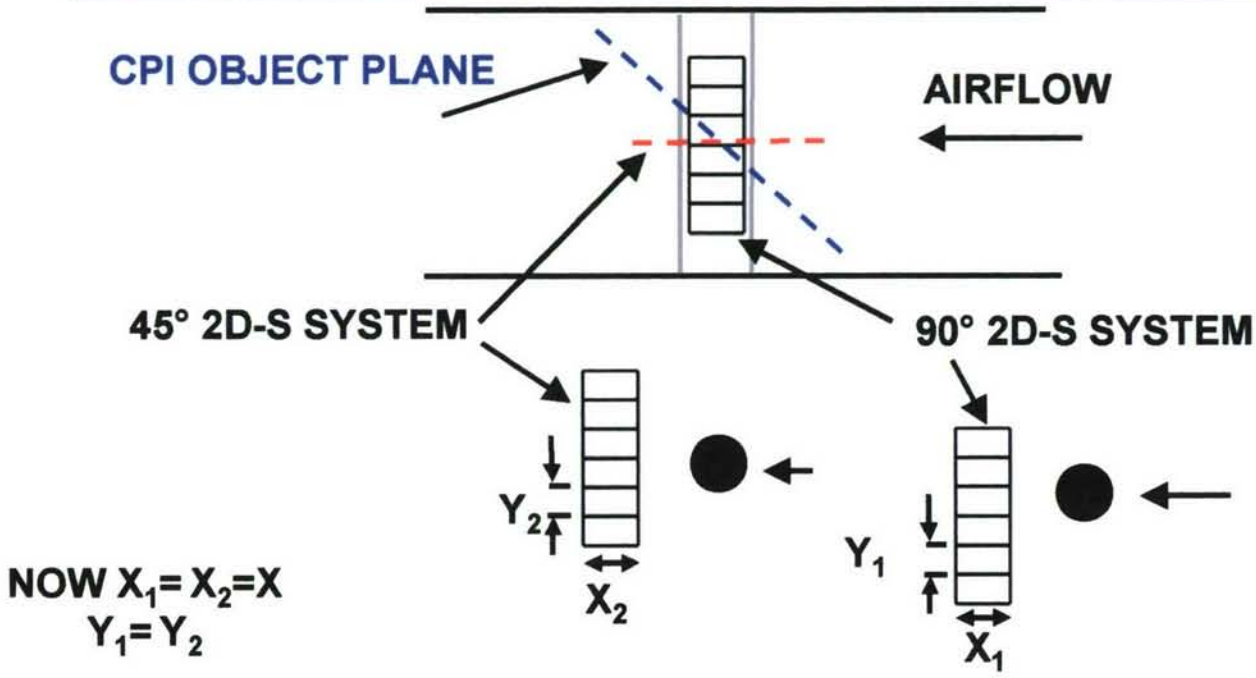

- PIXEL RESOLUTION SAME FOR 45 AND 90 SYSTEM
- TRUE AIR SPEED CLOCKING SET TO X1, WILL HAVE SQUARE PIXELS
- ALL 2D-S ANALYSIS SOFTWARE IS DIRECTLY APPLICABLE, FUTURE SOFTWARE ALSO APPLICABLE TO 2D-S AND 3V-CPI
- INCREASE IN 2D-S SAMPLE VOLUME
- TRIGGERED IMAGES NOT PERFECTLY IN FOCUS ON CPI

NEW ORIENTATION EFFECT ON CPI IMAGE FOCUS

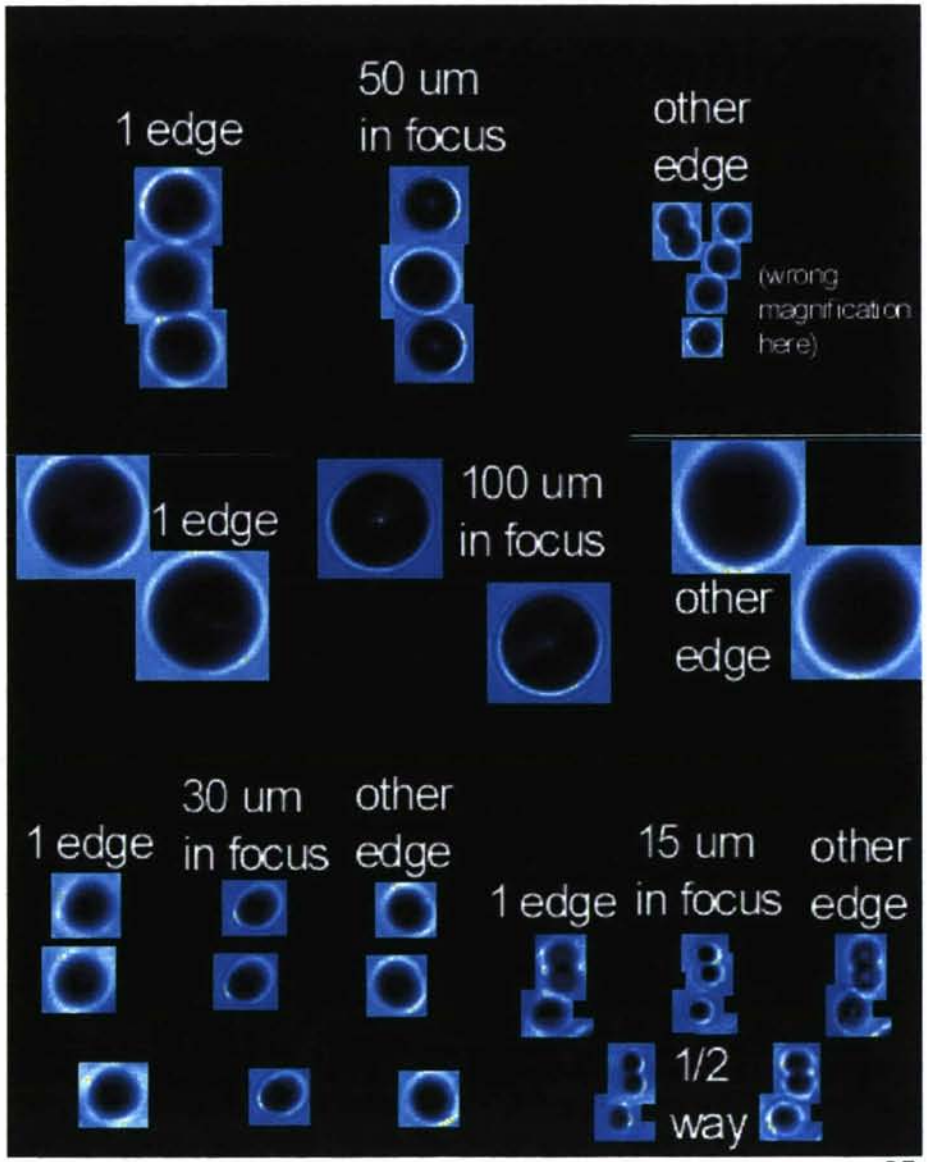

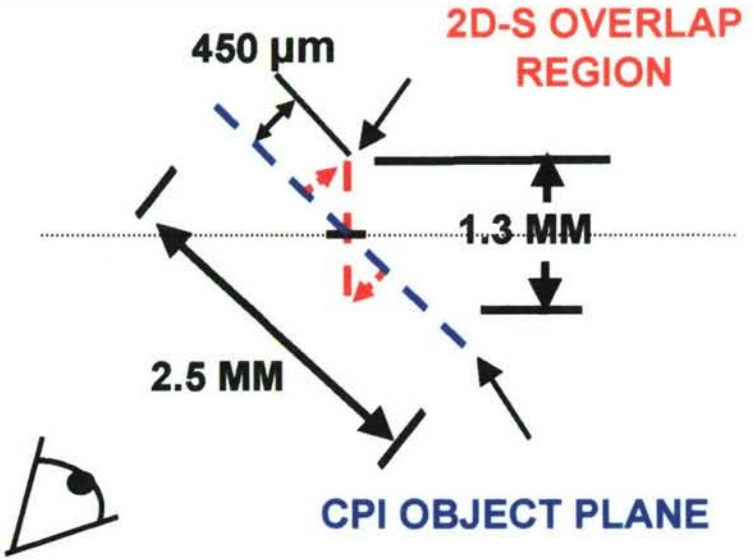

- **15 µm ~ SMALLEST PARTICLE THAT WILL BE DETECTED AT EDGES OF 2D-S OVERLAP**
- **PARTICLES ~ 450 µm FROM CPI OBJECT PLANE AT SV EDGES**
- **OUT OF FOCUS IMAGES OF 15 µm BEADS FAIRLY GOOD AT SV EDGE**
- **SIZE CAN BE CORRECTED BASED ON 2DS ARRAY POSITION AND CMOS GRAY SCALE LEVEL**

DESIGN CHALLENGES FOR COMBINED 3V-CPI OPTICAL SYSTEM

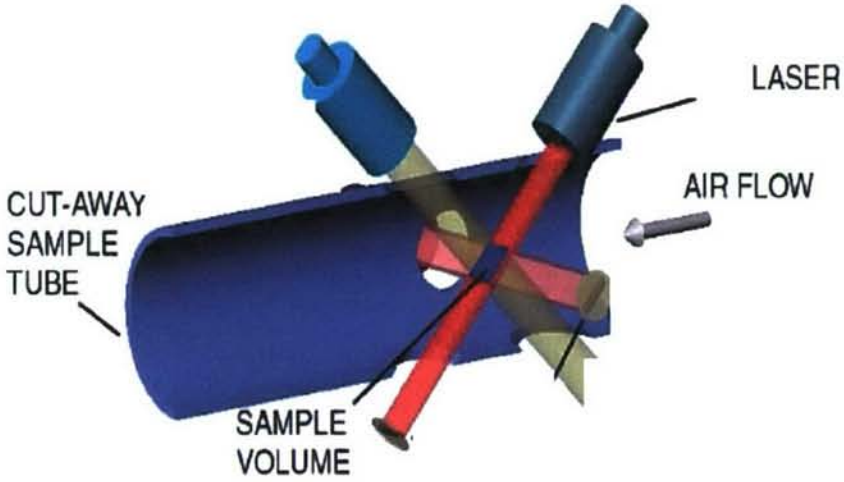

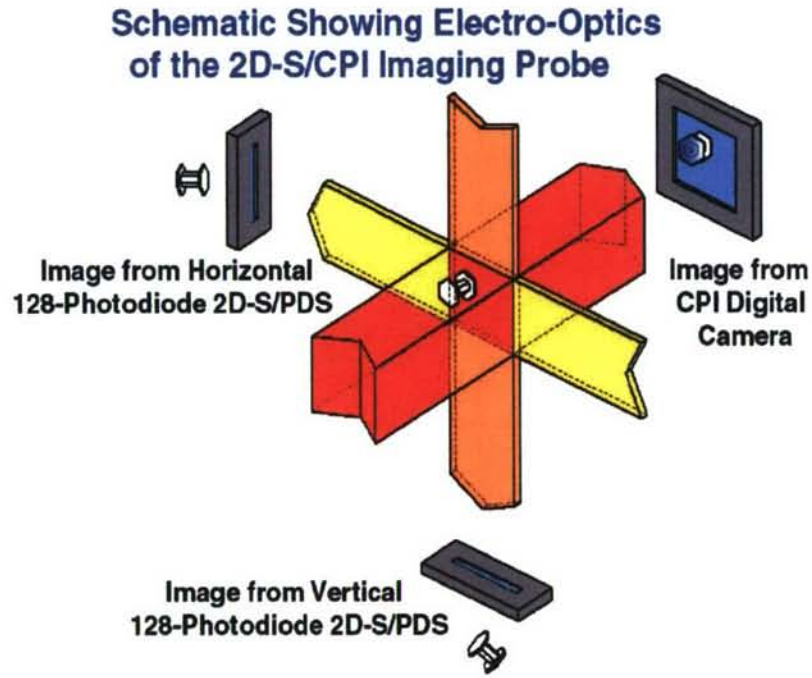

- EXISTING CPI IMAGING SYSTEM USED IN 1" DIAMETER SAMPLE TUBE – NEW DESIGN TARGETING 2" TUBE
- 2D-S SYSTEM NOW TILTED 45 DEG. TO FLOW- NOW IT IS TILTED BACK PERPENDICULAR TO FLOW
- 45 2D-S MAY REQUIRE CORRECTION PLATE TO BALANCE OUT ASTIGMATISM – NO ASTIGMATISM NOW
- 2D-S LASER POWER IS BARELY SUFFICIENT IN CURRENT DESIGN – BEAM SHAPING MAY IMPROVE THIS
- LARGER DIAMETER SAMPLE TUBE MAY REQUIRE LARGER CLEAR APERTURE, POSSIBLY THICKER SAPPHIRE WINDOW DUE TO PRESSURE DIFFERENTIAL
- INCORPORATING FOLDED 2DS PATH INTO NEW GEOMETRY – 2D-S ARRAY BOARD HAS ARRAY ROTATED 45
- OPTICAL ALIGNMENT, - COPLANARITY OF 2D-S OBJECT PLANES WITH CCD OBJECT PLANE NOT CRITICAL

2D-S OPTICAL SYSTEM PARAMETERS

- BEAM SHAPING (ILLUMINATION) SYSTEM – LASER AND OPTICS USED TO ILLUMINATE ARRAY (PRESENTED 2 OPTIONS LAST TIME)
- IMAGING OPTICAL SYSTEM – TAKES OBJECT IN SAMPLE VOLUME AND FORMS IMAGE ON ARRAY AT REQUIRED MAGNIFICATION
- USED TO TRIGGER CPI IMAGING SYSTEM, OVERLAP OF 45 AND 90 IMAGING SYSTEMS IN SAMPLE AREA IS CRITICAL DESIGN PARAMETER
- EXCESSIVE INSTABILITY OF ARRAY ILLUMINATION DEGRADES SNR, CAN LEAD TO EXCESS NOISE IN DATA, AFFECTS EACH CHANNEL INDIVIDUALLY
- EXCESSIVE INSTABILITY OF 2D-S IMAGING OPTICAL SYSTEMS LEADS TO TRIGGERING PROBLEMS, DESIRABLE TO HAVE 0-10 MICRON SEPARATION BETWEEN OBJECT PLANES
- TRIGGERING ELECTRONICS DESIGNED TO COMPENSATE FOR SOME THERMAL SHIFT IN 45 AND 90 OBJECT PLANES

2D-S IMAGING OPTICAL SYSTEM, EXISTING VS PROPOSED VS NEWLY PROPOSED 4 LENS SYSTEM

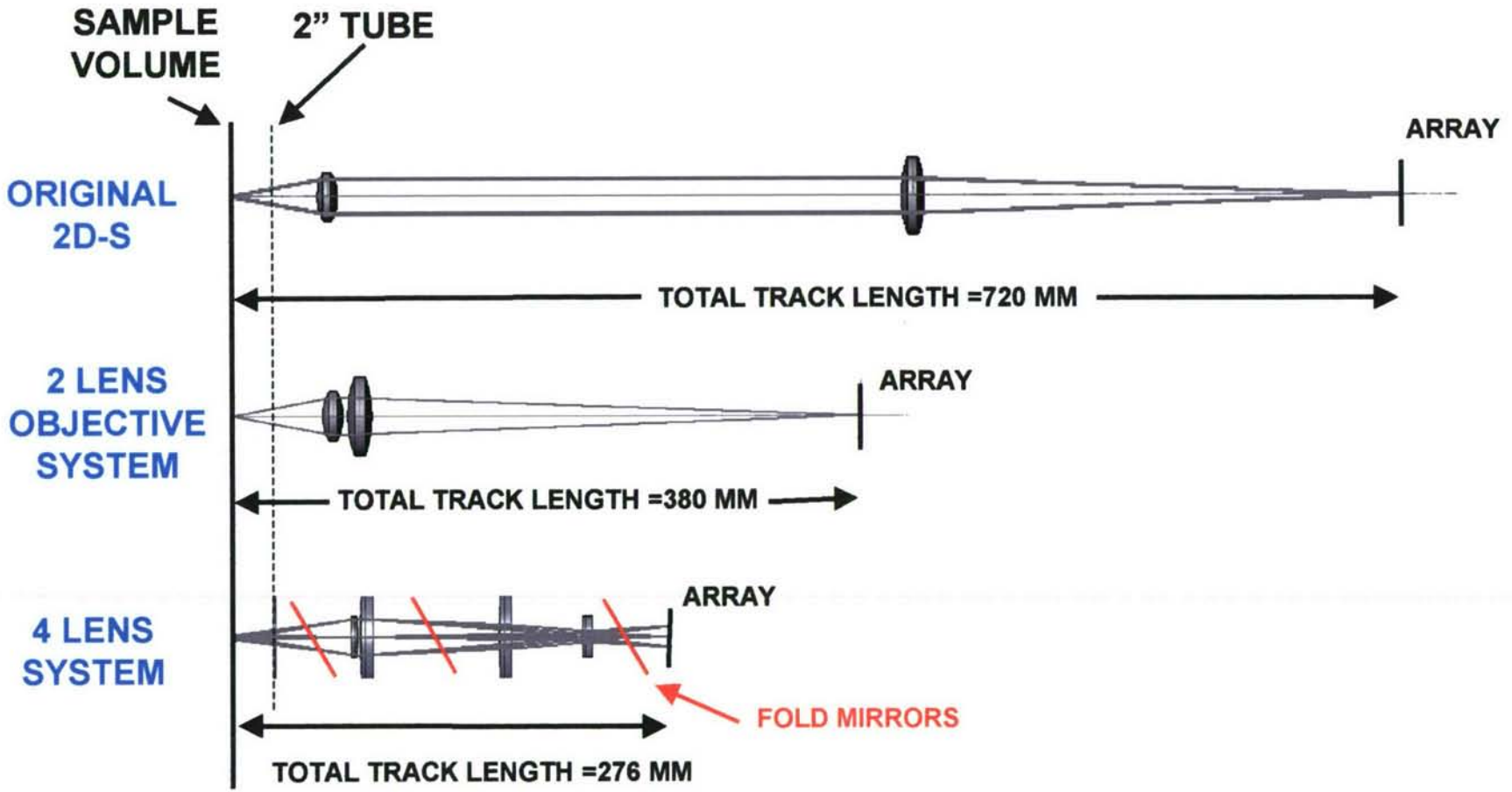

NEWLY PROPOSED 2D-S 4 LENS SYSTEM

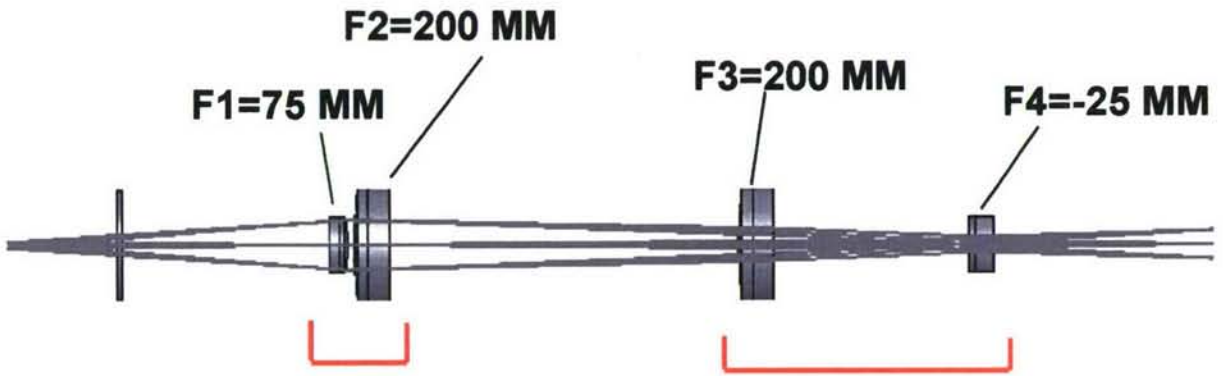

$M_{SYSTEM}=M_A M_B=5X$

GIVES 10 UM/PIXEL RESOLUTION IN SAMPLE VOLUME

USED TO INCREASE MAGNIFICATION OF SYSTEM WITHOUT INCREASING BACK FOCAL LENGTH

80 MICRON BEAD - DOF PLOT FOR 4 LENS SYSTEM

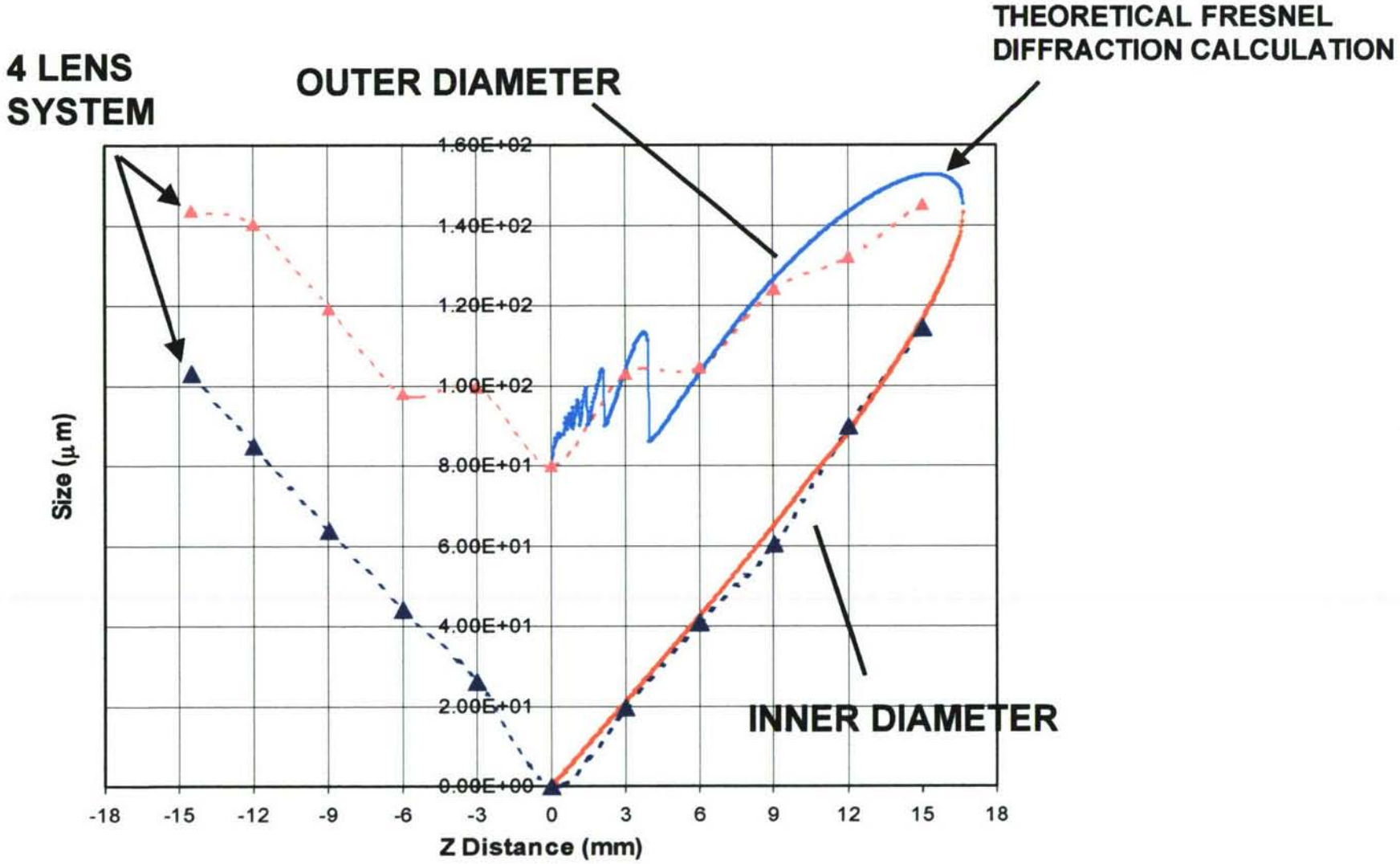

3V-CPI OPTO-MECHANICAL/PACKAGING CONCERNS

- GOAL: RELIABLE / REPEATABLE PARTICLE SIZE AND CONCENTRATION MEASUREMENT AND CPI SYSTEM TRIGGERING / IMAGING
- MININIZE EFFECTS OF TEMPERATURE, VIBRATION (OTHER ENVIRONMENTAL FACTORS) ON INSTRUMENT PERFORMANCE
- DESIGN A SYSTEM THAT CAN BE EASILY MANUFACTURED, ALIGNED, EVALUATED, AND QUANTIFIED IN THE LABORATORY
- SHORTER OPTICAL PATHS ARE INHERENTLY LESS SENSITIVE TO VIBRATION AND THERMAL EFFECTS THAN LONGER OPTICAL PATHS – DESIGN FOR UNIFORM THERMAL EXPANSION
- BASED ON PAST EXPERIENCE, ALL ADJUSTMENTS SHOULD BE ORTHOGONAL TO 2D-S LINEAR ARRAY POSITION WITH NO CROSS-TALK

ZEMAX LAYOUT – SINGLE VS DUAL FOLD SYSTEM

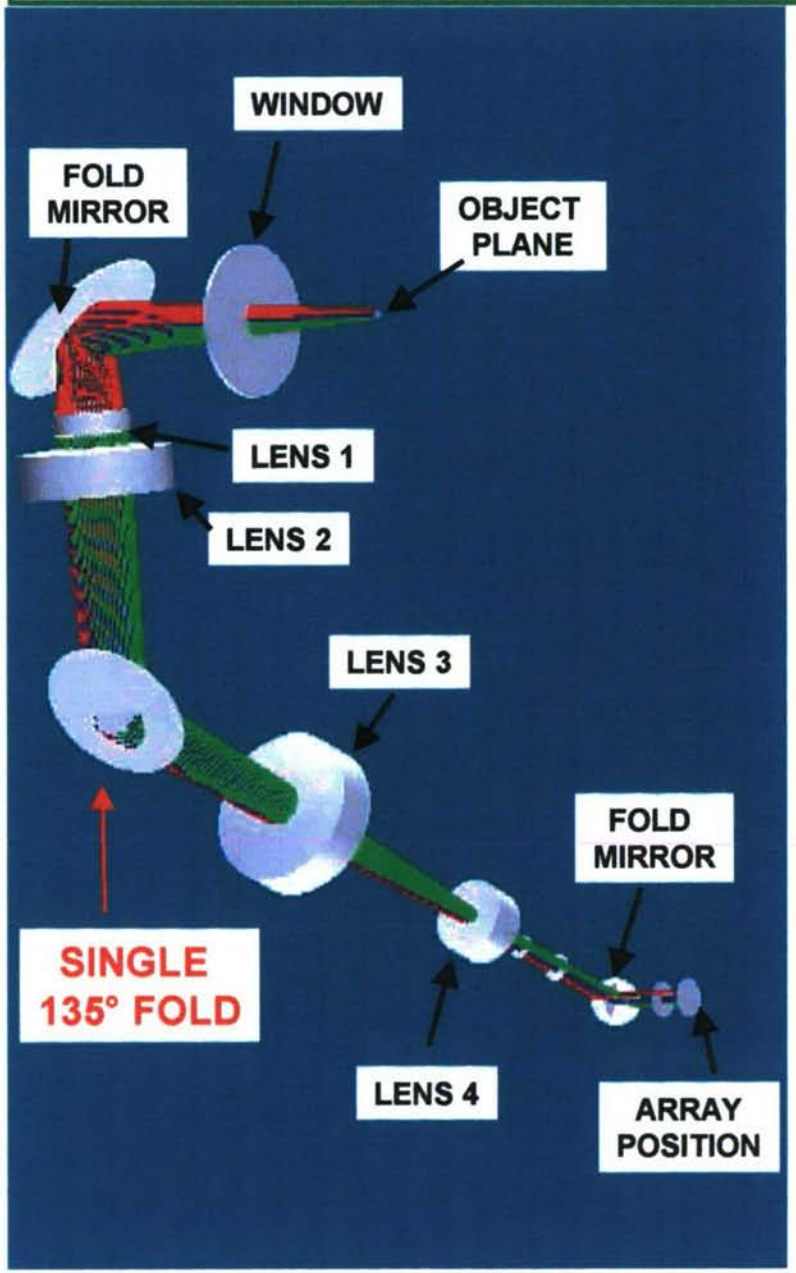

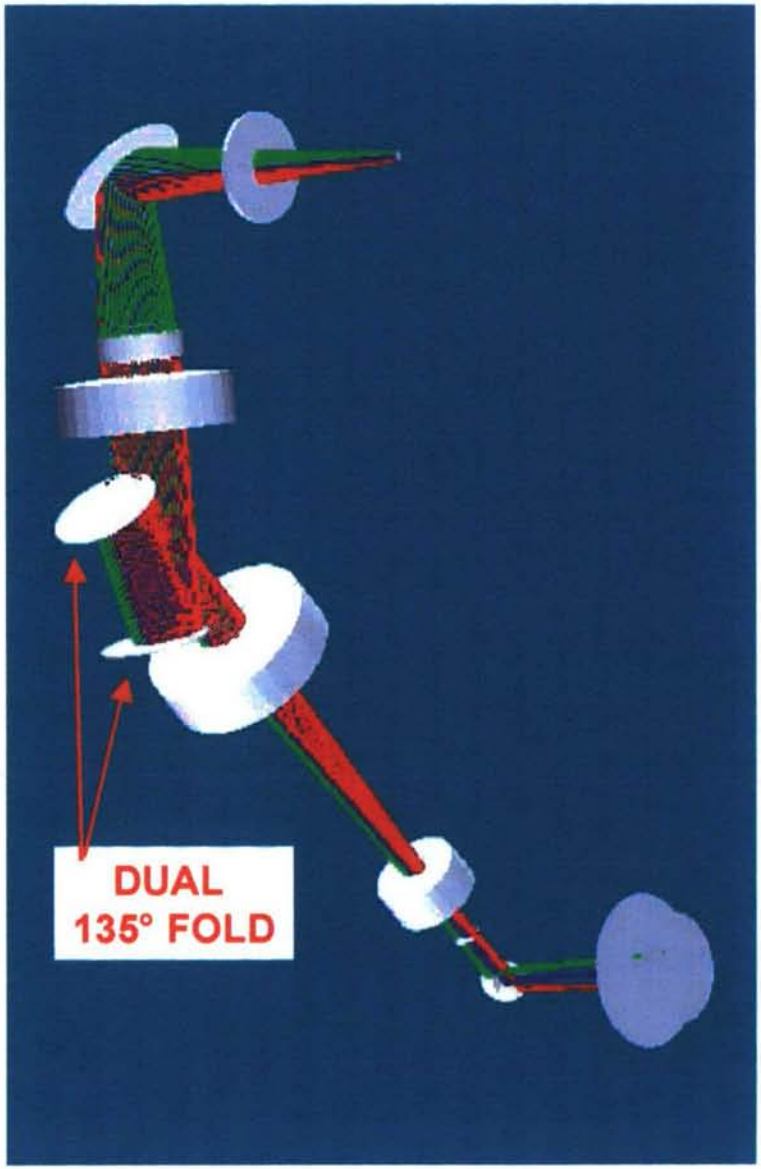

COMPARISON OF SINGLE VS DUAL FOLD MIRROR APPROACH

SINGLE FOLD MIRROR, 67.5° AOI

- CONCEPTUALLY SIMPLE, ONE COMPONENT
- POTENTIAL POLARIZATION ISSUES WITH COATING ABOVE 45° AOI
- SMALL MIRROR DISPLACEMENT OR TILT RESULTS IN LARGE REFLECTED BEAM OFFSET OR TILT, LARGE EFFECT ON ARRAY OFFSETS
- INITIAL ALIGNMENT POSITION WILL REQUIRE EXTREMELY HIGH RESOLUTION

DUAL FOLD MIRROR, 11.25° AOI

- 2 COMPONENTS, MORE COMPLICATED, BUT MORE COMPACT
- NO POLARIZATION ISSUES WITH COATINGS
- DISPLACEMENTS AND TILTS HAVE MUCH LESS EFFECT ON BEAM, FOR UNIFORM THERMAL EXPANSION, INPUT AND OUTPUT BEAM ARE NOT DISPLACED
- MOUNT CAN BE MACHINED TO HIGH TOLERANCE TO HOLD MIRRORS IN CORRECT POSITION
- POTENTIAL LASER BEAM CLIPPING AND VIGNETTING OF OBJECT IF NOT DESIGNED CORRECTLY

DUAL FOLD VS SINGLE FOLD

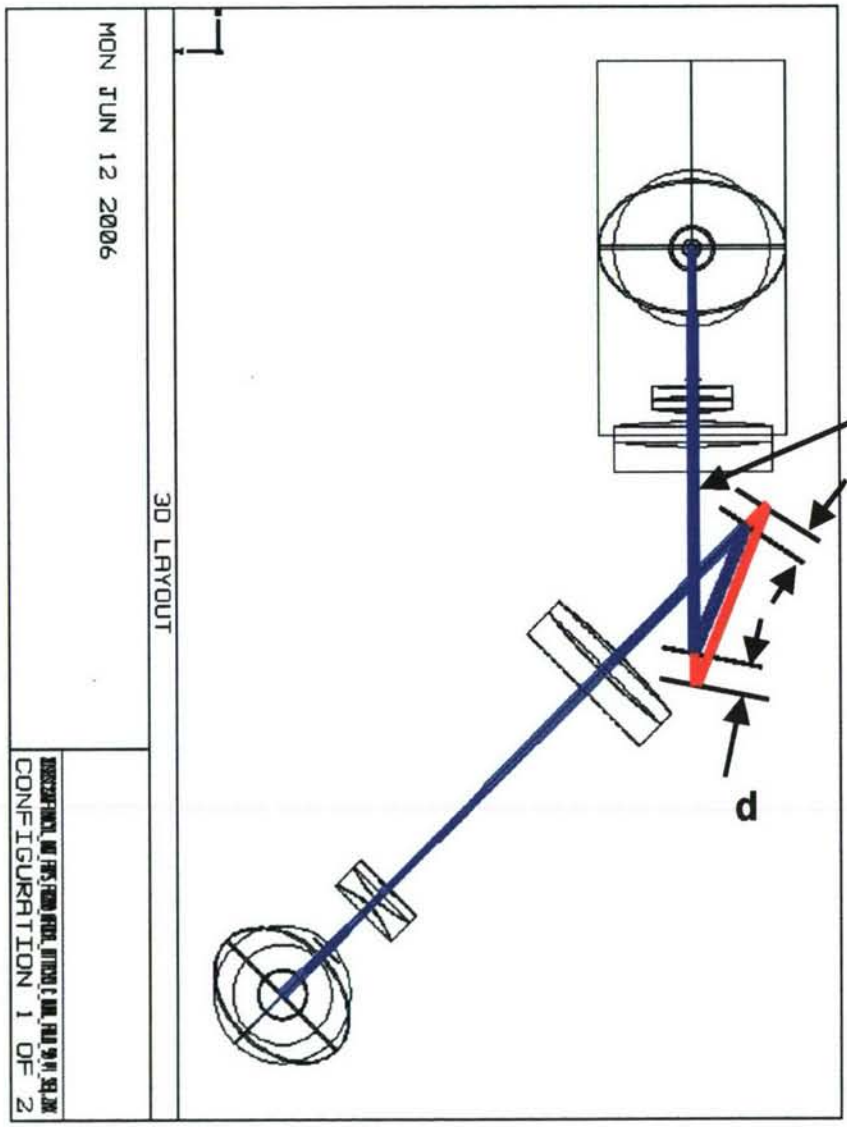

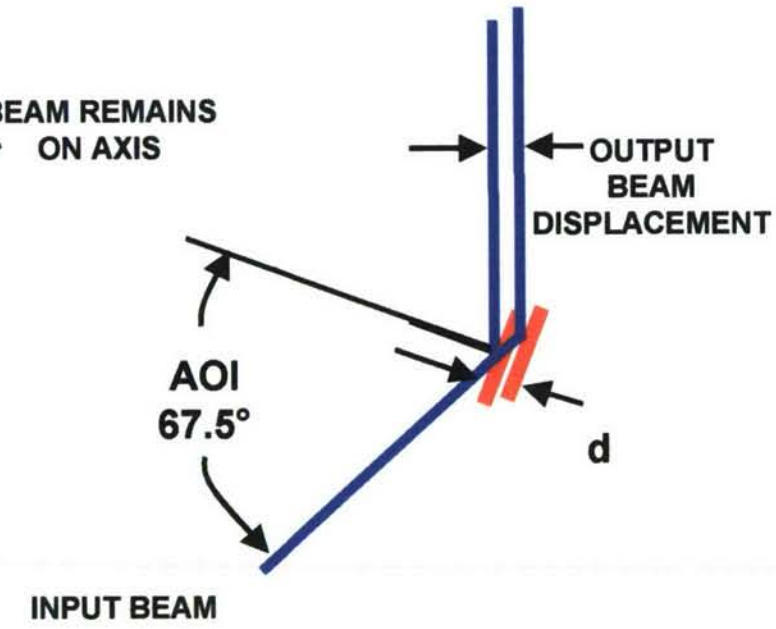

SINGLE FOLD MIRROR AT LARGE AOI CAN RESULT IN LARGE SHIFTS OF 90 AND 45 W.R.T EACH OTHER

DUAL FOLD 4 LENS SYSTEM PROTOTYPED IN LAB

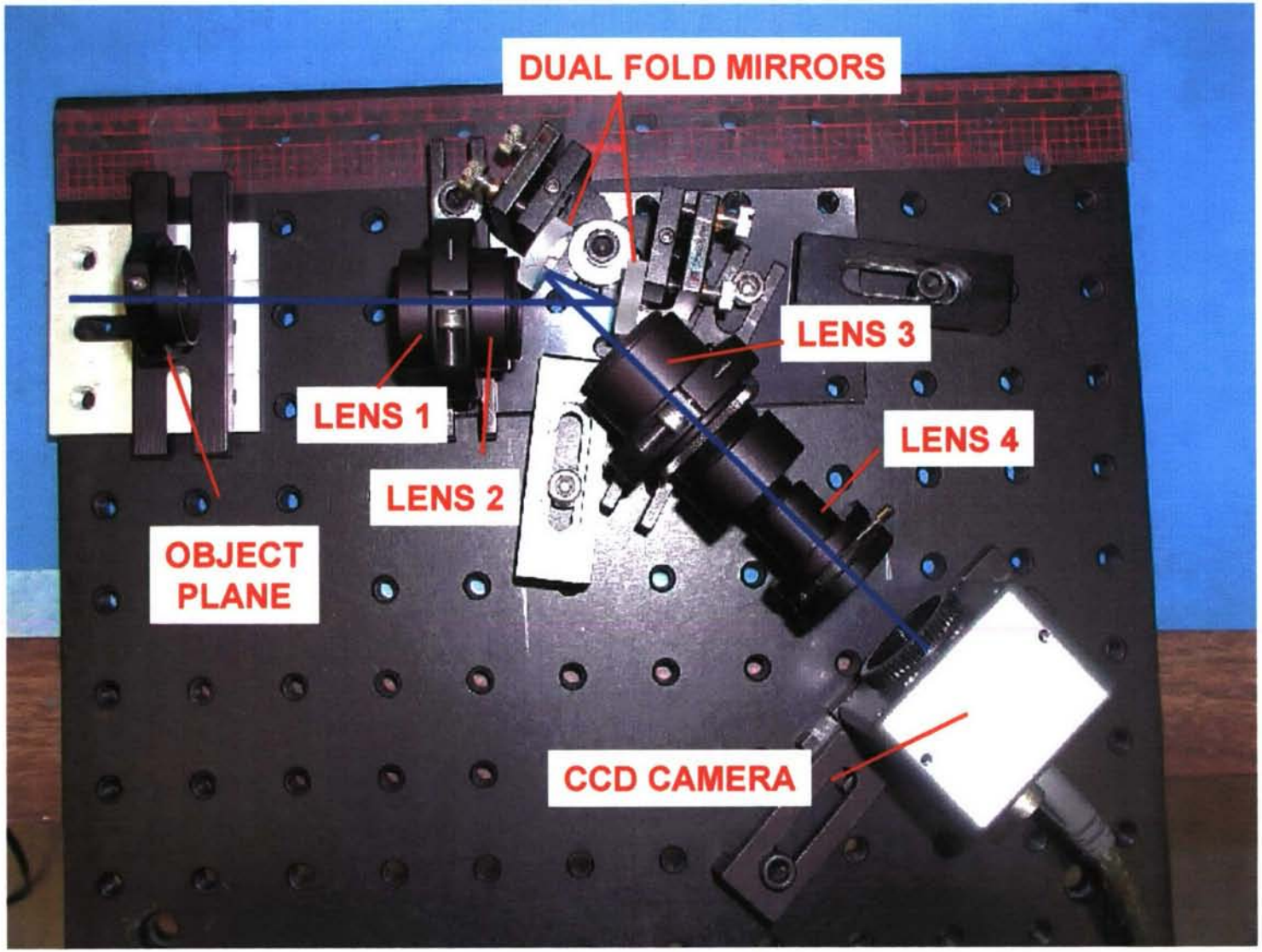

ZEMAX LAYOUT – COMBINED 45 & 90 SYSTEM

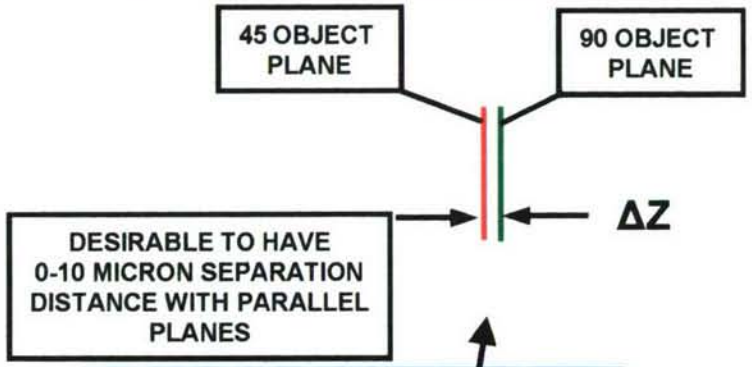

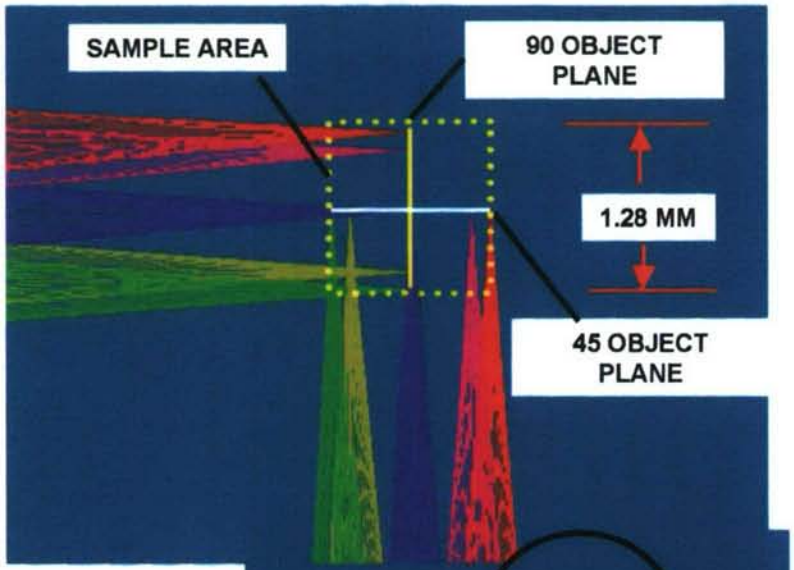

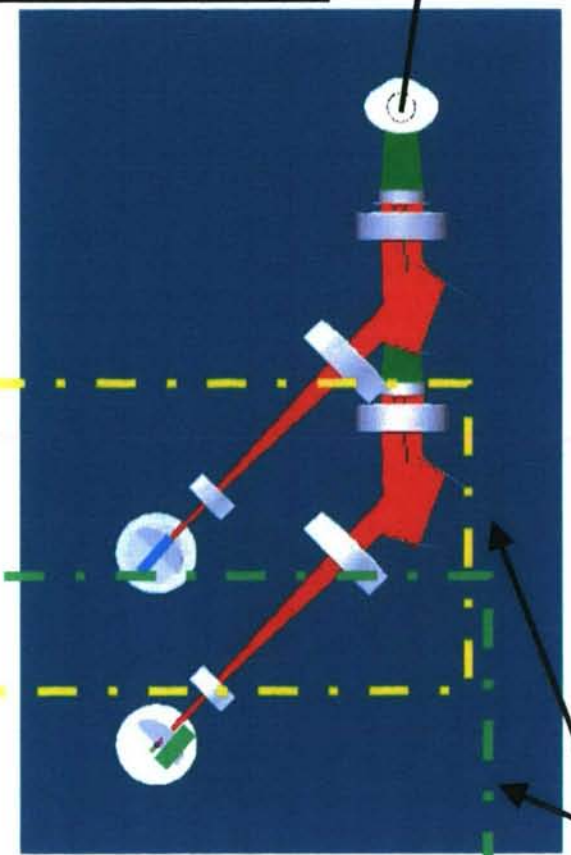

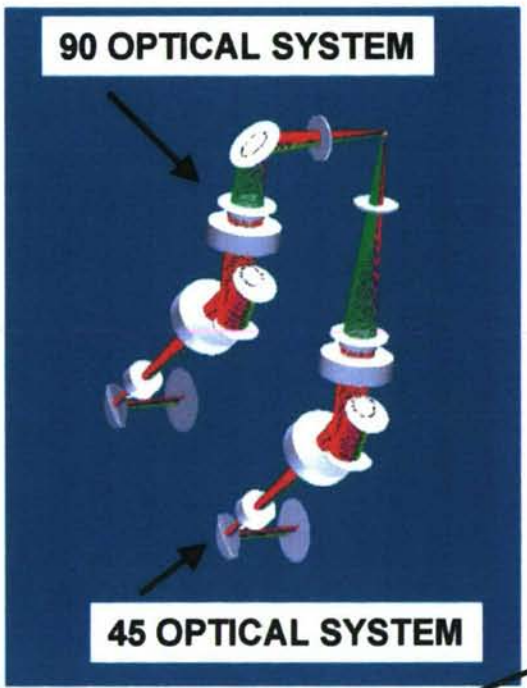

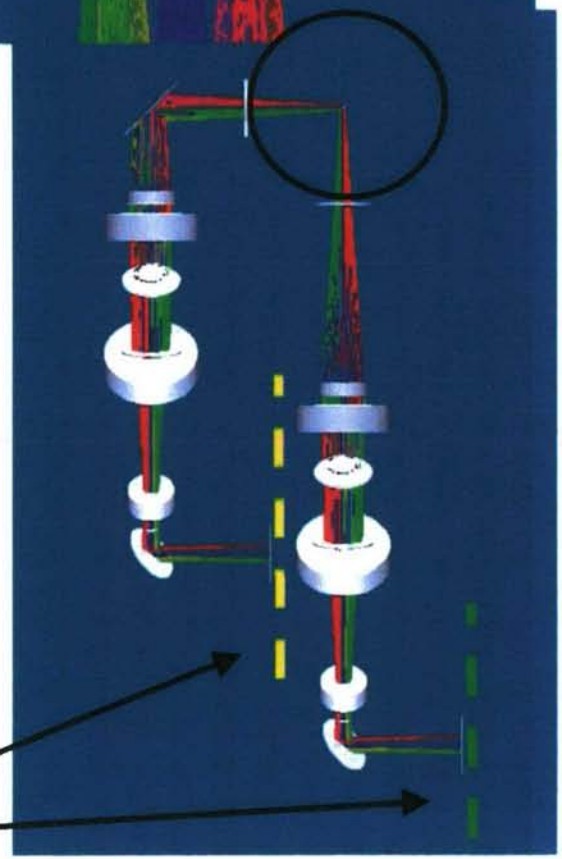

ARRAY BOARDS

3V-CPI 90° 2D-S SYSTEM ASSEMBLY LAYOUT (45° ALMOST IDENTICAL)

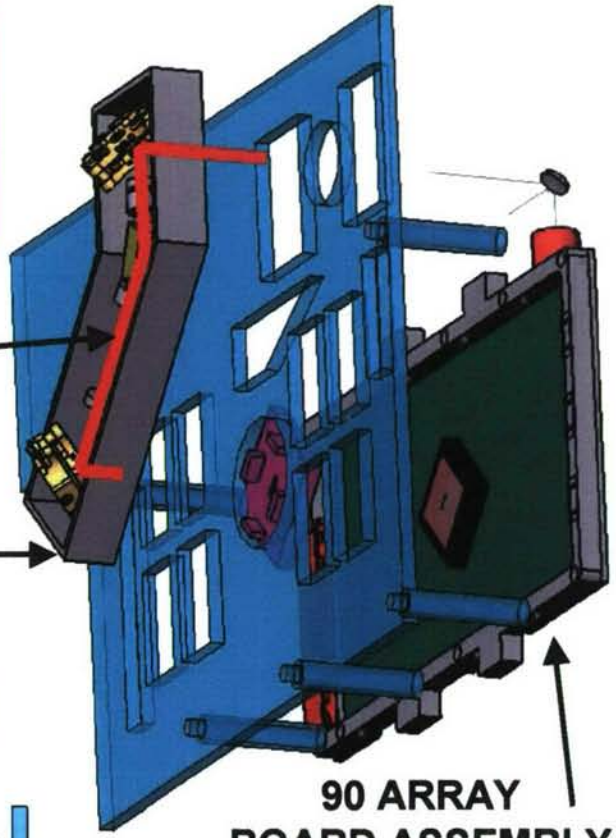

90 OPTICAL AXIS

90 4 LENS SYSTEM
INDEPENDENTLY ALIGNED

90 ARRAY
BOARD ASSEMBLY

90 PLATEN

- STRUCTURAL INTERFACE BETWEEN ARRAY ASSEMBLY AND 90 OPTICAL SYSTEM
- CONNECTS TO 45 OPTICAL SYSTEM TO FORM RIGID STRUCTURE

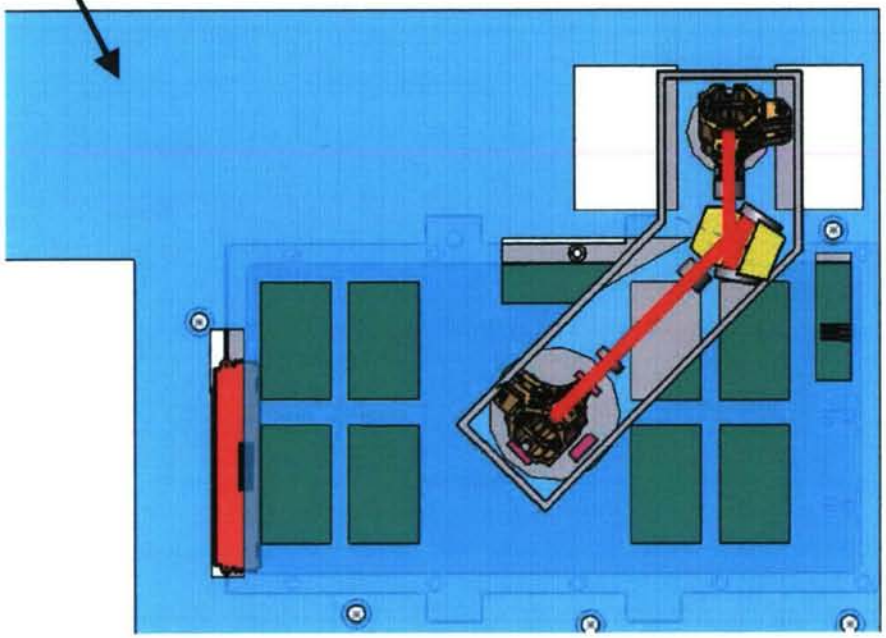

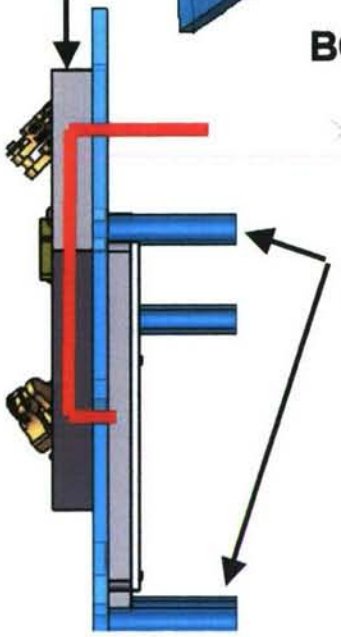

STRUCTURAL
CONNECTING
MEMBERS TO 45
PLATEN

3V-CPI COMBINED OPTICAL PATHS

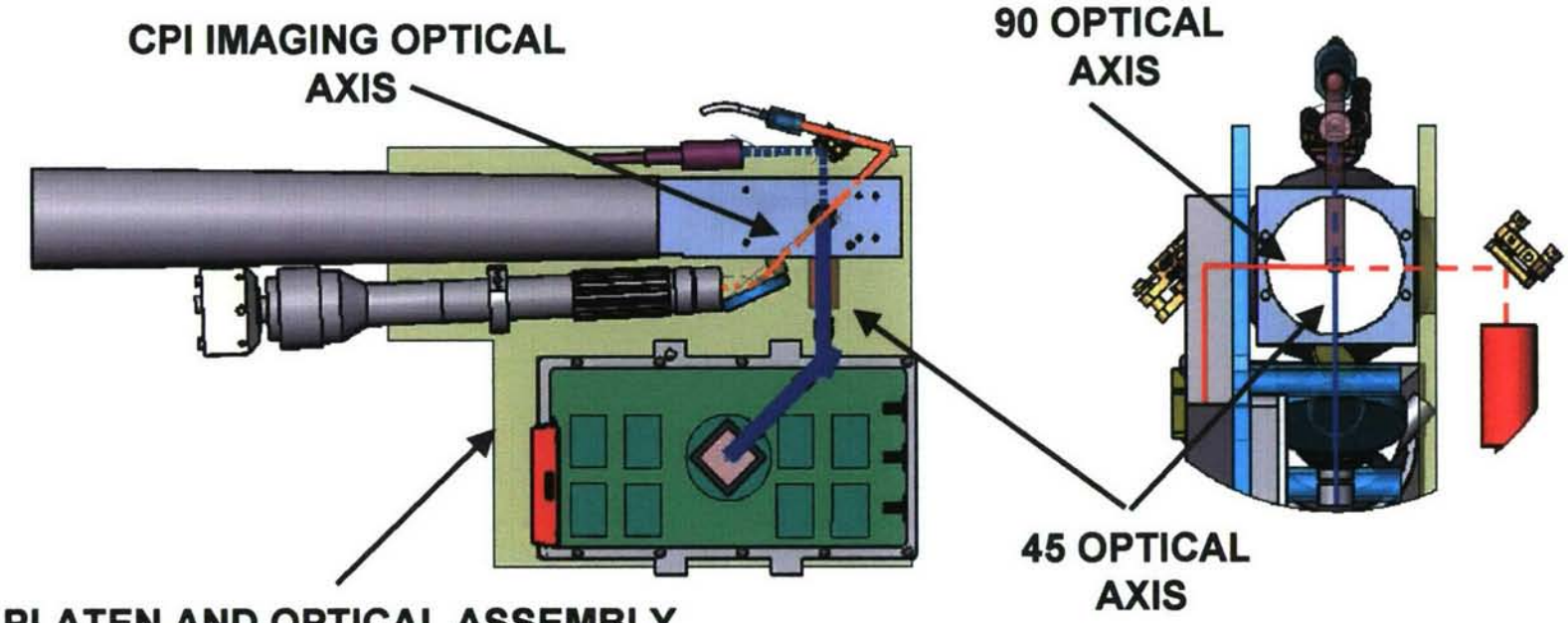

45 PLATEN AND OPTICAL ASSEMBLY

- CONNECTS TO 90 OPTICAL SYSTEM TO FORM RIGID STRUCTURE

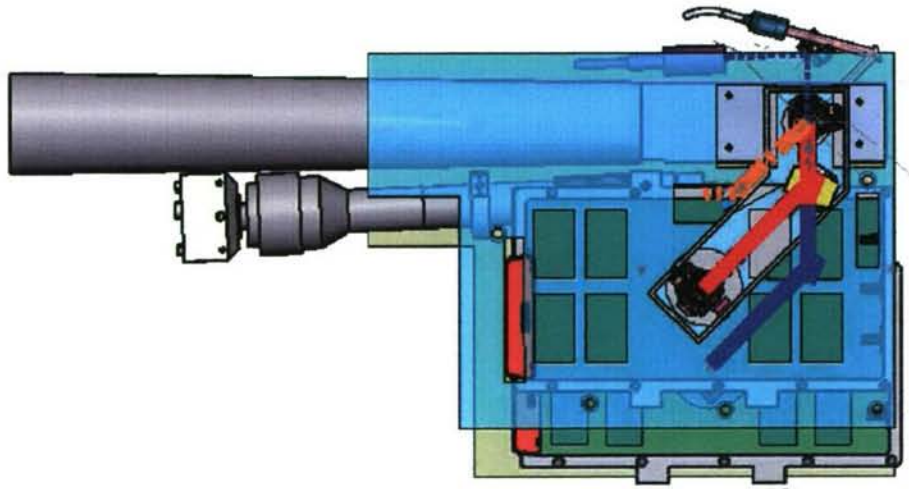

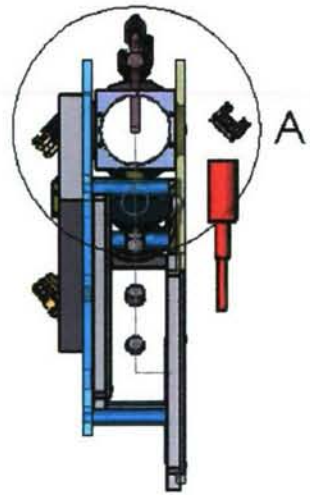

CPI IMAGE SYSTEM COMPARISON, M=5X

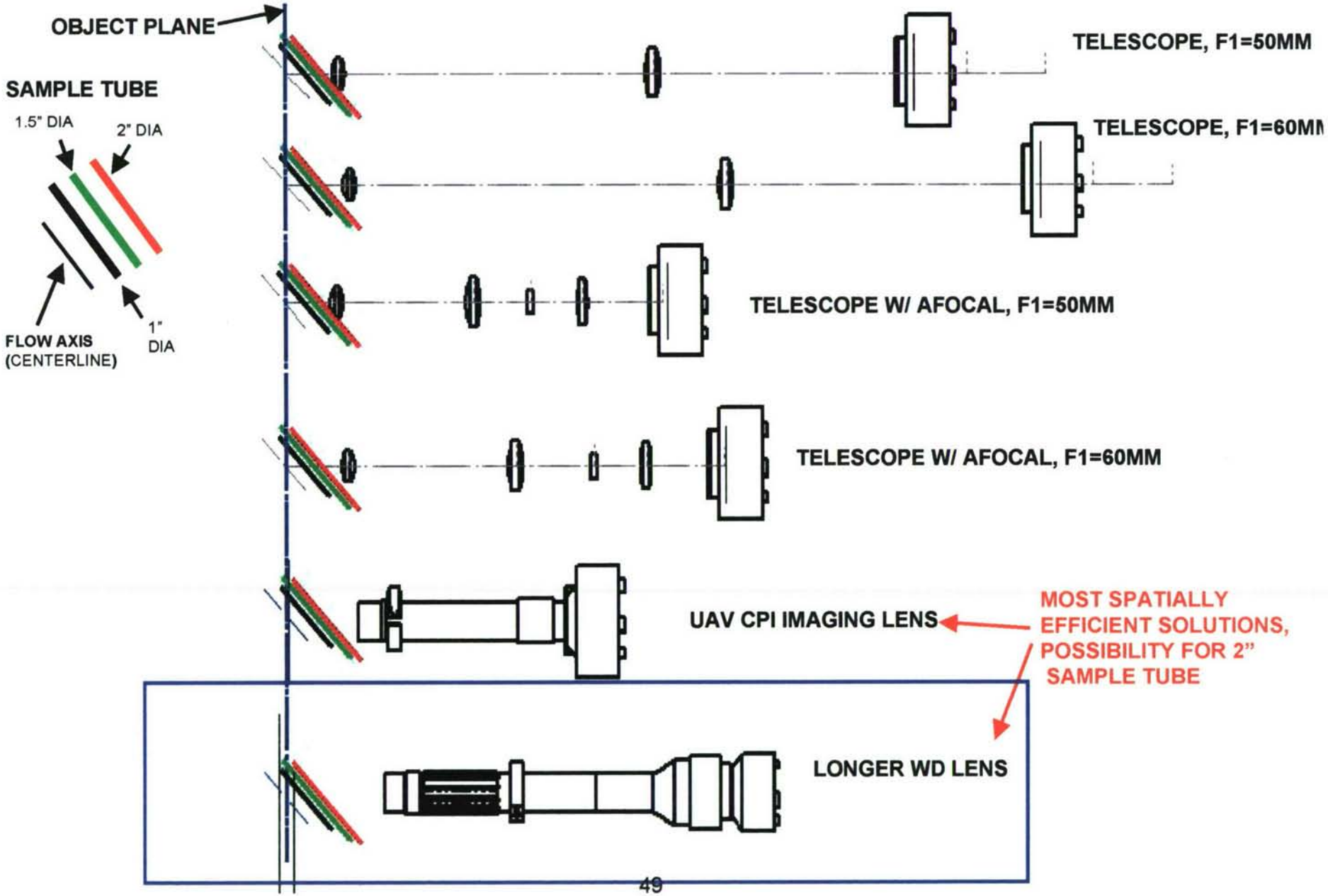

CPI IMAGE SYSTEM LAYOUT INCORPORATING 135 ° FOLD PATH

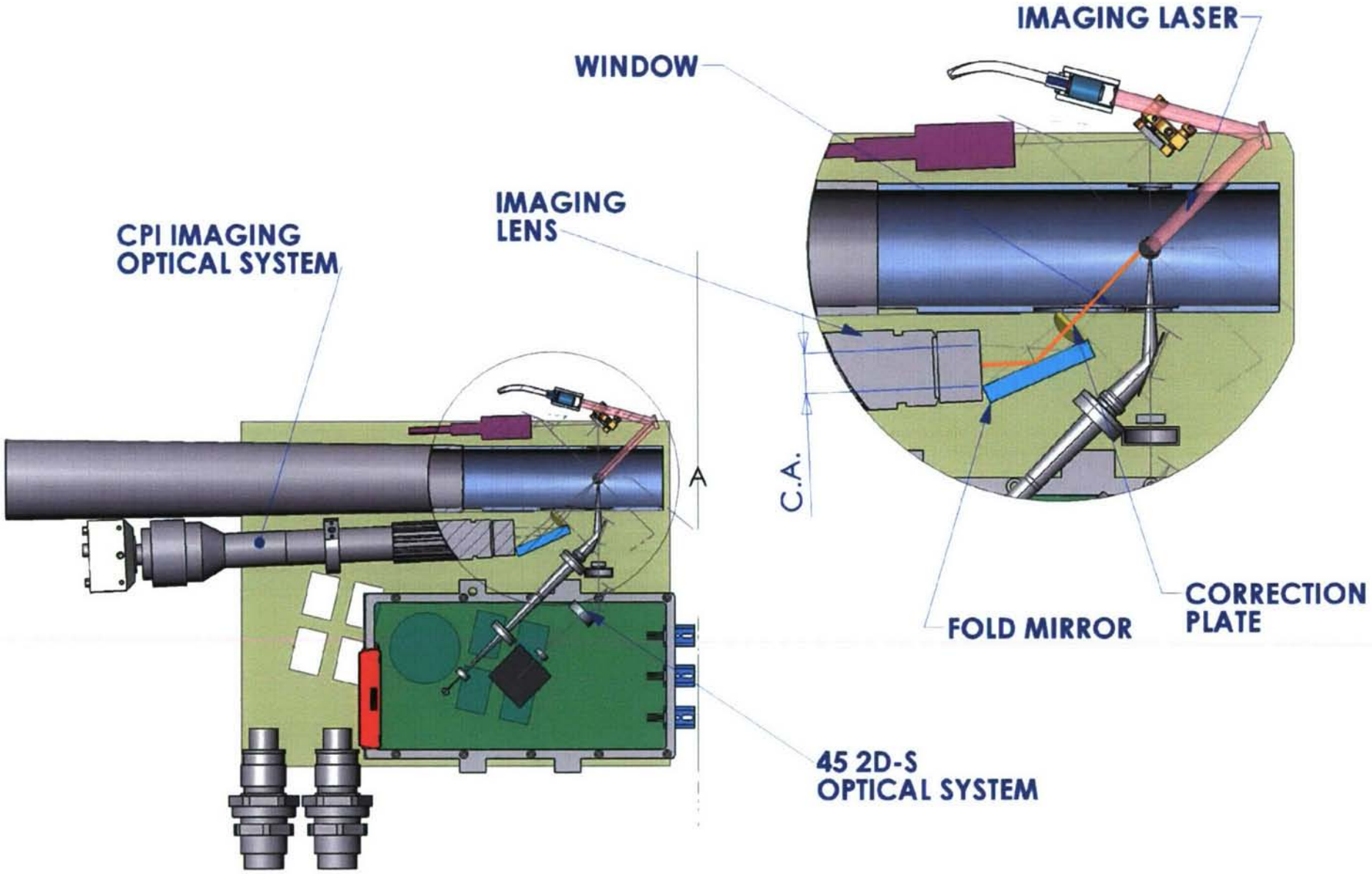

CPI IMAGING SYSTEM IN LABORTORY INCORPORATING 135° FOLD PATH

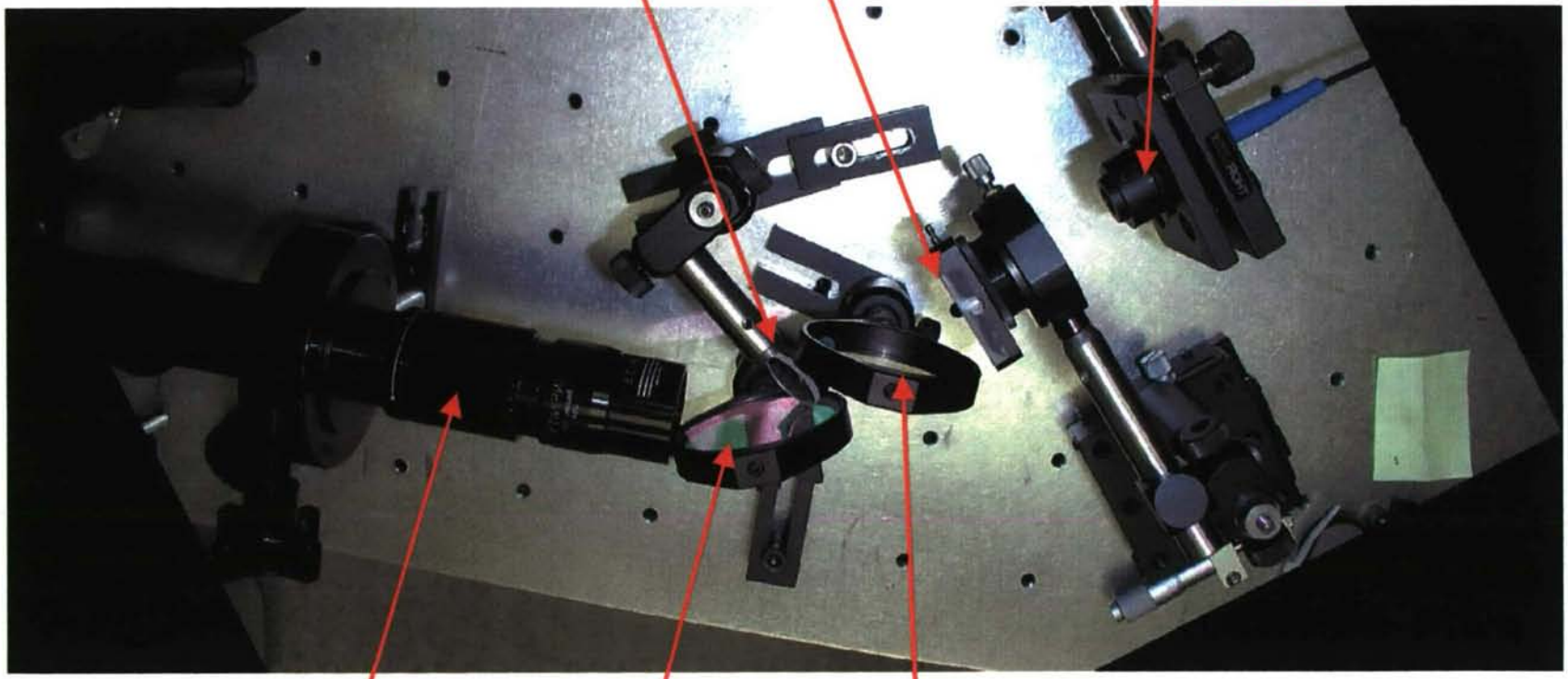

CPI IMAGING SYSTEM WINDOW PRESSURE INTEGRITY

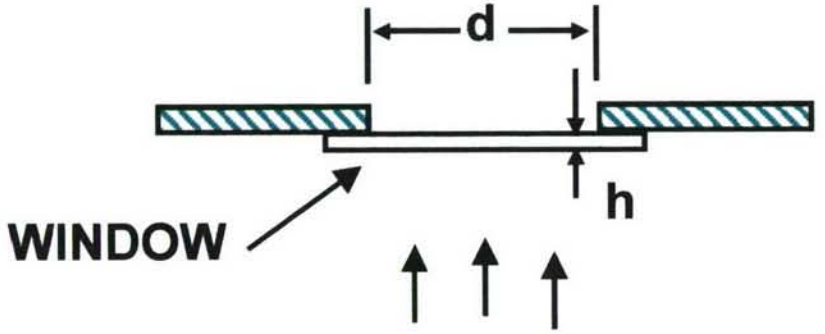

WINDOW FAILURE MAY OCCUR BELOW CRITICAL ASPECT RATIO

$$\text{CRITICAL ASPECT RATIO} = \frac{h}{d} = 1.06\left[\frac{P}{\sigma_{YS}}\right]^{1/2} = 0.024$$

- GV DESIGN PRESSURE – 26.2 PSI
- CALCULATION HAS SAFETY FACTOR OF 4X
- h=1 mm , d=22 mm (major axis of ellipse)
- σ_{YS}=50,000 psi FOR SAPPHIRE WINDOW

$h_{actual}/d_{actual} = 1/22$

$=0.045 > 0.024$

SUFFICIENT IMAGING WINDOW THICKNESS

OPTICAL SYSTEM ALIGNMENT PLAN

ALIGNMENT PLAN FORMULATED BEFORE DETAILED DESIGN TO INCLUDE ALIGNMENT FEATURES / ADJUSTMENTS IN DESIGN

NOTE: CPI SYSTEM CMOS CAMERA ALLOWS US TO LOOK AT STATIONARY IMAGES IN REAL TIME AT HIGH RESOLUTION, 2D-S SYSTEM ARRAY BOARDS MASK OUT STATIONARY OBJECTS, DIFFICULT TO ALIGN

- **The 45 and 90 optical systems will be aligned independently- using a white light source, target reticle, and CCD camera. Lens spacing, decentration, magnification, and focus will be checked.**
- **The two 2D-S imaging systems will be aligned w.r.t each other using stationary pin at the SV center, and CCD camera for each detector with array slit mask.**
- **2DS array board assemblies installed registered to position of slit mask.**
- **Individual laser beamshaping systems aligned with laser beam profiler, then installed into 3V-CPI. Tilt and translation of laser systems adjusted to illuminate array boards.**
- **Use moving wire on a speaker to evaluate and adjust array board positions.**
- **CPI imaging system will be aligned w.r.t the 2D-S system using stationary pin at the appropriate location and adjusting the imaging lens focus barrel and mirror tilt.**
- **System performance evaluated – with water drops, glass beads, moving wire.**

EXAMPLE OF 2D-S CO-PLANARITY EVALUATION

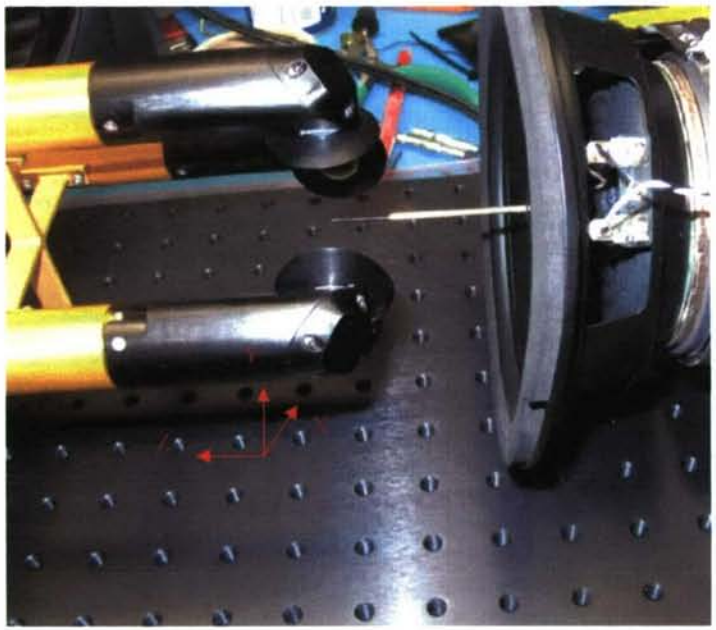

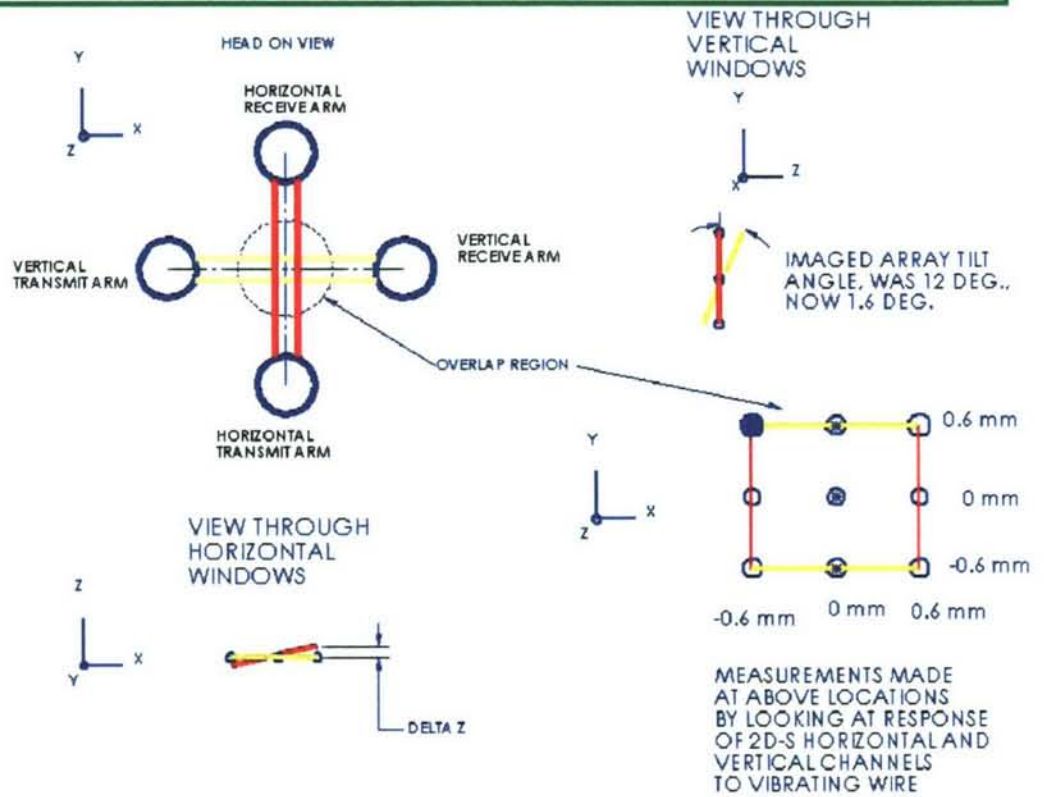

			X - Horizontal coordinate In overlap region	
		-0.6 mm	0 mm	0.6 mm
	-0.6 mm	Before Δz= 70 μm After Δz= 20 μm	Before Δz= -10 μm After Δz= 5μm	Before Δz= -90 μm After Δz= -15μm
Y - Vertical coordinate in overlap region	0 mm	Before Δz= 80 μm After Δz= 35μm	Before Δz= 20 μm After Δz= 10μm	Before Δz= -70 μm After Δz= -10μm
	0.6 mm	Before Δz= 120 μm After Δz= 25μm	Before Δz= 30 μm After Δz= 10μm	Before Δz= -30 μm After Δz= -10μm

EXAMPLE OF 2D-S LASER BEAM SHAPING ALIGNMENT WITH BEAM PROFILER

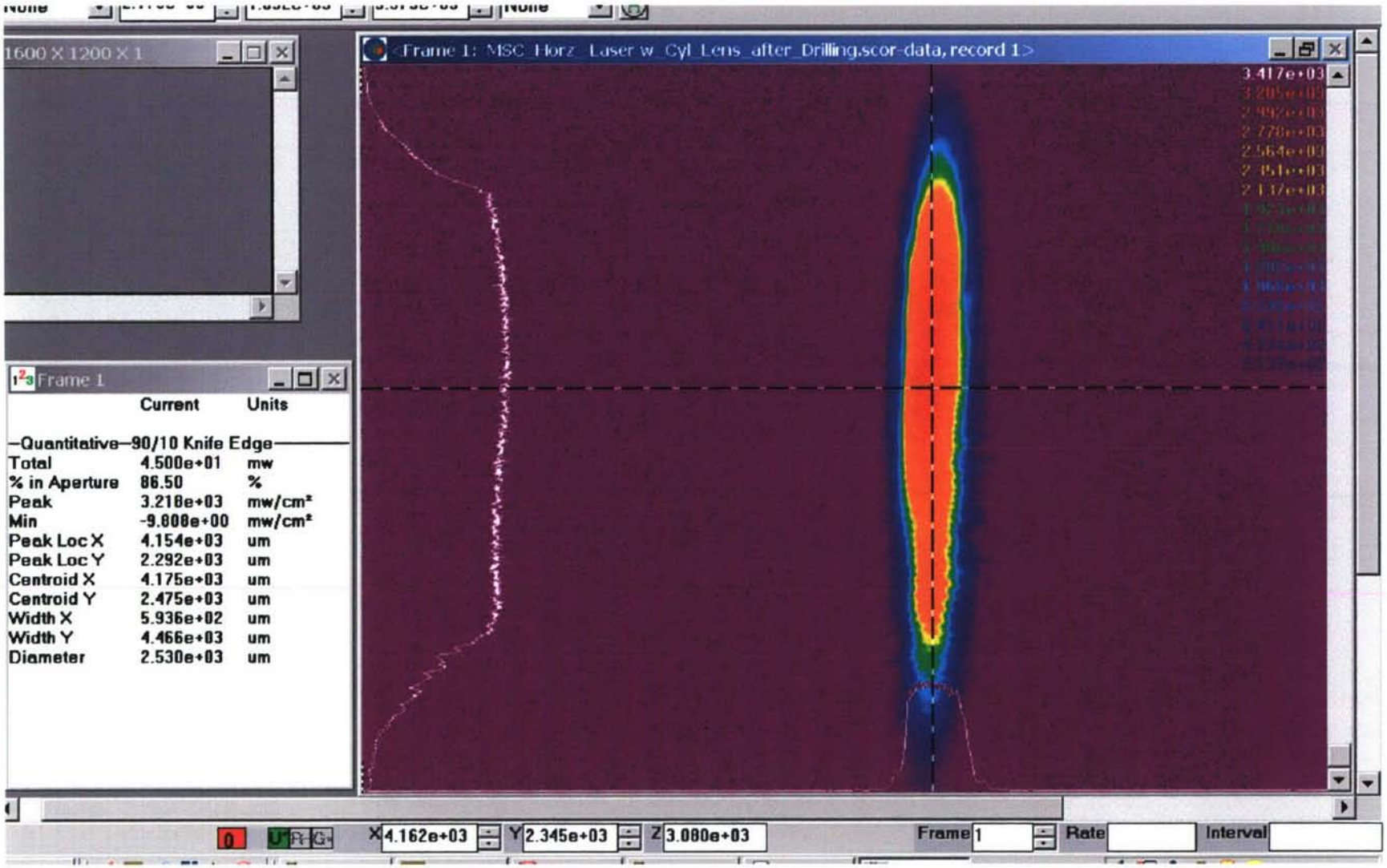

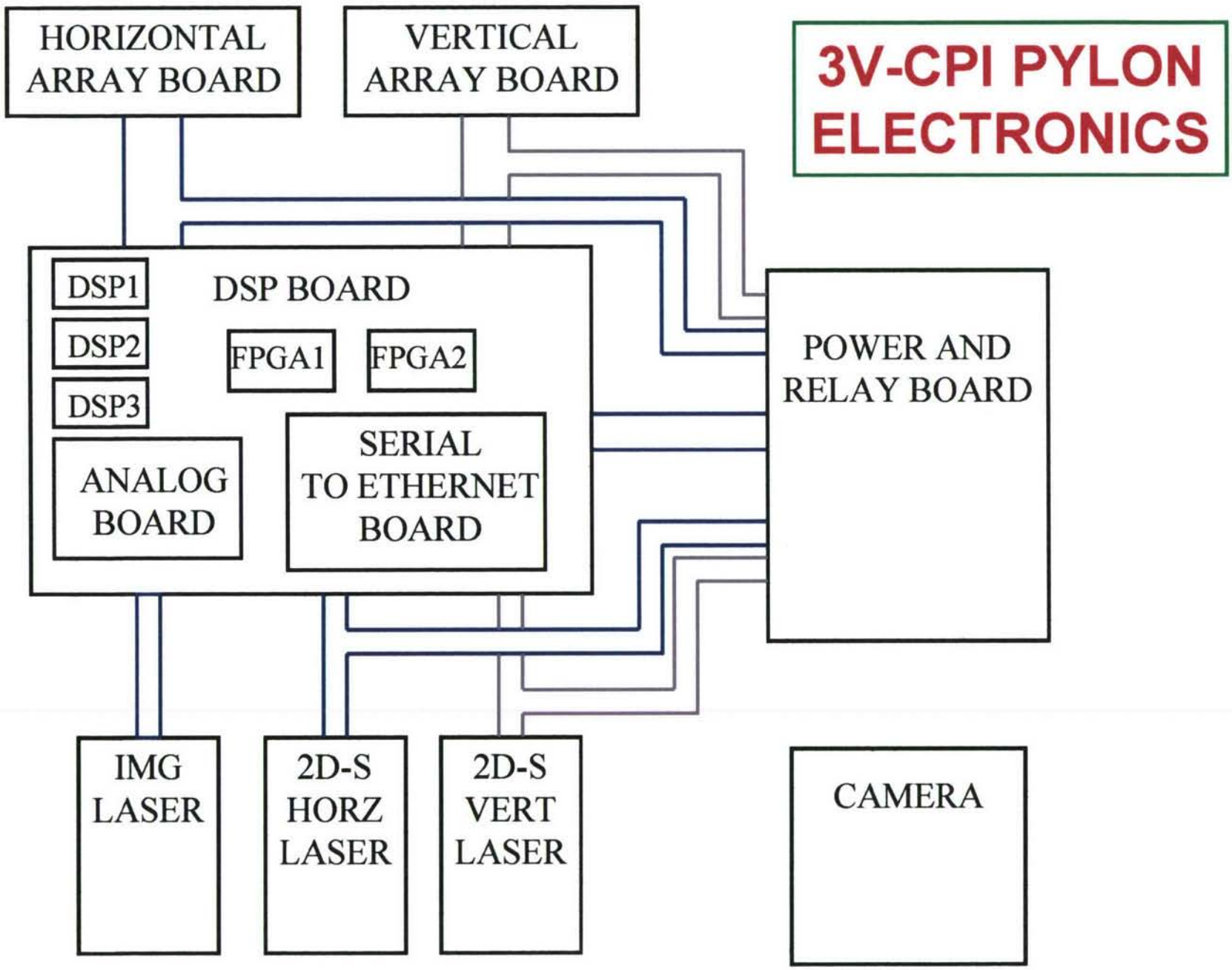
HORIZONTAL ARRAY BOARD
VERTICAL ARRAY BOARD
3V-CPI PYLON ELECTRONICS
DSP1
DSP2
DSP3
DSP BOARD
FPGA1
FPGA2
ANALOG BOARD
SERIAL TO ETHERNET BOARD
POWER AND RELAY BOARD
IMG LASER
2D-S HORZ LASER
2D-S VERT LASER
CAMERA

3V-CPI ELECTRONICS BOARD CHANGES

- Master DSP and two 2D-S DSP's, one for each array board channel.
- Single or dual FPGA replacing 6 (total) memory and logic chips.
- FPGA logic achieves 200 m s^{-1} sample rates and single timing clock, in addition to reducing chip count and board complexity.
- Horizontal and Vertical lasers moved to independent boards for greatest spatial flexibility, including safest fiber-optic routing.
- Power and relay board will have more temperature control zones, PWM/PID heater controls

ELECTRONICS BOARD DESIGN STATUS

- Power distribution board (external to pylon) schematic capture complete.
- PDS (2D-S) laser board schematics complete.
- Power and relay board 50% complete. Awaiting further temperature zone definition.
- Diode array boards unchanged, ready for manufacture.
- Analog board not yet designed.
- Serial to ethernet board ready for manufacture.
- DSP board 50% complete. Awaiting FPGA design completion (currently active task).
- Schematics delivered as part of this design review

CONNECTOR AND CABLE STATUS

- All (wire) cable connectors ordered and received
- Hermetic pylon connectors identified and received
- Fiber-optic connector manufacturers identified and quotes obtained (ongoing). Price tag roughly $5000
- Wire cables specified. Burn test of chosen wire needs done by NCAR specified service. Where possible, wire already approved by NCAR will be used

3V-CPI SENSOR HEAD TOP LEVEL PACKAGE DESIGN AS OF 6/19/06

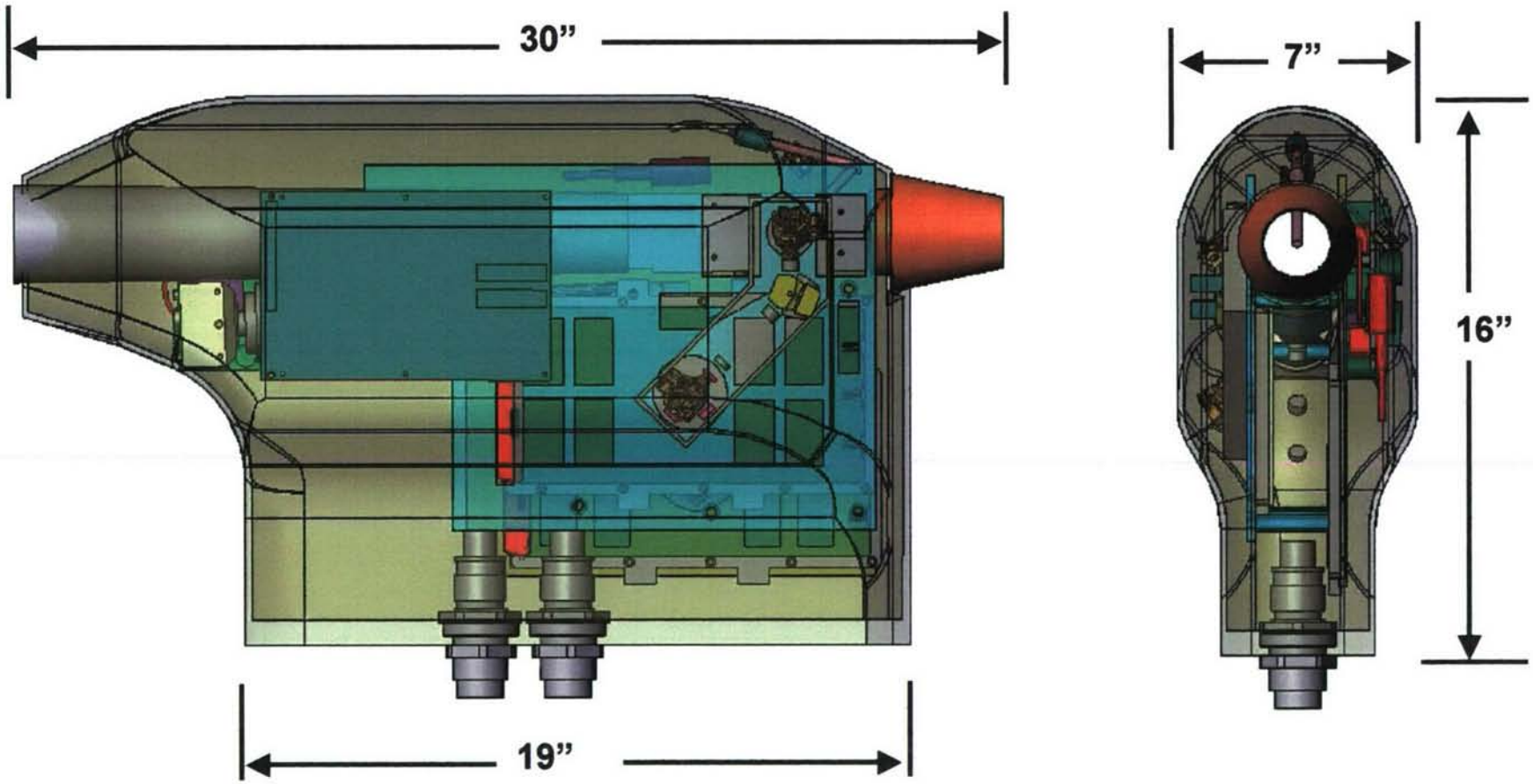

3V-CPI SENSOR HEAD COMPARED TO EXISTING VERSION 2 CPI

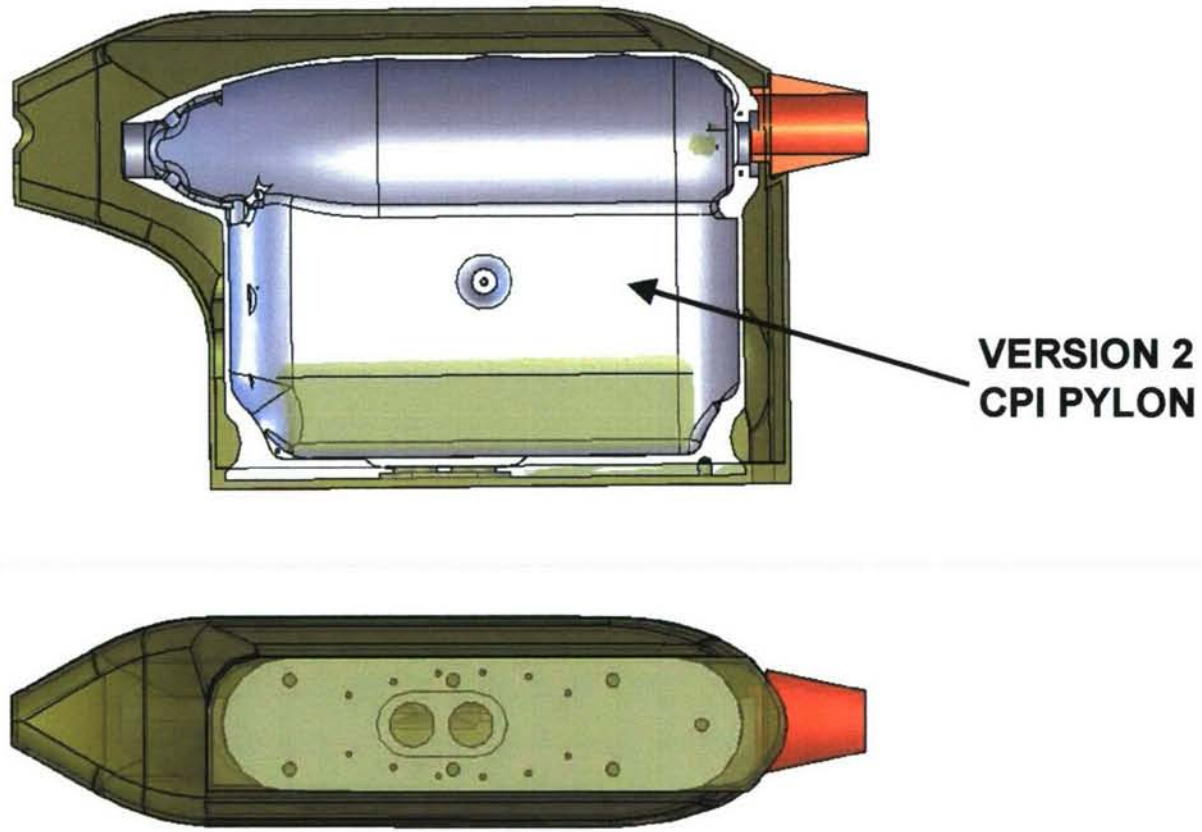

SUMMARY

- CPI IMAGE PROCESSING COMPUTER HAS BEEN PURCHASED AND IMAGE PROCESSING ALGORITHMS OPTIMIZED
- FIBER / POWER INTERFACE BOX DETAILED DESIGN ALMOST COMPLETE
- OPTICAL SYSTEM DESIGN AND TOP LEVEL OPTICAL LAYOUT COMPLETE
- TOP LEVEL PACKAGING DESIGN COMPLETE – READY TO BEGIN DETAILED MECHANICAL DESIGN
- ALL SYSTEM CONNECTORS RECEIVED OR IDENTIFIED
- ELECTRONICS SCHEMATIC CAPTURE IN PROGRESS

References

Baker, B. A., and R. P. Lawson, 2006: In situ observations of the microphysical properties of wave, cirrus and anvil clouds. Part 1: Wave clouds. *J. Atmos. Sci.,* **63**, 3160-3185.

Baumgardner, D. and A. Korolev, 1997: Airspeed corrections for optical array probe sample volumes. *J. Atmos. Oceanic Technol.,* **14,** 1224-1229.

Baumgardner, D., H. Jonsson, W. Dawson, D. O'Connor and R. Newton, 2001: The cloud, aerosol and precipitation spectrometer: a new instrument for cloud investigations. *Atmos. Res.*, **59-60**, 251-264.

Blyth, A. K., S. Lasher-Trapp, A. Cooper, C. Knight and J. Latham, 2003: The role of giant and ultra-giant nuclei in the formation of early radar echoes in warm cumulus clouds. *J. Atmos. Sci.*, **60**, 2557-2572.

Cober, Stewart G., George A. Isaac and Alexei V. Korolev, 2001: Assessing the Rosemount icing detector with in situ measurements. *J. Atmos. and Oceanic Technol.*, **18**, 4, 515-528.

Gayet J-F, P. R. Brown and F. Albers: 1993: A comparison on in-cloud measurements obtained with six PMS 2D-C probes. *J. Atmos. Ocean. Tech.*, **10**, 180-194.

Gayet, J-F, F. Auriol, A. Minikin, J. Ström, M. Seifert, R. Krejci, A. Petzold, G. Febvre, and U. Schumann, 2002: Quantitative measurement of the microphysical and optical properties of cirrus clouds with four different in situ probes: Evidence of small ice crystals. *Geophys. Res. Lett.*, **29,** 24, 2230 - 2233.

Jensen, J.B. and H. Granek, 2002: Optoelectronic simulation of the PMS 260X optical array probe and application to drizzle in a marine stratocumulus. *J. Atmos. and Oceanic Tech.*, **19**, 568-585.

Korolev, A. V., S. V. Kuznetsov, Y. E. Makarov, and V. S. Novikov, 1991: Evaluation of measurements of particle size and sample area from optical array probes. *J. Atmos. Oceanic Technol.,* **8,** 514-522.

Korolev, A.V., J.W. Strapp and G.A. Isaac, 1998: Evaluation of the Accuracy of PMS Optical Array Probes. *J. Atmos. Oceanic Technol.*, **15**, 708-720.

Korolev A. V. and G. A. Isaac, 2005: Shattering during Sampling by OAPs and HVPS. Part I: Snow Particles. *J. Atmos. Oceanic Technol.* **22**, 528-542.

Lawson, R.P., B.A. Baker, C.G. Schmitt and T.L. Jensen, 2001: An overview of microphysical properties of Arctic clouds observed in May and July during FIRE.ACE. *J. Geophys. Res.*, **106**, 14,989-15,014.

Lawson, R. P., D. O'Connor, P. Zmarzly, K. Weaver, B. A. Baker, Q. Mo, and H. Jonsson, 2006: The 2D-S (Stereo) Probe: Design and preliminary tests of a new airborne, high speed, high-resolution particle imaging probe. *J. Atmos. Oceanic Technol.*, **23**, 1462-1477.

Lawson, R. P., B. Pilson, B. Baker, Q. Mo, E. Jensen. L. Pfister and P. Bui, 2007: Microphysical Properties of subvisible cirrus. *J. Atmos. Chem. Phy., Discussions,* **7**, 6255 - 6292.

Mazin, I. P., A. V. Korolev, A. Heymsfield, G. A. Isaac and S. G. Cober, 2001: Thermodynamics of Icing Cylinder for Measurements of Liquid Water Content in Supercooled Clouds. *J. Atmos. and Oceanic Technol.*, **18**, 4, 529-542.

Nagel, D. 2003 – Personal Communication

NCAR 2003: Bulletin No. 9. Standard output data products from the NCAR Research Aviation Facility. Available at: http://raf.atd.ucar.edu/Bulletins/bulletin9.html

Rauber, R., C. Knight, H. Ochs and B. Stevens, 2003: Rain in Cumulus over the Ocean (RICO). *RICO Scientific Overview Document*, submitted to the National Science Foundation. (Available at http://rico.atmos.uiuc.edu/)

Strapp, J. Walter, Frank Albers, Andreas Reuter, A. V. Korolev, Uwe Maixner, E. Rashke and Z. Vukovic, 2001: Laboratory Measurements of the Response of a PMS OAP-2DC. *J. Atmos. and Oceanic Technol.*, **18**, 7, 1150-1170.

Appendix A
Reprint of:

Lawson, R. P., B. Pilson, B. Baker, Q. Mo, E. Jensen. L. Pfister and P. Bui, 2007: Microphysical properties of subvisible cirrus. *J. Atmos. Chem. Phy., Discussions,* **7**, 6255 - 6292.

AIRCRAFT MEASUREMENTS OF MICROPHYSICAL PROPERTIES OF SUBVISIBLE CIRRUS IN THE TROPICAL TROPOPAUSE LAYER

R. Paul Lawson[1], B. Pilson[1], B. Baker[1], Q. Mo[1], E. Jensen[2], L. Pfister[2] and P. Bui[2]
[1]SPEC Incorporated, Boulder CO, USA
[2]NASA Ames Research Center, Moffett Field, CA, USA

Abstract. Subvisible cirrus (SVC) clouds are often observed within the tropical tropopause layer (TTL) and have been shown to have a significant impact on the earth radiation budget. The Costa Rica Aura Validation Experiment (CR-AVE) sponsored by the National Aeronautics and Space Administration (NASA) took place near San Jose, Costa Rica from 14 January – 15 February 2006. The NASA WB-57F sampled SVC in the TTL from –75°C to -90°C with an improved set of cloud particle probes. The first digital images of ice particles in the TTL are compared with replicator images of ice particles collected in 1973 by a WB-57F in the TTL. The newer measurements reveal larger particles, on the order of 100 μm compared with < 50 μm from the earlier measurements, and also different particle shapes. The 1973 particles were mainly columnar and trigonal, whereas the newer measurements are quasi-spherical and hexagonal plates. The WB-57F also measured very high water vapor contents with some instruments, up to 4 ppmv, and aerosols with mixed organics and sulfates. It is unknown whether these ambient conditions were present in the 1973 studies, and whether such conditions have an influence on particle shape and the development of the large particles. A companion paper (Jensen et al. 2007) presents crystal growth calculations that suggest that the high water vapor measurements are required to grow ice particles to the observed sizes of 100 μm and larger.

1 Introduction

Subvisible cirrus (SVC) clouds appear mostly in the tropical tropopause layer (TTL) up to the tropopause (Wang et al. 1996; Beyerle et al. 1998; McFarquhar et al. 2000; Comstock et al. 2002; Clark 2005), but have also been observed at midlatitudes (Sassen and Campbell 2001; Immler and Schrems 2002). The TTL is the region of the tropical atmosphere that lies between the top of the main cumulus outflow layer and the thermal tropopause (Folkins et al. 1999). This layer is a transition layer between dynamical control of the vertical mass flux by tropospheric convection, and by the stratospheric Brewer-Dobson circulation, and is crucial to understanding the dehydration of air entering the stratosphere.

Although the radiative forcing of optically thin SVC is relatively small, the clouds generally cover a large horizontal extent and are considered to be radiatively significant (McFarquhar et al. 2000; Comstock et al. 2002). Using a nadir-pointing Nd:YAG lidar on a Learjet, McFarquhar et al. (2000) report that a spatially thin layer of cirrus, with both base and top above 15 km, was observed in the central Pacific Tropics 29% of the time, with a mean thickness of 0.47 km. Based on vertical profiles and a radiative transfer model, they calculate observed heating rates of up to 1.0 K day^{-1}, principally in the infrared, and cloud radiative forcing of up to 1.2 W m^{-2}. SVC clouds are occasionally observed above the tropopause at midlatitudes (Goldfarb et al. 2001) and in Polar Regions (Lelieveld et al., 1999; Kärcher and Solomon, 1999).

Supersaturation with respect to ice has been observed in the upper troposphere and lowermost stratosphere (Murphy et al. 1990; Gierens et al. 1999; Ovarlez et al. 2000; Jensen et al. 1999, 2001, 2005; Peter et al. 2006). Brewer (1949) showed that air entering the stratosphere is freeze dried as it crosses the cold tropical tropopause. Jensen et al. (1996) suggested that SVC can effectively freeze-dry air crossing the tropical tropopause to the observed lower stratospheric water vapor concentrations, which may significantly affect the Earth's radiation budget (Comstock et al. 2002).

SVC clouds were studied with the NASA WB-57F research aircraft in January - February 2006 during the Costa Rica – Aura Validation Experiment (CR-AVE http://cloud1.arc.nasa.gov/ave-costarica2). Figure 1 shows a photograph of the WB-57F and an example of an SVC layer as seen from the cockpit of the aircraft. While there have been several studies of SVC using airborne, satellite and ground-based lidar, there has been a relative dearth of in situ microphysical measurements.

correspondence to R. P. Lawson
(plawson@specinc.com)

Heymsfield (1986) and McFarquhar et al. (2000) discuss measurements made by a WB-57F in a SVC cloud at –84°C over the Marshall Islands on 17 December 1973. Based on an examination of replicator data, they concluded that particle sizes ranged from about 5 to 50 μm and particle shapes were mostly columnar and trigonal plates, with some hexagonal plates. The only other microphysical measurements in SVC that we are aware of have been made with scattering probes, such as the forward scattering spectrometer probe (FSSP) For example, Thomas et al. (2002) found a modal peak in the size distribution between about 2 and 17 μm, and Peter et al. (2003) found a model peak of 10 to 12 μm, both studies used an FSSP-300 (Baumgardner et al. 1992), which measured particles from 0.4 to 23 μm in size.

Fig 1. Photograph of (top) Subvisible Cirrus (SVC) layer taken from the cockpit of the NASA WB-57F (shown at bottom before sensors were installed) during the transit flight from Houston, Texas for the Costa Rica Aura Validation Experiment (CR-AVE). See acknowledgements for photo credit.

The microphysical measurements collected in SVC by the WB-57F research platform include, for the first time, digital images of particles from a cloud particle imager (CPI) probe (Lawson et al. 2001) a cloud and aerosol particle spectrometer (CAPS) probe (Baumgardner et al. 2001), and a new device, the 2D-S probe (Lawson et al. 2006). Data from the CPI, CAPS and 2D-S are analyzed from four WB-57F missions when all three instruments were functioning. Temperature, pressure and true airspeed measurements come from the WB-57F meteorological measurement system (Scott et al. 1990) and water vapor measurements are from the Harvard Integrated Cavity Output Spectroscopy (ICOS) instrument (Sayres 2006). The data presented here represent approximately 1,800 km of WB-57 F flight in SVC during the CR-AVE project. The CPI recorded 8524 images and the 2D-S probe recorded over 100,000 images of ice particles in SVC.

2 Instrumentation and data

A highlight of CR-AVE field campaign was the full complement of state-of-the art microphysical probes used to extensively investigate SVC. The combination of particle probes, CPI, 2D-S and CAPS, provided extensive overlap in particle size distributions and high-resolution digital images of the particles in SVC. Data for this paper were extracted from the CR-AVE archives. Before being placed in the archives, 2D-S data were averaged over 1 s, CPI data were averaged over 10 s and CAPS data were averaged over 30 s. In order to generate 1-Hz CAPS data that could be combined with 2D-S data, each 30-s averaged CAPS value was repeated 30 times. Both 2D-S and CAPS data were then used to generate a combined particle size distribution (PSD) and derived parameters on a 1 Hz basis. Since the ice particles did not exceed 165 μm in this study, particle shattering on probe inlets is not considered to be an issue (Field et al. 2003).

The CAPS contains two particle probes, a cloud and aerosol spectrometer (CAS), which measures forward and backward scattered light to count and size particles from 0.5 to 50 μm, and a cloud imaging probe that images particles from 75 to 1600 μm with 25 μm pixels. The CPI has 2.3 μm pixels, which provides high-resolution digital images of ice particles in SVC, but the relatively small CPI sample volume (a maximum of 0.7 L s^{-1}) compared with optical array probes, limits its ability to adequately represent the entire particle size distribution. The 2D-S is a new imaging probe that has true 10 μm per pixel resolution at jet aircraft airspeeds, whereas the response of the older 2D imaging probes is degraded with airspeed. At the true airspeed of the WB-57F (about 180 m s^{-1} at 55,000 ft), the older 2D imaging probes do not detect particles with sizes

less than 50 to 100 μm (Lawson et al. 2006). Figure 2 shows photographs of the CPI and 2D-S probes that were installed on the WB-57F for CR-AVE.

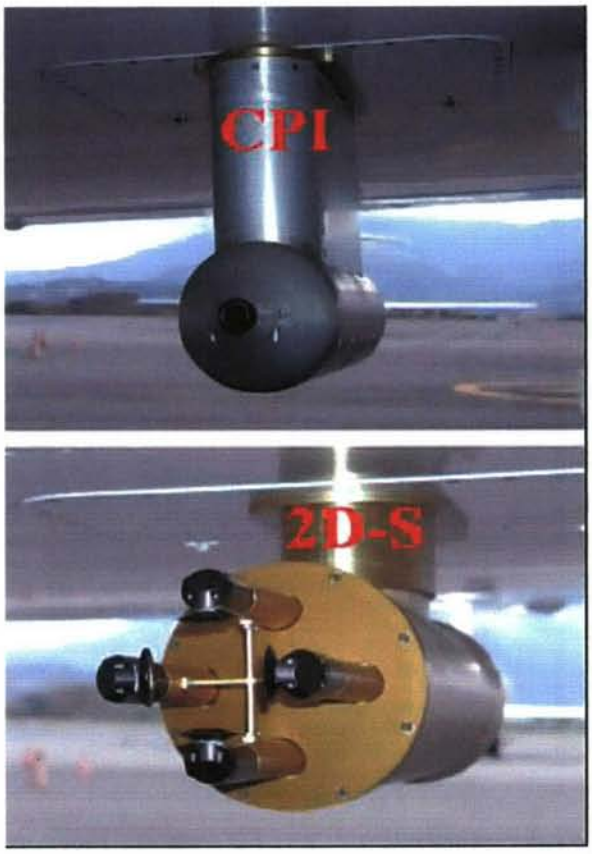

Fig 2. Photographs of the CPI and 2D-S probes installed under the left wing of the NASA WB-57F for the CR-AVE project.

The true 10 μm resolution of the 2D-S facilitates resizing of out-of-focus images, which has otherwise been a source of error that has hampered older 2D imaging probes (Korolev et al. 1998). Examples of 2D-S images in SVC and re-sizing using an algorithm developed by Korolev (2007) are shown in Fig. 3. The algorithm is based on theoretical diffraction and has been evaluated using images of glass beads in the laboratory. The Korolev algorithm was tested on several bead sizes, and it performed better on some sizes than it did on others, for reasons that are unknown at this time. Later in this paper (Fig. 10) we show results of a PSD that has been resized using the Korolev (2007) algorithm compared with a PSD computed using only in-focus 2D-S images.

Water vapor was measured with multiple instruments on the WB-57F during the CRAVE flights. The Harvard water vapor instrument photodissociates H2O molecules with 121.6 nm (Lyman-α) radiation and detects the resulting OH photofragment fluorescence at 315 nm (Weinstock et al., 1994). The Harvard ICOS instrument uses a mid-infrared quantum cascade laser at 1484 cm^{-1} to obtain measurements of H2O, as well water vapor isotopes, with an effective path length of nearly 4 km (Sayres 2006). The Jet Propulsion Laboratory Laser Hygrometer (JLH) is a tunable-diode laser focused that operates by harmonic wavelength modulation spectroscopy (May 1998). For over 50 years measurements of water vapor concentration in the TTL have been conducted using balloon-borne instrumentation, typically frost-point chilled mirrors (Oltmans et. al. 2000). A long-standing discrepancy has persisted between the frostpoint H2O measurements and aircraft-borne H2O measurements made using a variety of techniques. This discrepancy was particularly glaring under the very dry tropopause conditions sampled during CR-AVE, with the frostpoint and JLH measurements typically reporting 1-2 ppmv whereas the ICOS and Harvard Water Vapor instruments report 3-4 ppmv. This discrepancy in water vapor measurements is germane to this paper, because calculations shown in Jensen et al. (2007) suggest that water vapor limits the maximum size to which ice particles can grow before they fall out of the upper region of the TTL.

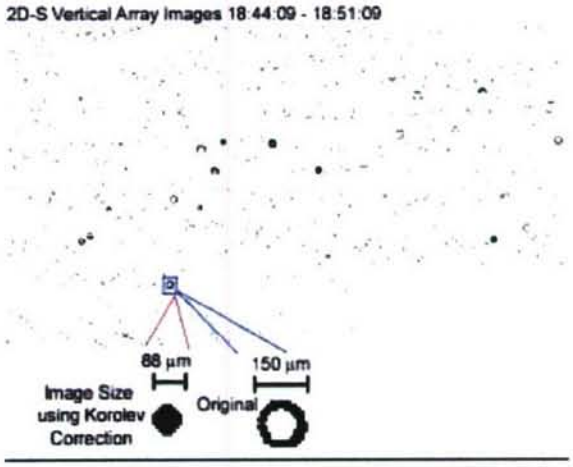

Fig 3. 2D-S particle images from the vertical (V) channel of the 2D-S probe and an example of size correction of a donut image using the Korolev (2007) resizing scheme.

3 Characteristics of subvisible cirrus

3.1 Spatial and vertical extent

Figure 4 shows the WB-57F flight track on the transit flight (TF 1) to San Jose, Costa Rica on 14 January 2006, and flight tracks for five research flights: RF 1 (17 January 2006), RF 5 (25 January 2006), RF 8 (1 February 2006), RF 9 (2 February 2006) and RF 11 (7 February 2006). These are flights when there were CPI data available. CPI data were used to identify regions when the WB-57F was in SVC, because out of all the particle probes, it was the most reliable indicator of SVC. CPI data were also used to determine the shape of ice particles, because of its high-resolution imagery. Both CAPS and 2D-S data were available for TF 1, RF 5, RF 8 and RF 9, and data from these missions were used to compute the mean PSD's and average bulk parameters computed in SVC. Also shown in Fig. 4 are vertical profiles of the transit flight and research flights where the CPI observed SVC. The data in Fig. 4 show that SVC was frequently observed and that it was consistently found between about 53,000 ft (16.2 km) and 58,000 ft (17.7 km) msl, which corresponds to a temperature range from about – 75 to – 85°C.

As suggested in Fig. 4, the WB-57F was generally in and out of SVC clouds during its mission profile, and sometimes porpoised from the top to the bottom of the cloud layer. To avoid averaging regions of clear air with SVC cloud, the missions were divided into flight legs that were chosen when the average 2D-S particle concentration was > 5 L^{-1} for 5-km or greater without a containing continuous period of clear air (2D-S concentration < 0.01 L^{-1}) that was 1-km or greater. This resulted in 19 flight legs that were about 25 to 200 km in length, with one very long leg that extended for 2,400 km. Figure 5 shows an example of flight legs that were used for making PSD's from a time series of 2D-S particle concentration during a portion of the mission on 2 February 2006.

3.2 Particle habits

Figure 6 shows examples of CPI images in SVC that have been sorted into particles < 65 μm and particles ≥ 65 μm in maximum dimension. The 65 μm dimension was chosen because visual inspection showed that the shape of the CPI images typically changed at about this size. Images < 65 μm appear to be mostly quasi-spherical and there is little light transmission through the images. Images ≥ 65 μm start to appear disk shaped, with distinctive edges that are not apparent in the smaller spheroidal images. Also, several of the images ≥ 65 μm start to take on a plate-like shape. This can be seen more clearly in Fig. 7, which shows expanded views of several of the particles and reveals the distinctive edges on the basal faces of the particles, clearly revealing hexagonal crystal structure.

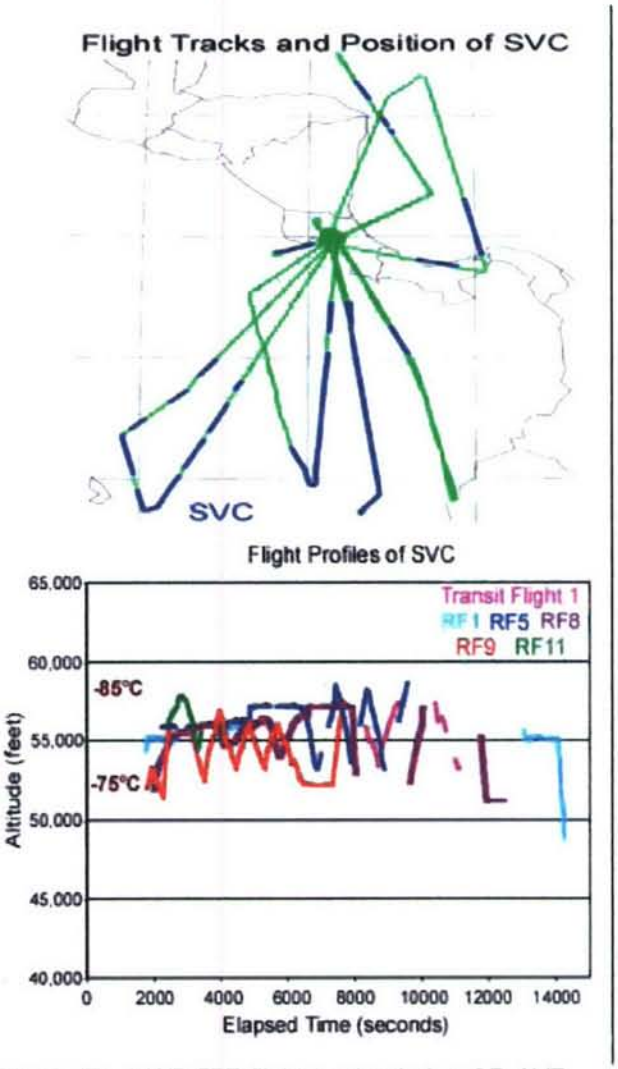

Fig 4. (Top) WB-57F flight tracks during CR-AVE showing (in blue) regions where SVC was encountered and (Bottom) vertical profile showing location of SVC. The color code in the right panel corresponds with the research flight (RF) number shown in the legend.

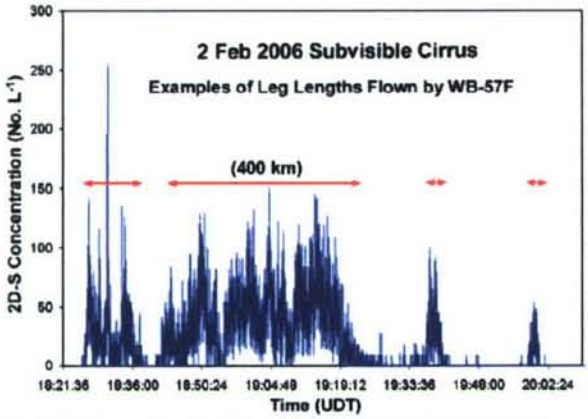

Fig 5. Example of a time series of WB-57F 2D-S total particle concentration in SVC showing 4 of the 19 "legs" (red arrows) used in the analyses in this paper. Legs were selected using an objective criteria explained in the text.

The CPI images in Figs. 6 and 7 are in sharp contrast to the only other known images of ice particles in the TTL, which were collected on 17 December 1973 using a replicator installed on a WB-57F research aircraft flying between 16.2 and 16.7 km (-83°C to -84°C) over the Marshall Islands (Heymsfield 1986; McFarquhar et al. 2000). Heymsfield (1986) shows a few images where the shapes of the ice particles are mostly columnar and trigonal (with some plates), ranging in size from about 5 to 50 μm.

In order to be certain that the CPI images have disk-like edges that are not an optical aberration, we captured images of 80 μm glass beads using the CR-AVE CPI in the laboratory and examined images on all locations in the CPI viewing volume. A few images of glass beads that come the closest to producing what appears to be an edge are also shown in Fig. 7. It is apparent from comparing the ice particle images in SVC with the images of spherical glass beads that, most likely, the edges are not an optical aberration of a (glass) sphere. Also, we could not find any evidence of disk-like edges upon examining quasi-spherical images of 50 to 100 μm ice particles in anvil cirrus observed during CR-AVE, further suggesting that the disk-like and plate-like SVC ice particles are real.

A geometric analysis of a CPI image (Appendix A) suggests that the aspect ratio (basal to prism faces) is on the order of 6:1. However, it is not possible from this crystal image to determine if the aspect ratio is actually larger than 6:1, because of the amount of blur in the image due to diffraction and optical aberrations. For example, the CPI image in the lower left frame of the plate-like images in Fig. 7 appears to have an aspect ratio of 6:1, assuming it is a plate being viewed orthogonal to the prism face (and 1:6 if it is actually a column). However, if it is a tilted plate, it will actually have a slightly larger aspect ratio. Also, if the prism face is significantly blurred due to diffraction and optical aberrations, the dimension of the prism face will be artificially lengthened, and the aspect ratio will be erroneously decreased.

The aspect ratio of these larger crystals is germane to the crystal growth calculations and relative humidity measurements presented in a companion paper (Jensen et al. 2007). In this paper we choose not to offer an estimate of the largest likely aspect ratio of these crystals, since any estimate will contain some degree of ambiguity and will be a subjective analysis of thickness of the image edge.

Figure 8 shows histograms of particle habits classified by a trained analyst for all of the CPI images collected in SVC and from only those images ≥ 65 μm. The histograms comparison between particles < 65 μm and those ≥ 65 μm shows considerably fewer quasi-spheroids in the larger particle histogram and a significant increase in plate-like and edged irregulars (also note that the "columns" may be plates viewed on edge).

The CR-AVE data in SVC observed near Costa Rica contained a few particles that were significantly larger (by about 100 μm) and markedly different crystal habits than the observations reported by Heymsfield (1986) over the Marshall Islands. The lack of trigonal ice in the CR-AVE SVC data set is curious. The replicator images shown in Heymsfield (1986) are clearly trigonal. The CPI images are not quite as sharp as the replicator images, but once particles are larger than about 30 μm, trigonal shapes will be clearly identifiable, if they exist. Thus, the differences in particle habits between the Heymsfield (1986) case and the CR-AVE data set cannot be attributed to instrumental effects. The data set collected in 1973 is 33 years previous to the CR-AVE data, and the possibility exists that differences in the moisture field and atmospheric chemistry have changed over the past three decades; however, moisture and chemistry instrumentation was not installed on the WB-57F for the 1973 flights.

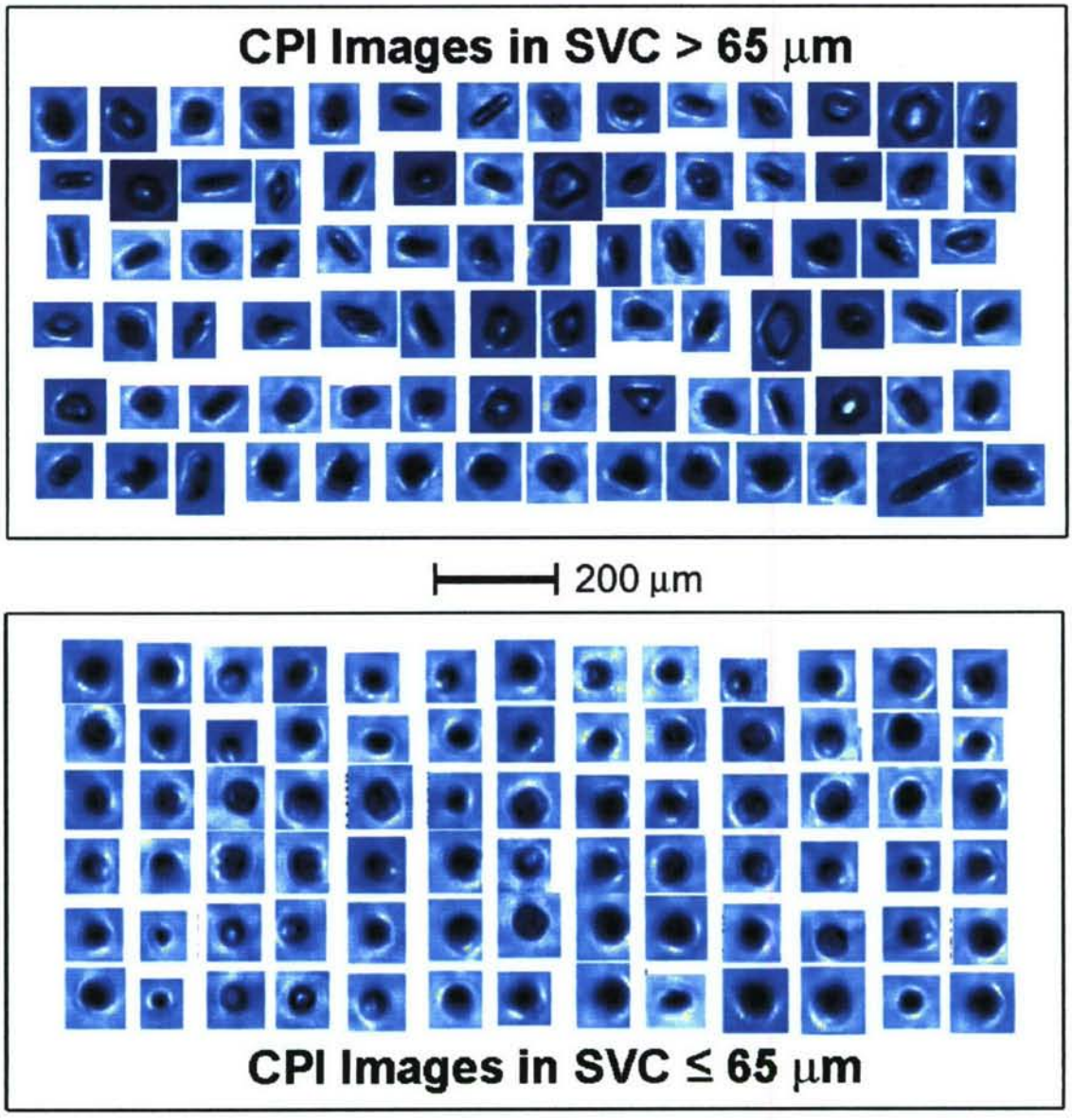

Fig. 6. Examples of CPI images in subvisible cirrus (SVC) of (top) ice particles > 65 μm and (bottom) ≤ 65 μm.

3.3 Particle size distributions (PSD's) and bulk properties

Figure 9 shows PSD's as a function of number, area and mass, based on ~1800 km of WB-57F flight in SVC during the four missions discussed in Sect. 3.1. Compared with the 2D-S mean PSD, there is a sharp drop in the CAPS (CAS) mean concentration at 5 μm. The CAS data applies Mie scattering theory to size particles, and implicit in Mie theory is the assumption that the particles are perfect spheres. Since the CAS is sizing ice that is not perfectly spherical, the sizing uncertainty is unknown. Also, it uses three stages of gain amplifiers, and the transition from one of the stages to another occurs at 5 μm (where the dip starts in the CAPS PSD). We chose to use the 2D-S PSD in the size region from 10 to 30 μm region and interpolate between CAS and 2D-S

between 5 and 10 μm. Figure 9 shows that, compared with the 2D-S, the CAPS indicates a higher concentration in the size range from 50 to 150 μm, and that it recorded particles as large as 225 μm, while the largest 2D-S particle was 165 μm. Both the CAPS and 2D-S data were processed using image-resizing schemes based on Korolev (2007). A check on 2D-S resizing was accomplished by comparing a PSD of infocus images with resized images using the Korolev (2007) technique. However, there were only 18 2D-S particles > 100 μm in the CR-AVE data set and only a few of these were in focus, so a comparison using the CR-AVE data set would not produce adequate statistics. Instead, a very large data set (137,222 total 2D-S images with 5,601 images > 100 μm) collected in drizzle during the 2005 Rain in Cumulus over the Ocean (RICO) experiment was processed. The RICO drizzle images appear very similar in shape to the quasi-spherical SVC images.

Figure 10 shows the results of comparing PSD's using only infocus 2D-S images with all images processed using standard 2D technique (i.e., the maximum image dimension across the array) and images resized using the Korolev (2007) scheme. Appendix B discusses sizing errors using only infocus images, which will usually result in a PSD with the smallest particle sizes. In Fig. 9, using infocus images does produce the smallest PSD, while the PSD produced based on the Korolev (2007) algorithm falls between the infocus and standard processing PSD. Based on the comparisons shown in Figs. 9 and 10, it appears that the 2D-S produces more reliable information in from 10 to 165 μm (the largest 2D-S particle size observed), and therefore the 2D-S data are used in that size range.

McFarquhar et al. (2000) show data in SVC from a Particle Measuring Systems (PMS) axially scattering spectrometer probe (ASSP) with a size range from 2 to 30 μm, and PMS 1-D probe that is intended to size particles from 20 to 300 μm. However, recent studies (Lawson et al. 2006) suggest that the slow time response of the 1-D probe, which uses a diode array and front-end amplifier comparable to the 2D-C, limit its response to particles larger than about 100 μm at the Learjet airspeeds used in that study. The PSD shown in Fig. 1 in McFarquhar et al. (2000) extends from 2 to 15 μm, with some 1-D probe activity in the 20 to 50 μm size range. However, these are likely to be much larger particles that are undersized due to limitations imposed by the time response of the 1-D probe. Interestingly, the ASSP PSD that extends from 2 to 15 μm shown by McFarquhar et al. (2000) is similar to the composite CR-AVE PSD shown in Fig. 9, (but it is not similar to the CAS PSD alone). Figure 9 also shows average composite PSD's as a function of particle area and particle mass. The particle area size distribution strongly influences optical cloud properties, such as extinction and optical depth. The particle mass size distribution has an impact on ice water content (IWC) and ice water path.

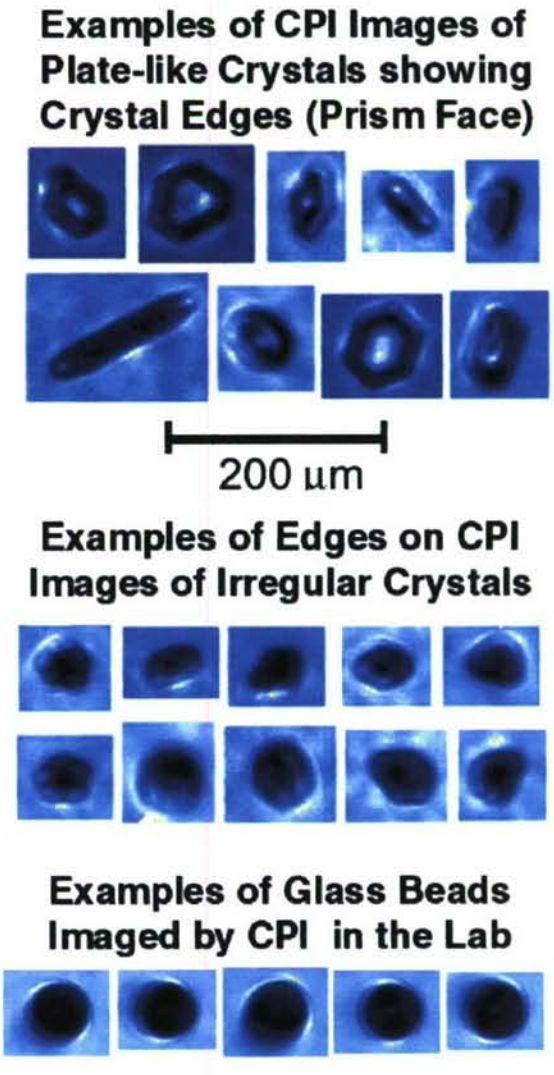

Fig. 7. Examples of CPI images in SVC that show edges (prism faces) of the larger plate-like and irregular crystals, and examples of images of glass beads taken in the laboratory for the sake of comparison.

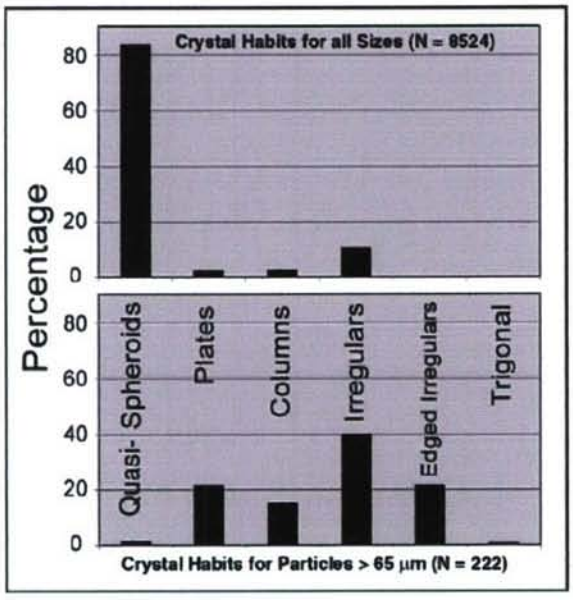

Fig. 8. Comparison of crystal habits for (top) all crystals and (bottom) crystals > 65 μm in SVC. Particle habits were classified manually based on CPI images.

The average bulk properties shown in Table 1 were derived by computing a time-weighted average from each of the 19 WB-57F legs in SVC (i.e., the sum of the number of 1-Hz data points in each leg times the leg average divided by total number of data points in all legs). The average particle concentration (66 L^{-1}), extinction coefficient (0.009 km^{-1}), effective radius (8.82 μm) and IWC (0.055 mg m^{-3}) are very close to values derived from graphs shown in McFarquhar et al. (2000). McFarquhar et al. measured IWC values from 0.001 to 0.1 mg m^{-3}, and show an average value of about 0.05 during a descent through SVC in their Fig. 2. They measured a value of about 11 μm for effective radius on the same flight. Based on cloud lidar system (CLS) measurements from the NASA ER-2 research aircraft, McFarquhar et al. show a mean value of τ = 0.045 for optical depth, based on an average CLS cloud thickness measurement of 0.47 km. Using WB-57F porpoising maneuvers to estimate SVC thickness in CR-AVE yields a range from about 0.5 to 1 km, which translates to an optical depth of 0.045 to 0.09.

Jensen and Pfister (2004) simulated formation of TTL cirrus along trajectory curtains throughout the tropics using a detailed cloud model. Temperature profiles in the model were taken from meteorological analyses with wave-driven perturbations superimposed. The model tracks the growth and sedimentation of thousands of individual ice crystals within each column of air (see Jensen and Pfister, (2004) for details). The simulated mean ice concentration (55 L^{-1}) and effective radius (7.3 μm) agree remarkably well with CR-AVE measurements (Table 1). Note that if we do not include gravity wave-driven temperature perturbations in the model, then the simulated ice concentrations (18 L^{-1}) are much lower than the observed values (66 L^{-1}).

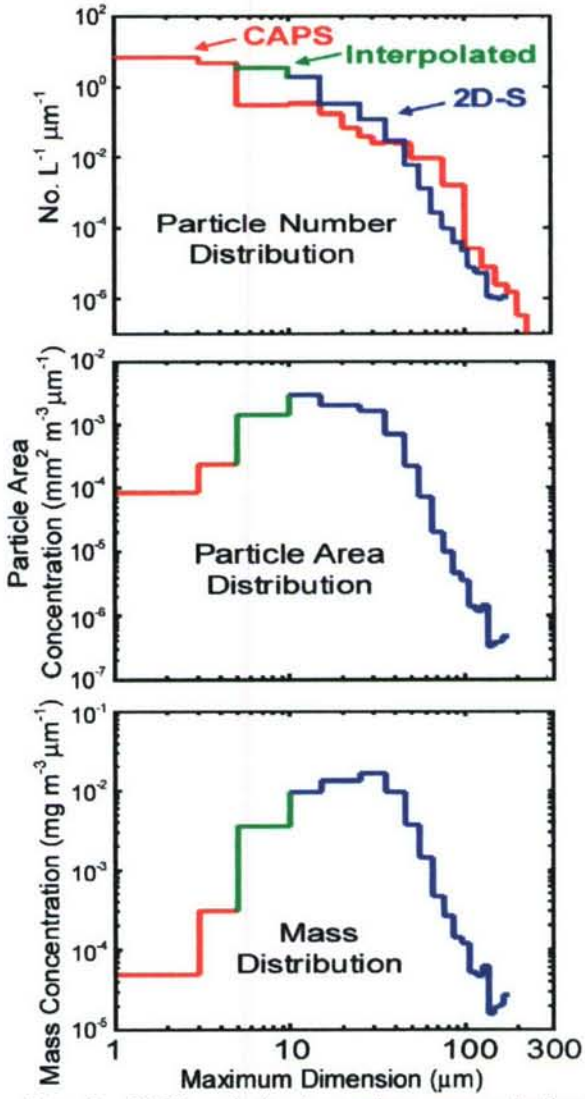

Fig. 9. PSD's of (top) number concentration, (middle) area and (bottom) mass based on ~1800 km of WB-57F 2D-S and CAPS measurements collected in SVC. Green trace is interpolated between 5 μm CAS and 10 μm 2D-S size bins.

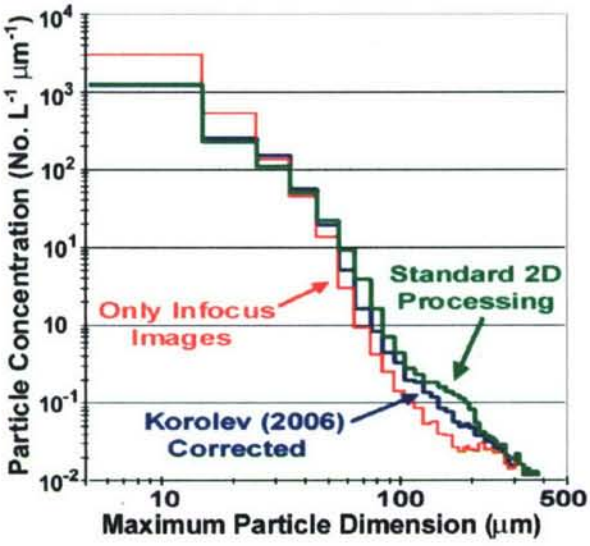

Fig. 10. Comparison of PSD's from drizzle observed in the RICO project using (green) standard 2D processing technique, (red) only in-focus 2D-S images and (blue) images that have been resized based on the Korolev (2007) algorithm.

Table 1. Bulk properties of SVC observed by the WB-57F on 4 missions, and particle concentration and R_{eff} from numerical simulations (Jensen and Pfister 2004). Means and standard deviations (σ) are an average of 8738 1-Hz averaged measurements collected by WB-57F from 19 legs in SVC. Max and Min are leg-averaged maximums and minimums of the 19 legs.

	Mean	σ	Max	Min
Particle Concentration (No. L^{-1}): WB-57F	66.0	30.8	188.8	22.5
Simulation	55			
Particle Concentration > 65 μm (No. L^{-1})	0.004	0.017	0.08	0.00
R_{eff} (μm): WB-57F	8.82	2.44	16.7	5.51
Simulation	7.3			
Extinction (km^{-1})	0.009	0.011	0.063	0.002
IWC (mg m^{-3})	0.055	0.098	0.503	0.012

3.4 Large particles

The ice particles observed in SVC during CR-AVE extend to larger sizes than previously reported by Heymsfield (1986), McFarquhar et al. (2000) and Thomas et al. (2002). There were 35 measurements out of a total of 8738 1-Hz 2D-S measurements that contained ice particles ≥ 100 μm, and the maximum infocus particle size observed is 165 μm. The maximum length of the largest CPI image is 151 μm. However, the previous investigations were incapable of properly measuring these larger particles (with the possible exception of the replicator used by Heymsfield 1986). McFarquhar et al. do mention that collateral studies in 1973 with the Aeromet Learjet near the Marshall Islands using PMS probes report ice particles up to 140 μm in thin cirrus between 14 and 15 km (45,000 and 49,000 ft), but these clouds are much lower than the SVC that exists at the base of the tropopause.

While the larger particles occasionally observed during CR-AVE do not have a significant impact on bulk microphysical properties, they do raise the question of how such relatively large particles can exist near the tropopause. Jensen et al. (2007) use back trajectory analysis to show that the crystals did not originate in convection. The large-scale vertical ascent velocity in the TTL has been estimated to be low, on the order of a cm s^{-1} or less (Heymsfield 1986). Growth-sedimentation calculations suggest the crystals cannot grow to these sizes before falling out of the supersaturated TTL layer unless the ice supersaturations are on the order of 100% or more (Jensen et al. 2007). This gives rise to discussions of discrepancies in results from different water vapor measurement technologies that are used in the TTL.

Balloon-borne measurements of frostpoint temperature in the TTL began in 1949 (Barrett et al 1950) and have been considered the only reliable technology until the recent development of tunable diode and quantum cavity lasers (May 1998; Sayres 2006).[1] The growth of large ice particles and how this process is affected by measurements of water vapor in the TTL is the subject of a companion paper (Jensen et al. 2007). In this paper we consider some relationships between ice particle size and water vapor measurements from the ICOS.

[1] A workshop that focused on discrepancies between balloon-borne frostpoint and laser-based measurements of water vapor and other aspects of the TTL was convened by NASA in November 2006

Figure 11 shows a plot of maximum particle size versus ICOS water vapor for 8,734 1-Hz measurements of water vapor in the TTL. The ICOS archived measurements were used only when the instrument had stabilized after passing through regions with high water concentrations, and missing 1-Hz ICOS measurements were interpolated using existing measurements. The relationship between maximum particle size and relative humidity with respect to ice (RH_{ice}) shows a subtle trend whereby the largest particles are only observed in regions at high RH_{ice}. For example, all of the SVC particles $\geq$ 120 μm are observed at $RH_{ice} \geq 125\%$. However, there was no observable trend when maximum particle size was plotted against total particle concentration and mean particle size.

Fig. 12 shows a time series with RH_{ice}, temperature, total particle concentration and total particle surface area on 22 January 2006 where appreciable ice is only found at $RH_{ice} > 150\%$, and even higher values of RH_{ice} correspond with the lowest values of both total particle concentration and total particle surface area. Extensive measurements of water vapor in mid-latitude cirrus at temperatures < –40°C in both the northern and southern hemispheres show that more than 75% of the measurements in both hemispheres range between $90\% < RH_{ice} < 110\%$ (Ovarlez et al. 2002). The authors suggest that the predominance of $RH_{ice} \approx 100\%$ measurements is a result of an equilibrium condition in these cirrus clouds. In contrast, Figure 13 shows that more than half of the CR-AVE ICOS RH_{ice} measurements in SVC exceeded 160%, which Koop et al. (2000) suggests is the value at which homogeneous nucleation occurs. Murphy et al. (2006) and Murphy (2007 – personal communication) report that TTL aerosols are composed mainly of sulfates mixed with organics. The obvious differences between the mid-latitude cirrus data and our observations are the colder temperatures and unusual aerosol chemistry in the upper TTL. However, there are no obvious physical mechanisms that explain the observed SVC particle sizes and shapes.

4 Summary

During the 2006 CR-AVE project staged from Costa Rica, the NASA WB-57F often observed SVC in the temperature range from –75° to –85° C within about 1 km of the tropopause between about 0 and 10° N Latitude. The average ice particle number concentration (66 L^{-1}), extinction coefficient (0.009 km^{-1}), ice water content (0.055 mg m^{-3}), effective radius (8.82 μm) and optical depth (0.045 to 0.09) are similar to values computed from in situ measurements over the Marshall Islands by McFarquhar et al. (2000). However, CPI images of the ice particles observed in CR-AVE were markedly different, with 84% of the particles being quasi-spherical, and particles larger than about 65 μm exhibiting disk-shaped and hexplate characteristics. In comparison, McFarquhar et al. (2000) report a 50% mixture of columns and trigonal plates (based on Heymsfield (1986) replicator data collected in 1973).

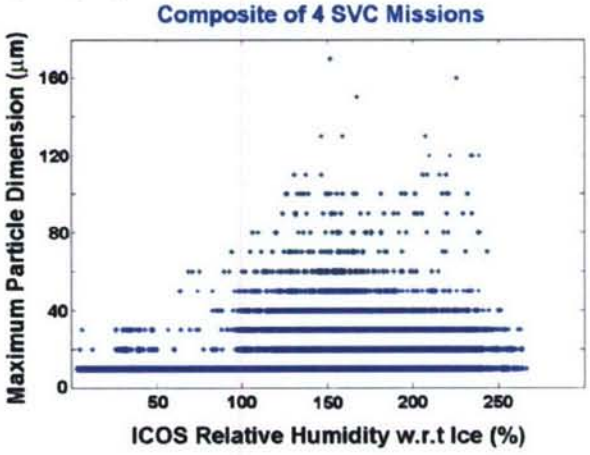

Fig. 11. Plot of maximum particle dimension from 1-Hz 2D-S data in 10 μm bins versus ICOS RH_{ice}.

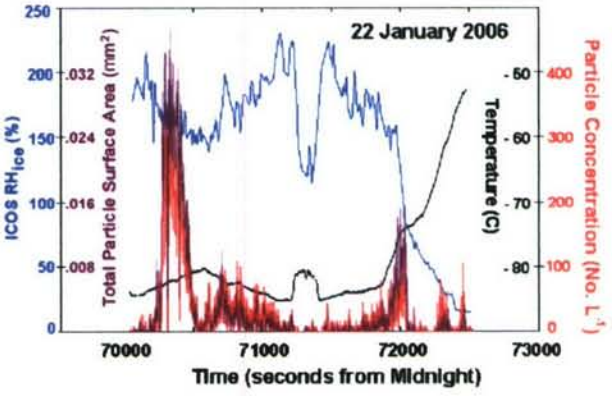

Fig. 12. Example of time series of 2D-S particle concentration, temperature and ICOS RH_{ice}

Also, the size of CR-AVE particles extended to 165 μm, while McFarquhar et al. (2000) found the largest particles in TTL SVC were 50 μm, in both

the 1973 WB-57F study and an investigation in 1993 using a Learjet.

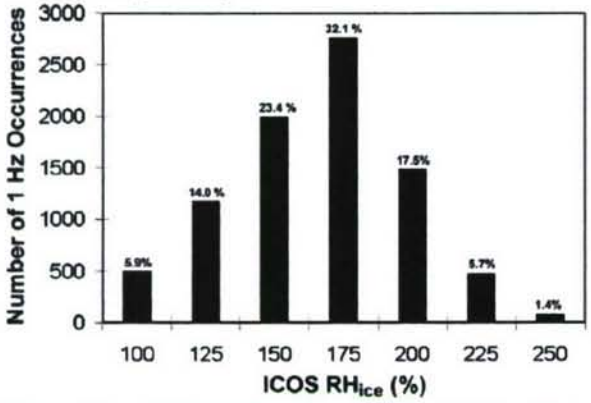

Fig. 13. Histogram of 8560 ICOS RH_{ice} measurements in SVC when RH_{ice} exceeded 100%.

The apparent difference in particle size between the Heymsfield (1986) data and recent CR-AVE measurements may be due to limitations of the PMS 1-D probe used in the earlier studies (Lawson et al. 2006). However, the difference in the shape of the particles appears to be real and is not readily explained. One possible difference is that very high relative humidity (in excess of 200%) observed by the WB-57F during CR-AVE was not present in the 1973 case reported by Heymsfield (1986). Based on a numerical model, Jensen et al. (2007) show that, for crystals with aspect ratios of 6:1 or less, 3 to 4 ppmv water vapor (i.e., about 200% to 250% RH_{ice} at -85°C) is necessary to grow ice particles with sizes on the order of 100 μm within about 500 m of the tropopause. Also, chemistry measurements near Costa Rica in 2004 and during CR-AVE suggest that the TTL is composed mainly of sulfates mixed with organics (Murphy et al. 2006; Murphy 2007 – personal communication). Nucleation and growth of ice particles at -85°C in the presence of sulfates mixed with organics and very high relative humidity are mechanisms that need to be investigated more thoroughly, perhaps with the aid of cloud chamber experiments.

Appendix A Calculation of particle aspect ratio from CPI images

Two-dimensional particle imagery (e.g., CPI images) limits the amount of three-dimensional information retrievable from any given image. However, the aspect ratio (an essentially two-dimensional quantity) can be estimated from some CPI images that view the crystal from a fortuitous angle. Estimates of particle aspect ratio (i.e., ratio of dimensions of basal to prism faces) based on a CPI image from the CR-AVE data set that reveals three-dimensional qualities are discussed in this Appendix.

Figure A1 shows a magnified and rotated view of the crystal third from the left in the top row of images in Fig. 7. The crystal appears to be a hexagonal plate viewed from such an angle that a basal face and at least two prism faces are seen. Assuming hexagonal symmetry an estimate of the view direction and thus of the aspect ratio can be made. Drawn over the image in Fig. A1 are yellow lines approximating the locations of the six edges of the basal face. The relative (i.e. arbitrary units) lengths of these lines are indicated in yellow as well. Opposite edges of the basal face are similar in length as expected by symmetry.

Let *A* represent the average length of the shortest pair of basal edges (i.e. 39.5), *B* represent the average of the mid-length pair (i.e. 86.5), and *C* the average of the longest pair of edges (i.e. 99.5). Let Φ represent the angle between the normal to the crystal's basal face (i.e. the c-axis) and the view direction and θ the angle between the red line in the plane of the basal face and the projection of the viewing direction onto the same plane. Let *L* represent the true length of the edges (in the same arbitrary units). Basic trigonometry assuming a hexagonal plate yields:

$$A^2/L^2 = \cos^2(\Phi)\cos^2(\Theta) + \sin^2(\Theta)$$
$$B^2/L^2 = \cos^2(\Phi)\cos^2(60-\Theta) + \sin^2(60-\Theta)$$
$$C^2/L^2 = \cos^2(\Phi)\cos^2(60+\Theta) + \sin^2(60+\Theta)$$

Solving these equations for the values of *A, B, and C* specified, yields: $L \approx 106$, $\theta \approx 8°$, and $\Phi \approx 70°$.

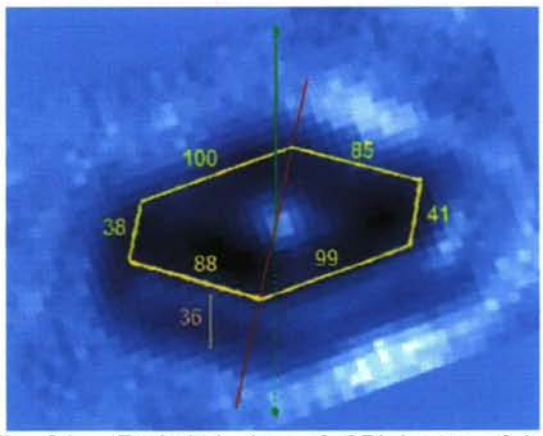

Fig A1. Exploded view of CPI image of ice particle shown in Fig. 7. See text for explanation of lines and numbers.

The pink line represents the thickness of the plate from the view angle. It's length (36), in the same arbitrary units, must be divided by *sin(Φ)* to obtain an estimate of the actual thickness (*TH*). The aspect ratio is then the ratio of *2L / TH* or about 5.5:1. The largest uncertainty is in the choice of the thickness (pink line). Figure 7 shows that the CPI optics can blur edges making them look thicker than they are. If this is causing an exaggeration of the thickness then we may be underestimating the aspect ratio. Therefore, we conclude that the aspect ratio of this crystal is on the order of 6:1.

Appendix B Uncertainty in the size of ice particle images

B.1 2D-S Images

For 2D-S images that appear to be in focus (i.e., all pixels are black; there are no white pixels in the center), there are three sources of uncertainty. Each are considered in turn below:

i. Uncertainty due to the effective pixel size of the photo diodes in the sample volume. For the 2D-S the effective pixel size is 10 μm.

ii. Uncertainty in the calibration of effective pixel size due to uncertainty in the laboratory calibration of glass beads used to determine effective pixel size. Based on discussion with the bead manufacturer, Duke Scientific, this uncertainty is about 5% of the image size.

iii. An image can be somewhat out of focus, thus enlarged, and still appear in-focus (all image pixels are black; no white pixels in the center). Using the tables found in Korolev (2007), the result depends on the size of the image rather than being a fixed value, or fixed percentage as discussed above in items ***i*** and ***ii***. Estimates of the maximum error are shown as function of image size in Table B1, based on the following discussion.

Table B1 shows calculations of actual image sizes (D_o) for six apparent image sizes (D_m = 50, 75, 100, 125, 150, 175 μm) that are slightly out of focus, but not sufficiently to produce a white (Poisson) spot in the middle of the image. For item iii, the error is always in the direction of an overestimation of the size. Therefore we find the maximum overestimation, minimum size, possible by first assuming the effect of (1) above has caused a 10 μm overestimate of the apparent size, and then assuming it is also out of focus as much as possible and still not have a spot. The 3rd column in Table 1 is the ratio of the spot size [(D_s)] to apparent size, (from Korolev 2007). Using D_s of 15 μm yields a Z_d (normalized distance from the focal plane from Korolev 2007 Table B1 column 1) and the ratio of apparent size to actual size (from Korolev 2007 Table B1 column 2 ,our column 5), from which D_o is computed. The maximum underestimation, or maximum possible size, is estimated as D_m+10.

B.2 CPI images

Unlike the 2D-S probe, the CPI is designed to maximize detection and imaging of only infocus images. It is, however, possible for CPI images to be out of focus, but unlike the 2D-S probe that has only one gray level (i.e., black), the CPI images particles with 256 gray levels. This significant increase in shading allows the eye to readily identify CPI images that are infocus, especially when the images have relatively sharp corners and regular structures, such as the plates shown in Fig 7 in the text. Thus, uncertainty in the size of infocus CPI images reduces to the pixel size (2.3 μm) plus the amount of blur that results from optical aberrations. Based on laboratory evaluation, the amount of blur is estimated to be equivalent to about one pixel, so the total maximum uncertainty in CPI images that are in focus is estimated to be about 5 μm.

Table B1: D_m is the observed size along the array. D_o is the smallest possible image size (i.e., the actual particle when in focus) and D_m +10 is the largest possible image size given errors discussed in the text.

Dm	D_m - 10	$D_s/(D_m$-10)	Z_d	$(D_m$-10)/D_o	D_o	D_m+10
50.000	40.000	0.375	2.420	1.166	34.299	60.000
75.000	65.000	0.231	1.810	1.412	46.030	85.000
100.000	90.000	0.167	1.058	1.142	78.800	110.000
125.000	115.000	0.130	0.900	1.238	92.894	135.000
150.000	140.000	0.107	0.709	1.191	117.570	160.000
175.000	165.000	0.091	0.580	1.143	144.403	185.000

Acknowledgements: We are indebted to the NASA WB-57F crews and SPEC engineers for support of the 2D-S and CPI. John H. Bain of NASA Johnson Space Center is credited with taking the photograph of the subvisible cirrus layer (Fig. 1) from the back seat of the WB-57F. We are appreciative of the Harvard group, Liz Moyer, Tom Hanisco and David Sayres for the ICOS data and Droplet Measurement technologies, Darrel Baumgardner and Grey Kok for the CAPS data. We appreciate insightful comments offered by Bernd Kärcher, which improved the quality of the manuscript. This research was funded by the NASA Radiation Sciences Program under Grant NNG04GE71G. The 2D-S was recently developed under funding from the U.S. Navy Office of Naval Research Contract N00014-02-C-0317.

References

Barrett, E. W., Herndon, L. R., and Carter, H. J.: Some measurements of the distribution of water vapor in the stratosphere, Tellus, 2, 302-311, 1950.

Baumgardner, D., Dye, J. E., Knollenberg, R. G. and Gandrud, B. W.: Interpretation of measurements made by the FSSP-300X during the Airborne Arctic Stratospheric Expedition, J. Geophys. Res., 97, 8035-8046, 1992

Baumgardner, D., Jonsson H., Dawson W., O'Connor, D., and Newton, R.: The cloud, aerosol and precipitation spectrometer: a new instrument for cloud investigations. Atmos. Res., 59-60, 251-264, 2001.

Beyerle, G., Schäfer, H.-J, Neuber, R., Schrems, O., and McDermid, I. S.: Dual wavelength lidar observation of tropical high altitude cirrus clouds during the ALBATROSS campaign, Geophys. Res. Lett., 25, 919–922. 1996.

Brewer, A. W.: Evidence for a world circulation provided by the measurements of helium and water vapor distribution in the stratosphere. Quart. J. Roy. Meteor. Soc., 75, 351– 363, 1949.

Clark, H. L.: Longitudinal variability of water vapor and cirrus in the tropical tropopause layer, J. Geophys. Res., 110, doi: 10.1029/2004JD004943, 2005.

Comstock, J. M., Ackerman, T. P., and Mace, G. G.: Ground based remote sensing of tropical cirrus clouds at Nauru Island: Cloud statistics and radiative impacts, J. Geophys. Res., 107, doi:10.1029/2002JD002203, 2002

Field, P. R., Wood, R., Brown, P. R. A., Kaye, P. H., Hirst, E., Greenaway, R., and Smith, J. A.: Ice particle interarrival times measured with a fast FSSP. J. Atmos. Oceanic Technol., 20, 249 – 261, 2003.

Folkins, I., Loewenstein, M., Podolske, J., Oltmans, S. J. and Proffitt, M., A 14 km mixing barrier in the tropics: Evidence from ozonesondes and aircraft measurements, J. Geophys. Res., 104, 22095-22102, 1999.

Gierens, K. M., Schumann, U., Helten, M., Smit, H., and Marenco, A.: A distribution law for relative humidity in the upper troposphere and lower stratosphere derived from three years of MOZAIC measurements, Ann. Geophysicae, 17, 1218–1226, 1999.

Goldfarb, L., Keckhut, P., Chanin, M.-L., and Hauchecorne, A.: Cirrus climatological results from lidar measurements at OHP (44_ N, 6_ E), Geophys. Res. Lett., 28, 1687–1690, 2001.

Heymsfield, A. J.: Ice particles observed in a cirriform cloud at -83°C and implications for polar stratospheric clouds, J. Atmos. Sci., 43, 851–855, 1986.

Immler, F., and Schrems, O.: LIDAR measurements of cirrus clouds in the northern and southern midlatitudes during INCA (55°N, 53°S): A comparative study, Geophys. Res. Lett., 29, 1809, doi:10.1029/2002GL015077, 2002.

Jensen, E. J., Toon, O. B., Pfister, L., and Selkirk, H. B.: Dehydration of the upper troposphere and lower stratosphere by subvisible cirrus clouds near the tropical tropopause, Geophys. Res. Lett., 23, 825–828, 1996.

Jensen, E. J., Read, W. G., Mergenthaler, J., Sandor, B. J., Pfister, L., and Tabazadeh, A.: High humidities and subvisible cirrus near the tropical tropopause, Geophys. Res. Lett., 26, 2347–2350, 1999.

Jensen, E. J., Toon, O. B., Vay, S. A., Ovarlez, J., May, R., Bui, P., Twohy, C. H., Gandrud, B., Pueschel, R. F., and Schumann, U.: Prevalence of ice-supersaturated regions in the upper troposphere: Implications for optically thin ice cloud formation, J. Geophys. Res., 106, 17,253–17,266, 2001.

Jensen, E. J. and Pfister, L.: Transport and freeze-drying in the tropical tropopause layer, J. Geophys. Res., 109, doi:10.1029/2003JD004022, 2004.

Jensen, E. J. Smith, J. B., Pfister, L, Pittman, J. V., Weinstock, E. M., Sayres, D. S., Herman, R. L., Troy, R. F., Rosenlof, K., Thompson, T. L., Fridlind, A. M., Hudson, P. K., Cziczo, D. J., Heymsfield, A. J., Schmitt, C., and Wilson, J. C.: Ice supersaturations exceeding 100% at the cold tropical tropopause: implications for cirrus formation and dehydration. Atmos. Chem. Phys., 5, 851–862, 2005.

Jensen E. J., Pfister, L., Lawson, P., Baker, B., Mo, Q., Baumgardner, D., Weinstock, E. M., Smith, J. B., Moyer, E. J., Hanisco, T. F., Sayres, D. S., Herman, R. L., Troy, R. F., Alexander, M. J., Toon, O. B. and Smith, J. A.: Formation of Large (≅100 μm) Ice crystals near the tropical tropopause. Submitted to: J. Atmos. Chem. Phys., February, 2007.

Kärcher, B. and Solomon, S.: On the composition and optical extinction of particles in the tropopause region, J. Geophys. Res., 104, 27,441–27,459, 1999.

Koop, T., Luo, B. P., Tsias, A., Peter, T.: Water activity as the determinant for homogeneous ice nucleation in aqueous solutions. Nature 406, 611–614. 2000.

Korolev, A.V., Strapp, J. W., and Isaac, G. A.: Evaluation of the accuracy of PMS optical array probes, J. Atmos. Oceanic Technol., 15, 708-720, 1998.

Korolev, A. V.: Reconstruction of the sizes of spherical particles from their shadow images. Part I: Theoretical considerations, J. Atmos. Oceanic Technol., in press, 2007.

Lawson, R.P., Baker, B.A., Schmitt, C.G., and Jensen, T.L.: An overview of microphysical properties of Arctic clouds observed in May and July during FIRE.ACE. J. Geophys. Res., 106, 14,989-15,014, 2001.

Lawson, R. P., O'Connor, D., Zmarzly, P., Weaver, K., Baker, B. A., Mo, Q., and Jonsson, H.: The 2D-S (Stereo) probe: design and preliminary tests of a new airborne, high speed, high-resolution particle imaging probe, J. Atmos. Oceanic Technol., 23, 1462-1477, 2006.

Lelieveld, J., Bregman, A., Scheeren, H. A., Ström, J., Carslaw, K. S., Fischer, H., Siegmund, P. C., and Arnold, F.: Chlorine activation and ozone destruction in the northern lowermost stratosphere, J. Geophys. Res., 104, 8201–8213, 1999.

May, R. D.: Open path, near-infrared tunable diode laser spectrometer for atmospheric measurements of H_2O, J. Geophys. Res., 103, 19161-19172, 1998.

McFarquhar, G. M., Heymsfield, A. J., Spinhirne, J., and Hart, B.: Thin and subvisual tropopause tropical cirrus: Observations and radiative impacts, J. Atmos. Sci., 57, 1841–1853, 2000.

Murphy, D. M., Kelly, K. K., Tuck, A. F., Proffitt, M. H., and Kinne, S.: Ice saturation at the tropopause observed from the ER-2 aircraft, Geophys. Res. Lett., 17, 353–356, 1990.

Murphy, D. M., Cziczo, D. J., Froyd, K. D., Hudson, P. K., Matthew, B. M., Middlebrook, A. M., Peltier, R. E., Sullivan, A., Thomson, D. S., and Weber, R. J., Single-particle mass spectrometry of tropospheric aerosol particles, J. Geophys. Res., 111, D23S32, doi:10.1029/2006JD007340, 2006.

Oltmans, S. J., Vo¨mel, H., Hofmann, D. J., Rosenlof, K. H., and Kley, D.: The increase in stratospheric water vapor from balloon-borne, frostpoint hygrometer measurements at Washington, D.C. and Boulder, Colorado, Geophys. Res. Lett., 27, 3453– 3456, 2000.

Ovarlez, J., van Velthoven, P., Sachse, G., Vay, S., Schlager, H., and Ovarlez, H.: Comparisons of water vapor measurements from POLINAT 2 with ECMWF analyses in high-humidity conditions, J. Geophys. Res., 105, 3737–3744, 2000.

Ovarlez,J., J.-F Gayet, J.-F., Gierens, K., Ström, J., Ovarlez, H., Auriol, F., Busen, R., and Schumann, U., Water vapour measurements inside cirrus clouds in Northern and Southern hemispheres during INCA, Geophys. Res. Lett., 29, doi:10.1029/2001GL014440, 2002.

Peter, T., Luo, B. P., Wenrli, H., Wirth, M., Kiemle, C., Flentje, H., Yushkov, V. A., Khattatov, V., Rudakov, V., and S. Boormann, A. T., Toci, G., Mazzinghi, P., Beuermann, J., Schiler, C., Cairo, F., Don-francesco, G. D., Adriani, A., Volk, C. M., Strom, J., Noone, K., Mitev, V., MacKenzie, R. A., Carslaw, K. S., Trautmann, T., Santacesaria, V., and Stefanutti, L.: Ultrathin Tropical Tropopause Clouds (UTTCs): I. Cloud morphology and occurrence, Atmos. Chem. and Phys., 3, 1557–1578, 2003.

Peter, T., Marcolli, C., Spichtinger, P., Corti, T., Baker, M. B., and Koop, T.: When Dry Air Is Too Humid. Science, 314, 1399-1402, 2006.

Sassen, K. and Campbell, J. R.: A midlatitude cirrus cloud climatology from the facility for atmospheric remote sensing. Part I: Macrophysical and synoptic properties, J. Atmos. Sci., 58, 481–496, 2001.

Sayres, D. S.: New techniques for accurate measurement of water and water isotopes,

Ph.D. Thesis, Harvard University, Cambridge, MA., 2006

Scott, S.G., Bui, T. P., Chan, K. R., and Bowen, S. W.: The meteorological measurement system on the NASA ER-2 aircraft, J. Atmos. Ocean. Tech., 7, 525-540, 1990.

Thomas, A., Borrmann, S., Kiemle, C., Cairo, F., Volk, M., Beuermann, J., Lepuchov, B., Santacesaria, V., Matthey, R., Rudakov, V., Yushkov, V., MacKenzie, A. R., Stefanutti, L.: In situ measurements of background aerosol and subvisible cirrus in the tropical tropopause region, J. Geophys. Res., 107, 4763, doi: 10.1029/2001JD001385, 2002.

Wang, P.-H., Minnis, P., McCormick, M. P., Kent, G. S., and Skeens, K. M., A 6-year climatology of cloud occurrence frequency from Stratospheric Aerosol and Gas Experiment II observations (1985 1990), J. Geophys. Res., 101, 29,407-29,429, 1996.

Weinstock, E. M., Hintsa, E. J., Dessler, A. E., Oliver, J. F., Hazen, N. L., Demusz, J. N., Allen, N. T., Lapson, L. B., and Anderson, J. G.: New fast response photofragment fluorescence hygrometer for use on the NASA ER-2 and the Perseus remotely piloted aircraft, Rev. Sci. Instrum., 22, 3544–3554, 1994.